Double-Difference Tomography Applied to Monitoring of Geologic Carbon Sequestration in the Aneth Oil Field, Utah

Brent Allan Slaker

Thesis submitted to the faculty of the Virginia Polytechnic Institute and State University in partial fulfillment of the requirements for the degree of

Master of Science
In
Mining & Minerals Engineering

Erik Westman, Chairman
Kramer Luxbacher
Nino Ripepi

6 December 2011
Blacksburg, VA

Keywords: Double-Difference Tomography, Carbon Sequestration, Synthetic Data

DOUBLE-DIFFERENCE TOMOGRAPHY APPLIED TO MONITORING OF GEOLOGIC CARBON SEQUESTRATION IN THE ANETH OIL FIELD, UTAH

Brent Slaker

ABSTRACT

Double-difference seismic tomography is performed on a carbon sequestration operation in the Aneth Oil Field in southeast Utah as part of a Department of Energy initiative on monitoring, verification, and accounting of sequestered CO_2. A total of 1,211 seismic events were recorded from a borehole array of 22 geophones. Aneth Unit data were divided into four time periods for time-lapse analysis. A low velocity zone spanning the lateral extents of the observable region, likely representing a CO_2 plume, is detected when considering voxels containing the highest ray path coverage. A series of synthetic tomography tests simulating different CO_2 plume sizes and locations was performed to assist in characterizing velocity changes associated with Aneth Unit data. Inferences about the existence of a CO_2 plume should be made by comparing actual data to synthetic data resulting from simulations performed under similar conditions. Considering synthetic simulation similarities and a derivative weight sum analysis, a CO_2 plume can be imaged within the Desert Creek reservoir, but the resolution of the CO2 plume is too low for proper monitoring, verification, and accounting of injected CO_2. Recommendations, for improving CO_2 plume resolution through double difference seismic tomography, are made to increase the ray path distribution throughout the Aneth Unit by varying geophone locations.

ACKNOWLEDGEMENTS

I thank my advisor, Dr. Erik Westman, for the opportunity to pursue my Master's Degree at Virginia Tech and for his guidance, support, and willingness to take time out of his busy schedule to answer questions or provide assistance in this project and other graduate studies. I thank both Dr. Luxbacher and Dr. Ripepi for generously agreeing to sit on my committee.

I thank Ben Fahrman and Jeff Kerr for the assistance they provided in troubleshooting and understanding the programs and principles associated with tomography, and for being a sounding board as I worked through problems. I thank the rest of the 115A office, Michael Kiser, Sarah Smith, Dan Sadtler, Meredith May, and Xu Ma for their moral support over the past year and a half.

I would also like to thank my friends and family for their patience, support, assistance, and prayers during the course of this project.

Contents

List of Figures

List of Tables

Chapter 1: Introduction

Climate change is a significant international concern, often attributed to increasing concentrations of greenhouse gasses in Earth's atmosphere, namely Carbon Dioxide (CO_2). Fossil fuels are responsible for the majority of anthropogenic CO_2 emissions, but also sustain the global economy. This conflict has created one of the greatest geo-political environmental issues in recent history. One method for reducing the amount of CO_2 released into the atmosphere is geologic carbon sequestration. Geologic carbon sequestration is the capture of CO_2 before it reaches the atmosphere, and its storage under deep geologic formations, such as depleted oil reserves, unmineable coal seams, or deep saline formations.

One of the first challenges encountered by the storage of CO_2 is the selection of a reservoir with sufficient storage capacity, appropriate sealing mechanism, and an absence of faults or fractures through which fluid migration may occur. Post-injection, the engineering challenge shifts to monitoring, verification, and accounting (MVA) of injected CO_2. There are three primary objectives of MVA:

- Monitoring - monitor both the location and impact of sequestered CO_2.
- Verifying - verify movement of CO_2 and ensure that sequestered CO_2 is not permeating the sealing mechanism, or migrating to an unsealed area.
- Accounting - account for the amount of injected CO_2 by comparing it to the amount of CO_2 estimated to be in place, through the chosen monitoring method.

The United States Department of Energy has established seven regional carbon sequestration partnerships to test the feasibility of geologic carbon sequestration as a means of storing CO_2 and preventing its release into the atmosphere. The goal of each of these partnerships is to assist in the development of technology, infrastructure, and regulations necessary to implement large-scale CO_2 sequestration projects in different regions and geologic formations [1].

Seismic tomography is a useful tool for characterizing geologic structures, and is anticipated to providing accurate method of monitoring, verification, and accounting of injected CO_2. Similar in principles to the more widely recognized and practiced medical tomography, seismic tomography utilizes seismic energy generated either passively or actively in rock masses to make inferences about the state of the medium through which the seismic energy passes. Expanding further on traditional tomography, double-difference seismic tomography is a method of improving precision of seismic source locations and accuracy of velocity model reconstruction by reducing travel path residuals among closely spaced seismic events.

A practical application of double-difference tomography to the monitoring, verification, and accounting of injected CO_2 is conducted on a carbon sequestration operation in the Aneth oil field. Data for this experiment are provided by Resolute Natural Resources and the National Energy Technology Laboratory as part of the Southwest Regional Partnership on Carbon Sequestration. Analysis of event, receiver, and travel time data provided for the Aneth Unit of the Aneth oil field is performed on a time-lapse basis to determine CO_2 plume extents, CO_2 concentration changes, and any leakage of CO_2 from the reservoir. Appropriate damping and smoothing values are selected to optimize the performance of the velocity model reconstruction. Simulations with synthetic travel times for a variety of different CO_2 plume sizes and locations are also conducted to assist in the verification of results obtained from the Aneth Unit data. This thesis will demonstrate the degree to which sequestered CO_2 can be monitored, verified, and accounted for in the Aneth Unit through time-lapse analyses of velocity changes and comparisons of synthetic plume simulations to Aneth Unit data.

Chapter 2: Literature Review

Predictions of global energy use throughout the next century suggest increasing levels of carbon emissions and rising concentrations of carbon dioxide (CO_2) in the atmosphere [1]. Concentrations of greenhouse gases have increased since the Industrial Revolution, to the level that measurable climate change has been attributed by many to human activity. Greenhouse gasses trap energy from the sun within Earth's atmosphere, warming the planet. The extent to which humans increase the concentration of greenhouse gasses in the atmosphere, and the global warming that occurs as a result, is referred to as the enhanced greenhouse effect. The gas considered most responsible for the enhanced greenhouse effect is CO_2, largely as a consequence of fossil fuel combustion for energy production. Currently, about 33 gigatons of CO_2 are produced annually from anthropogenic sources [2]. Fossil fuels provide roughly 85% [3] of the world's energy, and are likely to remain a large component of the world's energy portfolio for many decades due to their low cost, wide availability, ease of transport, and large reserves.

2.1 Geologic Carbon Sequestration

Geological sequestration of CO_2 is the most likely method to provide the first large scale opportunity for concentrated sequestration of CO_2 because the technology exists and has been used extensively in enhanced recovery projects [4]. Geologic carbon sequestration is a means of reducing carbon emissions by capturing carbon dioxide from the exhaust of fossil fuel power plants and other sources and sequestering them within geologic formations. CO_2 can be trapped in these formations as either a gas or a supercritical fluid. It is generally injected in a supercritical phase at pressures above 69 bars to reduce the injected volume. The costs of separation and capture of CO_2, including compression to sequestration pressures, are estimated to account for approximately 75% of the cost of geologic sequestration [1]. Geologic formations selected for carbon sequestration should be deeper than 762 meters to ensure that the injected CO_2 will remain in a supercritical state [43]. While the density of supercritical CO_2 is greater than that of gaseous CO_2, it is still less than the density of other in-situ fluids. As a result, the

migration of CO_2 away from the injection well is dependent on gravity and an unfavorable mobility ratio.

The permanence of sequestered CO_2 depends on the effectiveness of the trapping mechanism. To ensure that the injected CO_2 does not buoyantly rise to the surface, an impermeable barrier, known as a caprock, is required to trap the CO_2 within the geologic formation. This is similar to the natural geologic trapping of oil, where oil is unable to permeate an overlying caprock. Depending on the formation in which the CO_2 is injected, it may eventually dissolve into the ground water. CO_2 may also become trapped in the form of carbonate minerals formed by chemical reactions with the surrounding rock [6].

The three most widely suggested storage sites for large scale geologic carbon sequestration are: oil and gas reservoirs, saline formations, and unmineable coal seams. Each storage location has its own advantages and disadvantages. Oil and gas reservoirs have a known caprock, a potential for fuel recovery to offset the cost of sequestration, and a well characterized volume, due to extensive exploration. Oil and gas reservoirs also have good access to in-place CO_2 pipelines, however the scarcity of these pipelines is a disadvantage to geologic carbon sequestration overall. There are several disadvantages to sequestering CO_2 in oil and gas reservoirs. One disadvantage is both the limited number of oil and gas reservoirs, and the storage capacity of these reservoirs. The U.S. Department of Energy estimates that the total storage capacity of oil and gas reservoirs in the United States is limited to 140 gigatons of CO_2 [6]. Another disadvantage is the large number of boreholes used for oil and gas development may need to be remediated in order to prevent possible leakage pathways.

Advantages to deep saline formations include their large storage capacities and wide distribution. The U.S. Department of Energy estimates the storage potential of deep saline aquifers to be around 12,600 gigatons of CO_2 in the United States. Due to a lack of economic incentive to explore deep saline formations, they have been very poorly characterized and have the most geologic uncertainty concerning seal effectiveness and storage capacity. Storage capacity in saline formations is difficult to determine because multiple methods of storing the CO_2 are

available: trapping underneath an impermeable cap rock and dissolution and mineralization of the CO_2 [6].

Storage in unmineable coal seams has the advantage of nearby power plants, offering the potential for methane recovery to offset the cost of sequestration. The unmineable coal seams, however, suffer from the same storage capacity issues as oil and gas reservoirs, with capacities numbering in the tens to hundreds of gigatons of CO_2. In addition to these problems, unmineable coal is hard to define, as coal seams that are unmineable today may be capable of being mined years later [6]. Initial sequestration projects are more likely to occur in depleted oil and gas fields or unmineable coal seams due to the quality of subsurface data and the ability to mitigate sequestration costs through enhanced oil and gas recovery. However, due to the large storage potential available, most long-term geologic carbon sequestration will likely occur in deep saline formations [7].

2.2 Induced Seismicity

Geologic carbon sequestration has the potential for inducing seismic events through fluid injection. Mining activity, reservoirs, long-term fluid withdrawal wells, and long-term fluid injection wells have all created events on the microseismic level, but also have the potential to cause events with large enough magnitudes to damage surface facilities. Seismic activity was first linked to deep well injection at the Rocky Mountain Arsenal in Denver, Colorado [5]. The seismic activity was a result of waste water disposal in a deep injection well, drilled in 1961 by the Army Corps of Engineers. Between 1962 and 1967, over 1,500 seismic events were detected in the area with magnitudes as high as 5.5 [8]. Induced seismicity is recognized to be a hazard in nearly any engineering activity that alters the stress or pore-pressure within the earth's crust. The earth's crust is generally supporting very high stress levels and is often close to failure [9].

There are several potential mechanisms of induced seismicity, such as hydraulic fracturing, slipping resulting from redistribution of elastic stresses, slipping resulting from pore pressure relaxation, or a combination of these mechanisms. It is hypothesized that the dominant

mechanism of triggering induced seismicity is the diffusive process of pore-pressure relaxation in porous, saturated rocks. The tectonic stress in the earth's crust is, at some locations, close to a critical state that would cause brittle failure of rocks. If fluid pressure in a reservoir is increased, pore-pressure in the critical locations is also increased. This increase in the pore-pressure causes the effective normal stress to decrease, allowing for slipping along pre-existing cracks [10]. When injected fluid enters pre-existing microfractures within the rock, part of the normal stress is supported. Fluid has no shear strength and, as a result, the frictional resistance to sliding is lowered by an amount equivalent to the pressure of the fluid [11]. Fault stability assessments and estimates for the maximum sustainable fluid pressure are typically based on the Mohr-Coulomb failure criterion.

Several conditions, which must be satisfied to induce seismic events by injection of fluids, are suggested by McClain. First, the most important condition to be satisfied is the presence of regional tectonic stresses near the breaking strength of the rocks, prior to injection. Second, the reservoir formation must be porous enough to accept the fluids and simultaneously have a permeability low enough for pore pressure to increase. Last, the fluid must be injected into the formation at a high enough rate to significantly increase pressures over a wide area [12].

In determining displacement along faults due to induced slipping, the fault-plane solutions from the first motions detected by the recorded seismograms should be calculated. This requires a well calibrated array of seismic monitoring stations [13]. As a means to map reservoir dynamics, the deployment of geophones, or other acoustic sensors, is promoted to compliment standard engineering gauges. These monitoring devices can measure microseismic events related to induced seismic movements along existing fractures or the creation of new fractures. Microseismic data can be used to determine the location of the fracturing or to infer geomechanical details of the formation.

Monitoring can take place from either surface arrays or borehole arrays. Borehole deployments generally allow for closer placement of instrumentation to the seismic events, maximizing sensitivity. Surface arrays, while easier to deploy, provide a limited event monitoring resolution and are unable to detect seismic events with travel paths that do not reach the surface. A study at

the Ekofisk field in the North Sea had a maximum travel path recorded for seismic events of 2 kilometers, while the reservoir was 3 kilometers in depth. Without borehole monitoring, the seismic activity would have gone undetected [14].

2.2.1 Intensity and Frequency of Occurrence

The intensity and frequency of induced seismic events is controlled by a change in fluid injection rates, the net amount of fluid injected into a formation, the orientation of the stress field relative to the pore-pressure increase, and the size and extent of the local fault system [15]. Suckale suggests several reasons for the absence of a simple relationship between the quantity of fluid injection and seismicity. An absence of a correlation could be explained by: inaccuracies in the location of hypocenters, a lack of data regarding the precise injection pattern over time, a lack of high-quality instrumentation during the onset of seismic activity, or the clustering of seismic activity could obscure the fact that selected events are closely related to injection patterns [11].

The most well documented seismic events induced by fluid injection are associated with water flood operations for enhanced recovery. These operations often include large arrays of wells injecting fluids at high pressures into confined reservoirs with low permeability. Waste disposal wells tend to inject fluids at lower pressures into large, porous aquifers with high permeability, away from fault structures. As a result, only three waste disposal sites have been conclusively shown to have induced significant seismic activity: Ashtabula, Ohio, El Dorado, Arkansas, and Denver, Colorado [8].

Certain regions are more inclined to produce a higher seismic moments and more seismic activity than others. This inclination depends on the existing stress conditions within the upper crust. In some regions, elevating formation fluid pressures by only tens of bars can trigger shallow seismic events. The Great Lakes region of the Appalachian Plateau is a prime example of a region especially vulnerable to increased fluid pressures. Injection pressures ranging from 60 to 100 bars have triggered earthquakes in northeastern Ohio, western New York, and southwestern Ontario [8].

Many forms of deep well injection have resulted in significant numbers of induced seismic events, but CO_2 injection for enhanced oil recovery has a proven history of seismic stability. 30 megatons of CO_2 is currently being injected worldwide, annually, for enhanced oil recovery. A cumulative amount of 500 megatons of CO_2 has been injected to date, yet there have been no high magnitude seismic events attributed to enhanced oil recovery using CO_2 injection [16].

2.2.2 Seismicity Mitigation

There are several steps that can be taken to reduce the chance of experiencing induced seismic events or to reduce the intensity of induced seismic activity. The most important step is choosing sequestration sites that avoid formations or locations prone to fracturing or earthquakes [17]. Basins located in tectonically active areas, such as locations around the Pacific Ocean and northern Mediterranean Sea, are more likely to experience seismic events as a result of CO_2 injection. Basins formed in mid-continent regions or on the edges of stable continental plates, are stable long-term storage locations. Exceptions to this rule include the Los Angeles Basin and the Sacramento Basin, both of which have demonstrated stable storage capacity, yet lie in tectonically active regions. General guidelines can be established for selecting an ideal reservoir location, but care must still be taken to analyze the reservoir on an individual basis, considering site-specific conditions [16].

Another precaution that can be taken to reduce seismic activity is to set injection rates that keep pressures below the fracture strength of the surrounding rocks [17]. As discovered in Rangely, Colorado, changing injection rate correlates far better to seismic activity than net injected volume. With proper seismic monitoring of the region surrounding the injection well, the injection rates can be normalized or reduced if seismic activity becomes too extreme. Carefully selecting an injection rate that will not exceed the critical pressure of the injection site will help reduce seismic activity and intensity resulting from fluid injection. The scope of a fluid injection project could also play a significant role in the amount of seismicity experienced. Long-term fluid injection generally carries a higher risk of inducing high-magnitude seismic events than

short-term injections, since the total volume of rock where the stress field has been altered is expected to be larger [9].

2.3 Tomography

Tomography is derived from the Greek word *tomos*, meaning the study of slices. The process of recreating the internal structure of a body by compiling a series of projections, or slices, is generally referred to as tomography [18]. Generating an image, or tomogram, of an object by examining its reaction to the passive, probing energy from an external source forms the foundation of tomography [19]. The most common application of tomography is in the form of medical imaging, known as CAT (Computer Assisted Tomography) scans, which create a two-dimensional image from a series of one-dimensional line projections. Not limited to the most familiar imaging signal, X-rays, used in CAT scans, the signals used in tomography are incredibly varied in both type and scale. The most common types of tomographic signals include: seismic waves, ultrasound, magnetic resonance (MRI), X-rays, gamma rays, neutron beams, and electron microscopy. These signals can vary in scale from nanometers, during electron microscope reconstructions of viruses and atomic lattices, up to kilometers for seismic tomography applications [18]. Seismic tomography may be new by name, but it is fundamentally very similar to techniques that have been in use for many years, not only in the medical community but geophysical community as well. One example of a geophysical application of tomography is the wide range of engineering problems encountered in the oil industry. Many of these problems, from exploration and development to production can make use of seismic tomography. Applying tomography to previously existing or newly collected seismic data can allow for the generation of subsurface velocity models, providing a non-invasive procedure for assisting in these phases of operation [19]. Global seismology is another field which has been making use of tomography for many years. Global seismology has, however, lagged behind seismic exploration in development of accurate tomographic imaging for several reasons: earthquakes used in global seismology are both uncontrolled in their magnitude and location, coverage of the Earth in seismometers is limited, and instrument responses have been inconsistent [20].

2.3.1 Seismometers

The means by which signals are detected, in seismic tomography, are through seismometers. Modern seismometers first came into use around the end of the 19th century. Since their implementation, seismic waves have been used to locate remote objects and earthquake epicenters. Efforts were even made during World War I to locate heavy artillery batteries by examining seismic wave propagation [20]. Seismic sensors can be delineated into two main categories: inertial seismometers and extensometers. Inertial seismometers measure the motion of the ground relative to an inertial reference. Extensometers measure the movement of a single point on the ground relative to another point. Extensometers are well suited for low frequency measurements, but the large relative moment associated with earthquakes makes inertial seismometers well suited to seismic tomography [21]. Inertial seismometers make use of a suspended mass to convert ground motion into an electrical signal. The signal generated depends on both the amplitude of ground motion and how suddenly the event occurs.

2.3.2 General Principles

While the methods may differ, the principles behind the different forms of tomography remain the same. X-ray absorption tomography, for example, constructs images by analyzing the reduction in radiation as X-rays pass through a sample along a straight line [18]. Seismic tomography accounts for wave propagation along curved paths, but rather than measuring the intensity of a wave, the speed at which the wave traveled may be used to infer properties of the medium through which it passed.

The curved paths of seismic waves are governed by Snell's Law, which is derived from Fermat's Principle of Least Time. Fermat's Principle states that light will take the shortest possible travel path from point A to point B. Snell's law is derived from Fermat's Principle with dimensional variables presented in Figure 2.1.

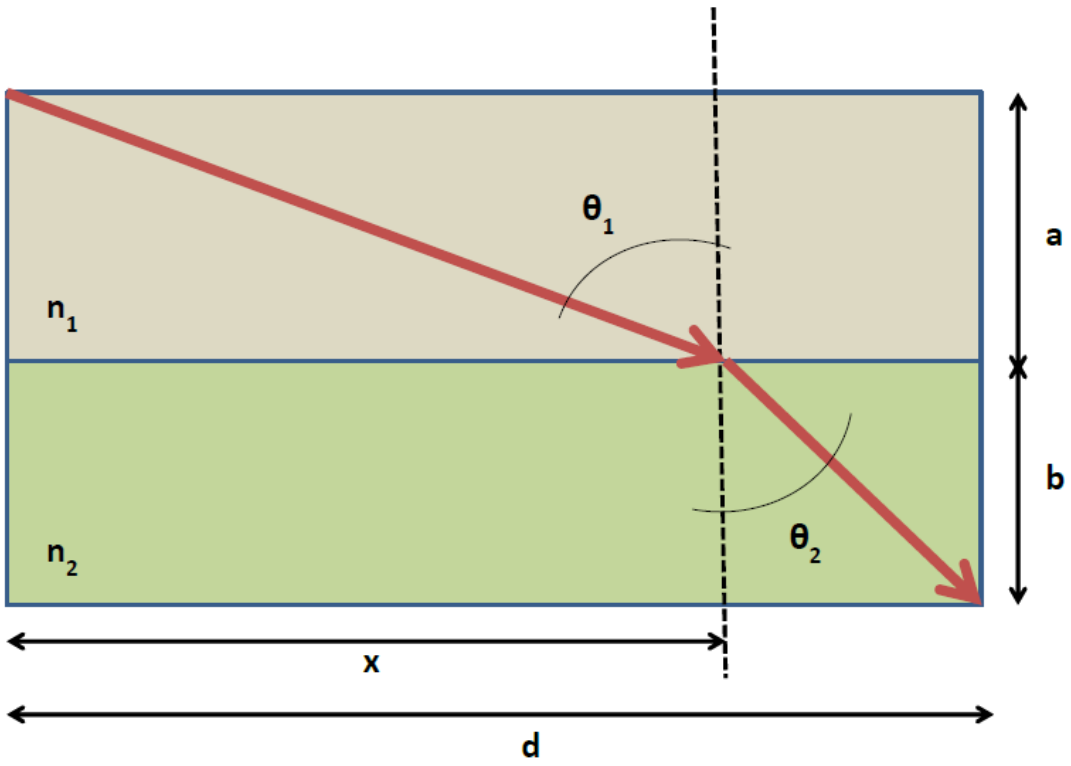

Figure 2.1: Wave Refraction

Fermat's principle is given below, where t is the travel time of the ray path, c is the speed of light, and n_1 and n_2 are the indices of refraction:

$$t = \frac{\sqrt{x^2 + a^2}}{c/n_1} + \frac{\sqrt{(d-x)^2 + b^2}}{c/n_2} \qquad \text{Equation 2.1}$$

Setting dt/dx equal to zero yields

$$n_1 \frac{x}{\sqrt{x^2 + a^2}} = n_2 \frac{d-x}{\sqrt{(d-x)^2 + b^2}} \qquad \text{Equation 2.2}$$

which can then be simplified into Snell's law using the angles of refraction as shown:

$$n_1 sin\theta_1 = n_2 sin\theta_2 \qquad \text{Equation 2.3}$$

Snell's law is useful for determining refraction angles, but it has limitations, namely in its ability to determine wave amplitudes or wave behaviors [22].

2.3.3 Seismic Tomography Principles

Medical tomography and seismic tomography also differ in their ray path distribution. Ray path distribution is determined by the event location, receiver location, and the medium through which the ray path travels. Ray bending, as a result of heterogeneous media, was explained through Snell's Law. Event and receiver location, however, are determined by the researcher or experimental conditions. In the case of medical tomography, the receiver and event locations are both known and chosen by the technician, so accurate ray paths can be determined. Event and receiver placement are more difficult when performing seismic tomography. With insufficient ray path distribution, velocity features may be smeared when performing seismic tomography [23]. Receiver locations are precisely known, but event locations are often unknown, unless active sources are used. Active source locations, artificially created and with a known hypocenter, have been used in the past to image individual pillars or tunnel stress distribution, but are labor-intensive, and therefore impractical for long-term monitoring programs [23]. Passive seismic events are seismic events already occurring at the location of interest. Passive seismic monitoring has applications in a wide range of engineering projects that make use of induced seismic events, such as oil and gas production [24], carbon sequestration [25], or mining [23]. For mine-stress analysis, using mining-induced microseismic events as ray path sources can be advantageous due to their frequency of occurrence and location, most likely occurring near the area of active mining [26]. Passive microseismic events are ideal for noninvasive, remote, time-lapse monitoring [26], because they allow for continuous observation of stress levels, fluid migration, or other time-dependent analyses.

Passive seismic imaging requires that both the seismic event locations and velocity structure be calculated simultaneously. A homogeneous velocity model can be assumed for initial source location, but more accurate source locations can be determined if velocity heterogeneities are accounted for prior to locating sources. The accuracy of source locations is one of the most important factors in any acoustic emission experiment [27]. The accuracy of reconstructed three-dimensional structures is sensitive to the initial velocity model, increasing the importance of obtaining an accurate or reliable starting model [28].

In addition to characterizing geologic structures, tomography can be used to determine the distribution of stress magnitude or monitor fluids within a rock mass. Higher stressed areas tend to produce higher seismic wave velocities due to the closing of microfractures and reduction of pore space within a rock mass. This trend does not continue as the rock begins to fail, because new fractures are being formed, creating additional void space that reduces the seismic wave velocity [26]. Many different factors influence the velocity of seismic wave propagation through rock masses, including: joints or faults, porosity, rock strength, density, depth, stress magnitude, stress anisotropy, degree of saturation, and the type of saturation fluid [29].

Fluid displacement within a rock mass is also capable of being imaged through tomography. Rocks in the subsurface may be saturated with brine, which has a specific associated p-wave velocity. If the brine is displaced by a fluid with different elastic properties, the p-wave velocity of waves traveling through that medium will change. This principle has applications to carbon sequestration, as CO_2 has different elastic properties than brine. The increased compressibility of CO_2 will result in subtle velocity changes in the host rock, which can then be imaged through the use of tomography [30]. Reservoirs with favorable injection and storage characteristics, such as high porosity and permeability, tend to have seismic properties suitable for CO_2 monitoring. Reservoirs with low permeability and low porosity are likely to have poor seismic conditions for imaging [31].

Cross-well seismic tomography is one common method of applying these tomographic techniques. This form of tomography involves generating events in one borehole and detecting them in another borehole with an array of geophones. Shown in Figure 2.2, cross-hole seismic tomography can be useful for determining the location and extent of low velocity zones between two boreholes. This method of velocity model reconstruction has revolutionized subsurface seismic measurements for a variety of engineering applications, such as tunnel development, deep foundation construction, and petroleum reservoir monitoring [29].

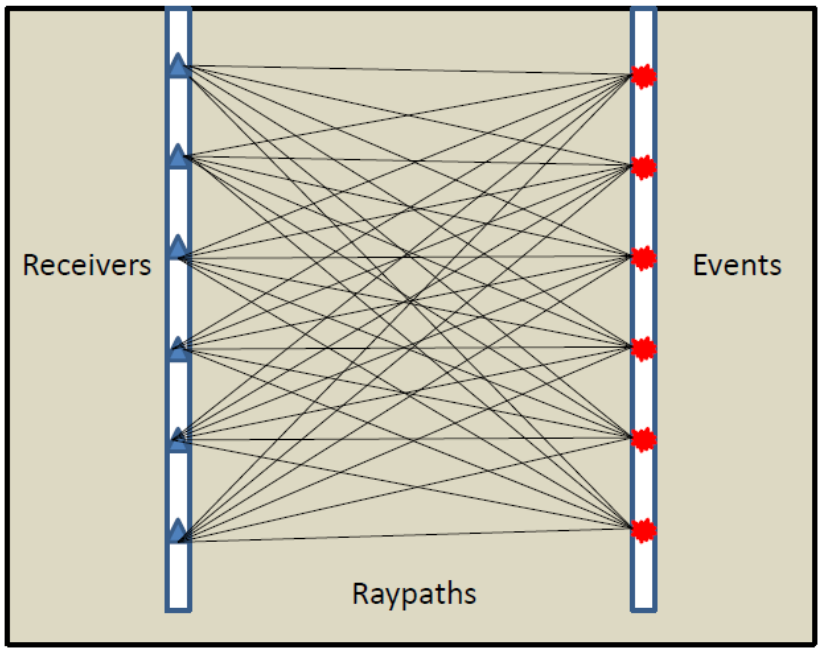

Figure 2.2: Cross-Well Seismic Tomography

Regardless of method or application, the success of arrival-time tomography is dependent on the quality of data, the travel-time calculation method, the constraints placed on the model, the weighting values selected, and the algorithms chosen to invert the system of linear equations [28].

2.3.4 Double-Difference Tomography

Double-difference tomography began as the double-difference earthquake location algorithm, developed by Waldhauser and Ellsworth [32]. This method attempts to minimize the residuals between observed and theoretical event-to-receiver travel times. If the hypocentral separation between two seismic events is small when compared to the absolute distance between the event and receiver, then it can be assumed that the ray paths are similar along the entire ray path, except for the small region near the spatial offset between the two events. The difference in these two travel times is a result of the spatial offset between the events rather than any velocity differences encountered between the event and station, due to their absolute errors being shared along the rest of the ray path [32]. Figure 2.3 shows an example event arrangement for a station X.

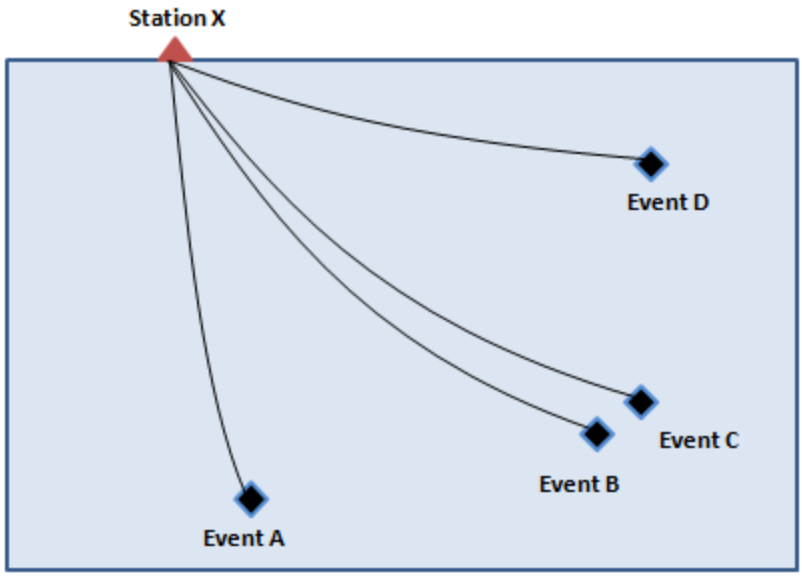

Figure 2.3: Coupled Events for Use in Double-Difference Tomography

If it is assumed that events B and C are closely spaced in relation to their total travel path, then the double-difference equation is given as

$$dr_X^{BC} = (t_X^B - t_X^C)^{obs} - (t_X^B - t_X^C)^{cal} \qquad \text{Equation 2.4}$$

where dr_X^{BC} is the double-difference, or residual between the observed and calculated differential travel times t [32].

Zhang and Thurber later adapted this double-difference earthquake location algorithm to simultaneously locate seismic events and reconstruct the velocity structure of the region. By simultaneously solving for event locations and velocity structure, the precision of event location should be improved due to a higher resolution 3-dimensional velocity model. Three types of data are used in the double-difference tomography method: absolute arrival times, catalog differential arrival times, and differential travel times obtained from waveform cross-correlation data [33].

2.4 Rock Mechanics

Waves are the phenomena through which tomography is possible. A wave can be described as "a disturbance that transfers energy and momentum progressively from one particle to another particle in a medium [34]." These waves are separated into two broad categories: electromagnetic waves and mechanical waves. Mechanical waves require a medium, such as water, air, or rocks to transfer mechanical energy between points, whereas electromagnetic waves can transmit energy in a vacuum [34]. Quantities frequently used to describe wave motion include frequency (f), amplitude (A), wavelength (λ), and period (T) [35]. Frequency is number of cycles per unit time and period is the time taken to complete one cycle. Wavelength and amplitude are presented in Figure 2.4.

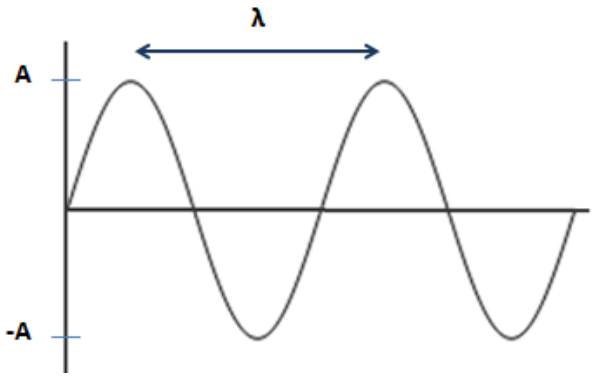

Figure 2.4: Wave Properties

Waves can further be separated into transverse waves and longitudinal waves. Particles in transverse waves oscillate perpendicularly to the direction of propagation of the wave, whereas particles in longitudinal waves oscillate parallel to the direction of propagation of the wave [34]. Seismic body waves are composed of both longitudinal (compression) and transverse (shear) waves, called P and S waves respectively. P waves are capable of traveling through liquids and propagate at a velocity related to their frequency (f) and wavelength (λ), given by the equation:

$$V_p = \lambda f \qquad \text{Equation 2.5}$$

S waves travel at slightly more than half the velocity of P waves and create shear forces in the medium they pass through, allowing for division of S waves into S_H waves, causing horizontal motion, and S_V waves, causing vertical motion. Due to liquids not having a shear strength, S waves are incapable of propagating through them [36].

Considering that P and S waves are mechanical waves, they require that an elastic medium transmit them. The elasticity of that medium determines how well the seismic waves are transmitted, represented by several elastic moduli. These varying elastic moduli are [37]:

- The Young's Modulus: given by the ratio of extensional stress to the resulting extensional strain.
- The bulk modulus: a measure of uniform incompressibility of the material.
- the shear modulus: a measure of a material's resistance to shearing, or changing shape while maintaining a constant volume
- Poisson's ratio: compares a material's transverse strain to its axial strain.

The approximate bulk modulus, shear modulus, Poisson's ratio, and density of several common materials, and their corresponding P and S wave velocities are given in Table 2.1.

Table 2.1: Typical Material Properties (Averages adapted from [37])

Medium	Bulk Modulus (GPa)	Shear Modulus (GPa)	Density (kg/m^3)	Poisson's Ratio	Vp (km/s)	Vs (km/s)
Air	0.0001	0	1	0.5	0.32	0
Water	2.2	0	1000	0.5	1.5	0
Sandstone	24	17	2500	0.21	4.3	2.6
Limestone	38	22	2700	0.19	4.7	2.9
Granite	56	34	2610	0.25	6.2	3.6
Basalt	71	38	2940	0.28	6.4	3.6

These moduli are dependent on stress and strain, whose relationship is commonly reported as a stress-strain curve, shown in Figure 2.5. The gradient of the linear portion of this curve is known as the Young's Modulus.

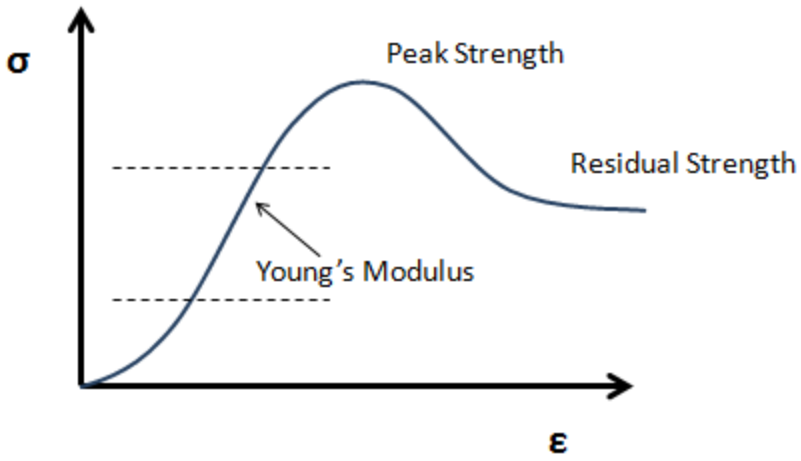

Figure 2.5: Stress-Strain Curve

Strain, by its simplest definition is the length of deformation of a body divided by its original length [38]. Stress, as it pertains to engineering, is a measure of the internal forces acting upon a deformable body, presented in force per unit area. Rock masses exist in a stressed state naturally, regardless of human activities. Understanding those natural stresses can assist in the mitigation of harmful effects the stresses might have on human activities, such as mining. Many civil or mining engineering projects require extensive knowledge of in-situ and induced stresses, such as: the stability of underground excavations, pillar design, drilling and blasting, and slope stabilities [39]. While there is no widely accepted terminology for describing the states of stress in a rock mass, it is described by Hudson in ten different ways [40]:

- *Tectonic Stress* – Stress resulting from the release of energy caused by tectonic plate movement. Tectonic stress is important to consider for safety factor calculations in underground construction projects, such as tunnels or caverns for gas and waste storage [41]. It can be delineated further into Global Tectonic Stress, concerning the shifting of plates, and Local Tectonic Stress, concerning plate bending and isostacy [42].
- *Gravitational Stress* – Stress from Earth's gravitational field, also called vertical stress. This stress encompasses the weight of the overburden, which increases with depth, as well as accounting for stress resulting from surface topography [42].
- *Natural Stress* – Also called in-situ stress or virgin stress, this is the stress that exists naturally in the rock mass before any man-made disturbance [42].
- *Regional Stress* – The stress state in a relatively large geological domain [40].

- *Local Stress* – The stress state in a small domain [40].
- *Near-field stress* – The stress state in the region of an engineering perturbation [40].
- *Induced Stress* – The stress state as influenced by man-made disturbances. Examples of induced stresses are those that result from excavating, explosions, drilling, or pumping [42].
- *Residual Stress* – Stresses that remain in the rock mass after the original triggering mechanism has occurred. These stresses exist in equilibrium or at a near-equilibrium state within the rock mass [42].
- *Thermal Stress* – The stress state caused by temperature change [40].
- *Palaeostress* – A form of residual stress occurring as a result of palaeo-tectonic events [42].

Stress is neither a scalar nor vector quantity, but a tensor quantity. It contains a magnitude, direction, and plane under consideration [38]. Nine components of stress exist at any given point in a rock mass, as shown in Figure 2.6. A normal stress acts on the x, y, and z plane and two shear stresses act within each plane. In the case of excavation, unsupported surfaces become principal stress planes because no shear stress can act on them. This is important to consider when orienting underground openings.

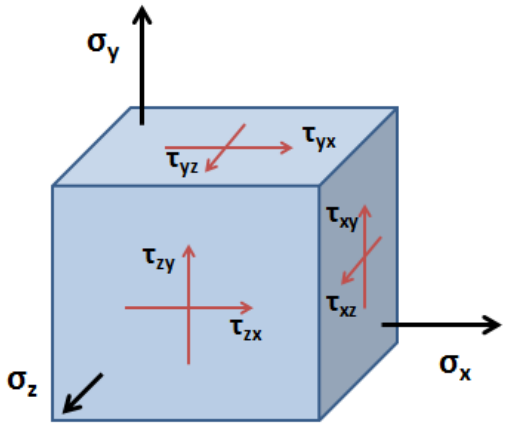

Figure 2.6: 3D Stress State

2.4.1 Failure Criteria

There are many criteria for explaining the failure of rocks due to stresses, known as failure criteria. Perhaps the most well-known of these criteria are the Mohr-Coulomb Failure Criterion, the Hoek-Brown Failure Criterion, and the Griffith Failure Criterion. The Mohr-Coulomb Failure Criterion, presented in 1900, suggests that materials fail due to a critical combination of normal stresses and shear stresses, rather than from one individual component. The Mohr-Coulomb Failure Criterion is written as:

$$\tau_f = C + \sigma \tan(\phi) \qquad \text{Equation 2.6}$$

where

τ_f = shear stress on the failure plane
C = cohesion
σ = normal stress on the failure plane
ϕ = angle of internal friction

The Mohr-Coulomb failure criterion can be visually represented by a Mohr's circle, shown in Figure 2.7. The line lying tangent to the circle is the failure criterion. Shear and normal stresses plotted below the failure criterion will not result in shear failure, whereas those plotted on the line will cause a shear failure along that plane. The angle of shear failure is given by Θ and the diameter of the Mohr's Circle is determined by the minor principle stress, σ_3, and the major principle stress, σ_1 [44].

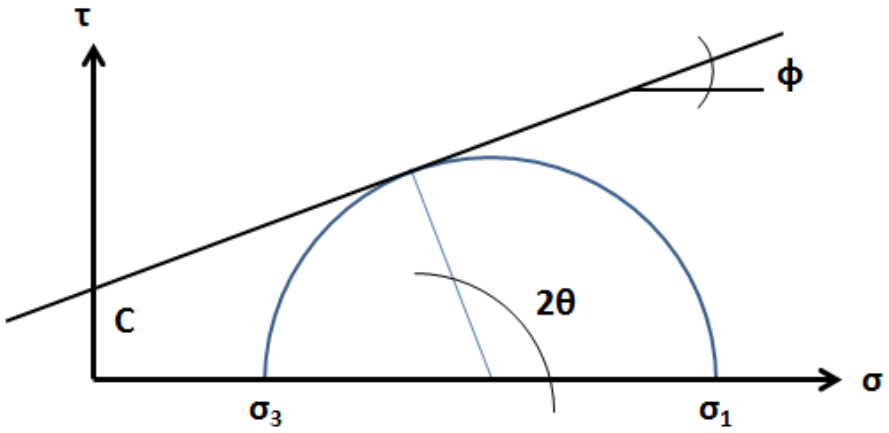

Figure 2.7: Mohr's Circle

In 1980, Evert Hoek and E. T. Brown introduced the Hoek-Brown Failure Criterion to provide an empirical relation for characterizing stress conditions that lead to failure in rock masses. The Hoek-Brown method can be used when either many joints are present in the rock mass or no joints are present. It cannot be used in anisotropic rocks. The Hoek Brown failure criterion is defined by the equation [45]:

$$\sigma_1 = \sigma_3 + \sigma_c \left(m \frac{\sigma_3}{\sigma_c} + s \right)^{0.5} \qquad \text{Equation 2.7}$$

where

σ_1= major principal stress

σ_3= minor principal stress

σ_c= uniaxial compressive strength of the intact rock

m and s are material constants, where s = 1 for intact rock.

The Griffith theory of fracture was developed to explain why brittle materials, such as glass, have a much smaller mechanical tensile strength than the theoretical molecular bond strength of that material [46]. Griffith uses a conceptual model of a two-dimensional rock containing randomly oriented thin cracks to derive a failure criterion for rock under both tensile and compressive loads. This leads to a nonlinear failure surface that is more realistic in several respects than the linear Coulomb Law. Griffith's Failure Criterion is given as:

$$(\sigma_1 - \sigma_3)^2 = 8T_0(\sigma_1 + \sigma_3)$$ Equation 2.8

where T_0 is the uniaxial tensile strength [47].

While these failure criteria may be often used, the Griffith, Hoek-Brown, and Mohr-Coulomb failure criteria only account for rock stress under conditions without confining pressure or with equal minor principal stresses. Unlike lab conditions, where σ_2 may be assumed to equal σ_3, actual rock masses will have varying minor principal stresses [48].

Chapters 1 and 2 References

[1] D. Reichle, *et al.*, "Carbon Sequestration Research and Development," U.S. Department of Energy 1999.

[2] S. Borenstein, "Markets for Anthropogenic Carbon Within the Larger Carbon Cycle," Energy Institute at Haas 2010.

[3] T. Hayward, "BP Statistical Review of World Energy," BP 2010.

[4] S. Bachu and J. J. Adams, "Sequestration of CO2 in Geological Media in Response to Climate Change: Capaity of Deep Saline Aquifers to Sequester CO2 in Solution," *Energy Conversion and Management,* vol. 44, pp. 3151-3175, 2003.

[5] J. Sminchak and N. Gupta, "Issues Related to Seismic Activity Induced by the Injection of CO2 in Deep Saline Aquifers," Battelle Memorial Institute, Columbus, Ohio.

[6] E. Sundquist, *et al.*, "Carbon Sequestration to Mitigate Climate Change," U.S. Geological Survey 2009.

[7] S. J. Friedmann. (2007) Geological Carbon Dioxide Sequestration. *Elements*. 179-184.

[8] C. Nicholson and R. L. Wesson, "Triggered Earthquakes and Deep Well Activities," *Pure and Applied Geophysics,* vol. 139, pp. 561-578, 1992.

[9] N. Deichmann and K. F. Evans, "Injection-Induced Seismicity: Placing the Problem in Perspective," presented at the European Seismological Commission 32nd General Assembly, Montpellier, France, 2010.

[10] S. A. Shapiro, *et al.*, "Fluid-Induced Seismicity: Theory, Modeling, and Applications," *Journal of Engineering Mechanics,* vol. 131, pp. 947-952, 2005.

[11] J. Suckale, "Moderate-to-large seismicity induced by hydrocarbon production," *The Leading Edge,* vol. 29, pp. 310-319, 2010.

[12] C. Kisslinger, "A review of theories of mechanisms of induced seismicity," *Engineering Geology,* vol. 10, pp. 85-98, 1976.

[13] J. E. Streit and A. F. Siggins, "Predicting, Monitoring, and Controlling Geomechanical Effects of CO2 Injection," presented at the Greenhouse Gas Control Technologies, 7th International Conference on Greenhouse Gas Control Technologies, Vancouver, 2004.

[14] S. C. Maxwell and T. I. Urbanic, "The role of passive microseismic monitoring in the instrumented oil field," *The Leading Edge,* vol. 20, pp. 636-639, 2001.

[15] E. L. Majer, *et al.*, "Induced Seismicity Associated with Enhanced Geothermal Systems," *Geothermics,* vol. 36, pp. 185-222, 2007.

[16] S. Solomon, "Carbon Dioxide Storage: Geological Security and Environmental Issues - Case Study on the Sleipner Gas field in Norway," Bellona 2007.

[17] P. N. Price, *et al.*, "Carbon Sequestration Risks and Risk Management," 2008.

[18] J. C. Russ, *The Image Processing Handbook*: CRC Press, 2011.

[19] T.-w. Lo and P. Inderwiesen, *Fundamentals of Seismic Tomography* vol. 6, 1994.

[20] G. Nolet, *Seismic Tomography*. Dordrecht: D. Reidel Publishing Company, 1987.

[21] E. Wielandt, *New Manual of Seismological Observatory Practice*. Potsdam: GFZ, 2002.

[22] S. Stein and M. Wysession, *An Introduction to Seismology, Earthquakes, and Earth Structure*: John Wiley and Sons, 2009.

[23] K. Luxbacher, *et al.*, "Time-Lapse Tomography of a Longwall Panel: A Comparison of Location Schemes," presented at the 26th International Conference on Ground Control in Mining, Morgantown, West Virginia, 2007.

[24] T. I. Urbancic and J. Rutledge, "Using microseismicity to map cotton valley hydraulic fractures," *SEG Technical Program Expanded Abstracts,* vol. 19, pp. 1444-1448, 2000.

[25] J. P. Verdon, *et al.*, "Passive Seismic Monitoring of Carbon Dioxide Storage at Weyburn," *The Leading Edge,* vol. 29, pp. 200-206, 2010.

[26] K. Luxbacher, *et al.*, "Three-dimensional time-lapse velocity tomography of an underground longwall panel," *International Journal of Rock Mechanics and MIning Sciences,* vol. 45, pp. 478-485, 2008.

[27] W. Sachse, *et al.*, *Acoustic Emission: Current Practice and Future Directions*: ASTM International, 1991.

[28] H. M. Benz, *et al.*, "Three-dimensional P and S wave velocity structure of Redoubt Volcano, Alaska," *Journal of Geophysical Research,* vol. 101, pp. 8111-8128, 1996.

[29] N. Barton, *Rock Quality, Seismic Velocity, Attenuation and Anisotropy*: CRC Press, 2006.

[30] S. Persoglia, *et al.*, "4-D Seismics, Gas-Hydrate Detection and Overpressure Prediction as a Combined Methodology for Application to CO2 Sequestration," 2006.

[31] R. A. Chadwick, *et al.*, "Review of monitoring issues and technologies associated with the long-term underground storage of carbon dioxide," *Geological Society Special Publications*, 2009.

[32] F. Waldhauser and W. L. Ellsworth, "A Double-Difference Earthquake Location Algorithm: Method and Application to the Northern Hayward Fault, California," *Bulletin of the Seismological Society of America*, vol. 90, pp. 1353-1368, 2000.

[33] R. Zhou, *et al.*, "Microseismic event location for monitoring CO2 injection using double-difference tomography," *The Leading Edge*, vol. 29, pp. 208-214, 2010.

[34] S. Garg, *et al.*, *Oscillations and Waves*: PHI Learning, 2009.

[35] K. F. Graff, *Wave Motion in Elastic Solids*: Courier Dover Publications, 1975.

[36] J.-P. Cordier, *Velocities in Reflection Seismology* vol. 3: Springer, 1985.

[37] P. Bormann, *et al.*, *Seismic Wave Propagation and Earth Models*, 2002.

[38] J. A. Hudson and J. P. Harrison, *Engineering Rock Mechanics: An Introduction to the Principles*: Elsevier, 2000.

[39] B. Amadei and O. Stephansson, *Rock Stress and Its Measurement*: Chapman & Hall, 1997.

[40] J. A. Hudson, *et al.*, "ISRM Suggested Methods for Rock Stress Estimation -- Part 1: Strategy for Rock Stress Estimation," *International Journal of Rock Mechanics & Mining Sciences*, vol. 40, pp. 991-998, 2003.

[41] D. A. Nieuwland, *New Insights into Structural Interpretation and Modelling*: The Geological Society Publishing House, 2003.

[42] A. Zang and O. Stephansson, *Stress Field of the Earth's Crust*, 2010.

[43] "Geologic Carbon Sequestration Opportunities in Pennsylvania," Pennsylvania Department of Conservation and Natural Resources.

[44] B. M. Das, *Fundamentals of Geotechnical Engineering*, 2009.

[45] D. C. Wyllie, *et al.*, *Rock Slope Engineering: Civil and Mining*, 2004.

[46] R. K. Rowe, *Geotechnical and Geoenvironmental Engineering Handbook*, 2001.

[47] J. C. Jaeger, *et al.*, *Fundamentals of Rock Mechanics*, 2007.

[48] J. Thomas C. Chidsey, *et al.*, "Why Modelers Need to Look at the Rocks!: Examples from Greater Aneth Field, Paradox Basin, Utah," U. G. Survey, Ed., ed, 2007.

Chapter 3: Double-Difference Tomography Applied to Monitoring of Geologic Carbon Sequestration in the Aneth Oil Field, Utah

3.1 Abstract

Double-difference seismic tomography is performed on a carbon sequestration operation in the Aneth Oil Field in southeast Utah as part of a Department of Energy initiative on monitoring, verification, and accounting of sequestered CO_2. A total of 1,211 seismic events were recorded from a borehole array of 22 geophones. Aneth Unit data were divided into four time periods for time-lapse analysis. A low velocity zone spanning the lateral extents of the observable region, likely representing a CO_2 plume, is detected when considering voxels containing the highest ray path coverage. A series of synthetic tomography tests simulating different CO_2 plume sizes and locations was performed to assist in characterizing velocity changes associated with Aneth Unit data. Inferences about the existence of a CO_2 plume should be made by comparing actual data to synthetic data resulting from simulations performed under similar conditions. Considering synthetic simulation similarities and a derivative weight sum analysis, a CO_2 plume can be imaged within the Desert Creek reservoir, but the resolution of the CO2 plume is too low for proper monitoring, verification, and accounting of injected CO_2. Recommendations for improving CO_2 plume resolution, through double difference seismic tomography, are made to increase the ray path distribution throughout the Aneth Unit by varying geophone locations.

3.2 Introduction

Climate change is a significant international concern, often attributed to increasing concentrations of greenhouse gasses, namely Carbon Dioxide (CO_2), in Earth's atmosphere. Fossil fuels are responsible for the majority of anthropogenic CO_2 emissions, but also sustain the global economy. This conflict has created one of the greatest geo-political environmental issues

in recent history. One method for reducing the amount of CO_2 released into the atmosphere is geologic carbon sequestration. Geologic carbon sequestration is the capture of CO_2 before it reaches the atmosphere, and its storage under deep geologic formations, such as depleted oil reserves, unmineable coal seams, or deep saline formations. It is important to monitor, verify, and account for CO_2 during injection and post-injection. One tool that can be used to perform this task is seismic tomography.

Generating an image, or tomogram, of an object by examining its reaction to the passive, probing energy from an external source is the foundation of tomography [19]. The external source, in the case of seismic tomography, is a seismic event. Seismic events can either be passive or active by nature. Active seismic event locations, artificially created and with a known epicenter, have been used in the past to image individual pillars or tunnel stress distribution, but are labor-intensive, and therefore impractical for long-term monitoring programs [23]. Passive seismic events are seismic events already occurring near the location of interest, possibly induced by humans through mining, fluid injection, or other engineering projects. Passive microseismic events are ideal for noninvasive, remote, time-lapse monitoring [26], as they allow for continuous observation of stress levels, fluid migration, or other time-dependent analyses.

Fluid displacement within a rock mass is capable of being imaged through tomography. Rocks in the subsoil may be saturated with brine, which has a specific associated p-wave velocity. If brine is displaced by a fluid with different elastic properties, the p-wave velocity of waves traveling through that medium will change. This is useful for carbon sequestration, as CO_2 different elastic properties than brine. The increased compressibility of CO_2 will result in subtle velocity changes in the host rock, which can then be imaged through the use of tomography [30].

This thesis will demonstrate the degree to which sequestered CO_2 can be monitored, verified, and accounted for in the Aneth Unit through time-lapse analyses of velocity changes and comparisons of synthetic plume simulations to Aneth Unit data. Analysis of event, receiver, and travel time data provided for the Aneth Unit of the Aneth oil field is performed on a time-lapse basis to determine CO_2 plume extents, CO_2 concentration changes, and any leakage of CO_2 from the reservoir. Appropriate damping and smoothing values are selected to optimize the

performance of the velocity model reconstruction. Simulations with synthetic travel times for a variety of different CO_2 plume sizes and locations are also conducted to assist in the verification of results obtained from the Aneth Unit data.

3.2.1 Double-Difference Tomography

Double-difference seismic tomography is based on the assumption that two seismic waves propagating along the same path should generate similar travel times. Studies have shown that substantial improvements in both locating seismic events and increasing geologic velocity model resolution can be obtained through the use of simultaneous multiple event ray path analysis. For double-difference tomography, the absolute and differential travel times are used to reconstruct a three-dimensional velocity model as well as relocate seismic events. The double-difference is given by the equation

$$dr_k^{ij} = (T_k^i - T_k^j)^{obs} - (T_k^i - T_k^j)^{cal} \qquad \text{Equation 3.1}$$

where T_k^i is the arrival time of the seismic wave, emanating from location i, arriving at station k and T_k^j is the arrival time of the seismic wave, emanating from location j, arriving at station k. The difference between the calculated and observed arrival time offsets is dr_k^{ij} or the double-difference [49].

The double-difference tomography code, tomoDD, is being used to perform pseudo-bending ray tracing to calculate the travel times between seismic events and receivers. This code is based on hypoDD, a double-difference event location algorithm developed by Waldhauser and Ellsworth [50].

3.2.2 Site Description

The Aneth oil field, located in southeast Utah, shown in Figure 3.1, is part of ongoing carbon sequestration experiments conducted under the Southwest Regional Partnership on Carbon Sequestration (SWP), which is represented by state and federal agencies, universities, electric utilities, non-governmental organizations, coal, oil and gas companies, and the Navajo Nation [51]. The Aneth Oil Field is Utah's largest producer of oil, having produced over 440 million barrels since its discovery in 1956. The Aneth Unit, the northwestern part of the Aneth Oil Field, was selected by the SWP to demonstrate the monitoring, verification, and accounting of injected CO_2. The Aneth Unit was acquired from ChevronTexaco Exploration and Production Company in 2004 by Resolute Natural Resources Company and is jointly owned by both Resolute and the Navajo Nation Oil and Gas Company. The Aneth Unit was selected for this project for several reasons: the practice of CO_2 injection in neighboring parts of the oil field, the presence of a CO_2 source and pipeline nearby [52], the amount of remaining oil for enhanced oil recovery, and it represents the archetypal oil field of the western United States [53].

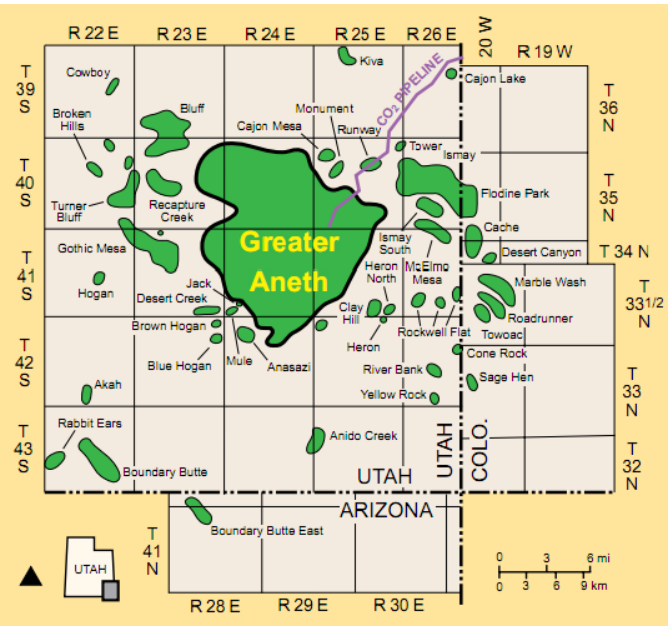

Figure 3.1: Location of the Greater Aneth Oil Field [48]

The Aneth Unit has produced roughly 149 million barrels of oil over an area that covers approximately 16,800 acres. Secondary recovery through water injection was first implemented

in the field in 1962, and CO_2 injection began in the Aneth oil field in 1985. CO_2 injection had not occurred in the Aneth Unit until 2007 [54]. The injection fluids being used at the site consist of salt water and CO_2. The salt water is produced through oil and gas production. The injection CO_2 is produced from the McElmo Dome Field located about 35 miles northeast of the Aneth Unit. The typical contents of the sequestered fluid are 72.6% CO_2, 15.4% methane, and 1.58% nitrogen, with the remainder being other hydrocarbon gases [55].

3.2.3 Geology

The Aneth Oil Field is located in the Pennsylvanian Paradox Basin of southeastern Utah. The basin is a stratigraphic trap, containing fractures and minor faults. The primary reservoir for the Aneth Unit is the Desert Creek carbonate, deposited on the Chimney Rock shale and overlain by the low-permeability Gothic shale, which acts as a caprock for the reservoir. Wells reveal a geology consisting of limestone, both oolitic and algal, and finely crystalline dolomite. Fractures in core samples are common, indicating minor faults that may affect fluid flow.

In addition to the Gothic Shale, the Desert Creek reservoir is overlain by approximately 800 feet of tight carbonates, evaporites, and fine-grained siliciclastics. Above that is up to 3,200 feet of shales, siltstones, sandstones, and evaporites, providing multiple layers of confinement against CO_2 migration [55].

The average vertical extent for the Desert Creek reservoir in the Aneth Unit is 14.9 meters (49 feet). The porosity of the reservoir is 10.3% with a permeability ranging from 6 to 27 millidarcies and water saturation of 23.3 percent [56]. Previous exploration has revealed the reservoir extents and geometry. The depth of the top of the Desert Creek reservoir is shown in Figure 3.2. The buoyancy of CO_2 should result in an upward migration of CO_2 until it is stopped by an impenetrable layer, the Gothic shale. If CO_2 migration is buoyancy driven, accumulation would most likely occur in the 1,708 to 1,702 meters in depth zone.

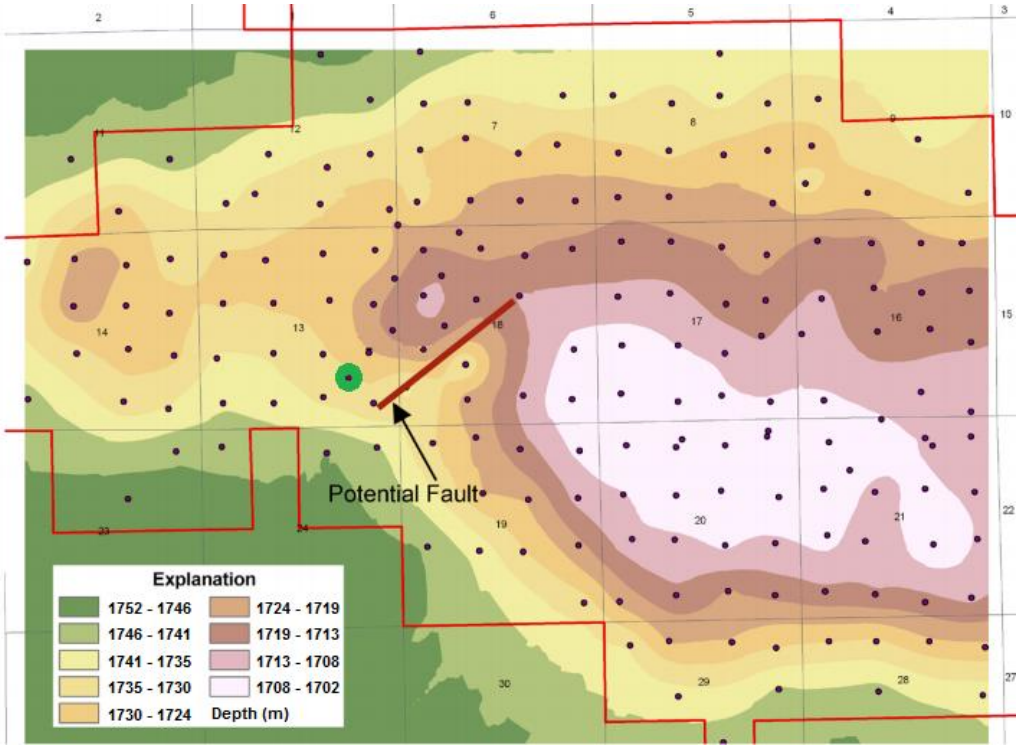

Figure 3.2: Depth of the Top of the Desert Creek Reservoir [48]

3.2.4 Microseismic Monitoring

There has been a history of monitoring at the Aneth Unit and Greater Aneth oil field. Since 2006, there have been several monitoring programs in place in the Aneth Unit for the purpose of monitoring CO_2. Establishing a background was performed through 3-D seismic reflection imaging surveys, passive seismic monitoring, vertical seismic profiles (VSP), crosswell seismic imaging, active doublet imaging, groundwater chemical analysis, and remote sensing. Time-lapse vertical seismic profile surveys, conducted from 2007 to 2009, found that injection of CO_2 registered an interpretable signal in VSP-CDP (vertical seismic profile to common depth point) images [57]. The monitoring well, C313SE, was used in many of these methods as well as the seismic monitoring associated with this tomographic study of the Desert Creek reservoir.

The geophone arrangement, in place at the C313SE monitoring well, is a 22-level vertical geophone array. The monitor well contains a 60-level geophone cable that extends to 1,704 meters in depth, with levels 15.2 meters apart. 16 geophones are evenly spaced between 1,445

meters and 1,704 meters in depth, with the remaining 7 geophones unevenly spaced between 805 meters and 1,445 meters in depth.

3.2.5 Microseismic Data

Microseismic monitoring, between April 25, 2008 and March 16, 2009, recorded 1,211 passive seismic events. As shown in Figure 3.3, the events are not evenly distributed over the monitoring period, possibly due to a changing rate of fluid injection into the reservoir. The moment scalars of the events range from 1.46×10^{7} to 1.44×10^{10} Nm, shown in Figure 3.4. P-wave arrival times and origin times were provided. A distance vs. time plot for the events is shown in Figure 3.5, reports a slowness of 0.207 s/km.

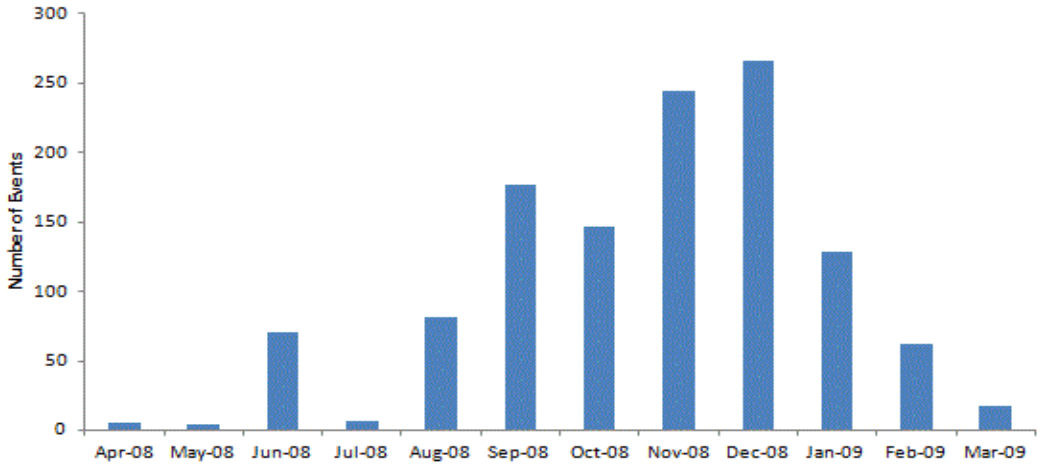

Figure 3.3: Event time histogram

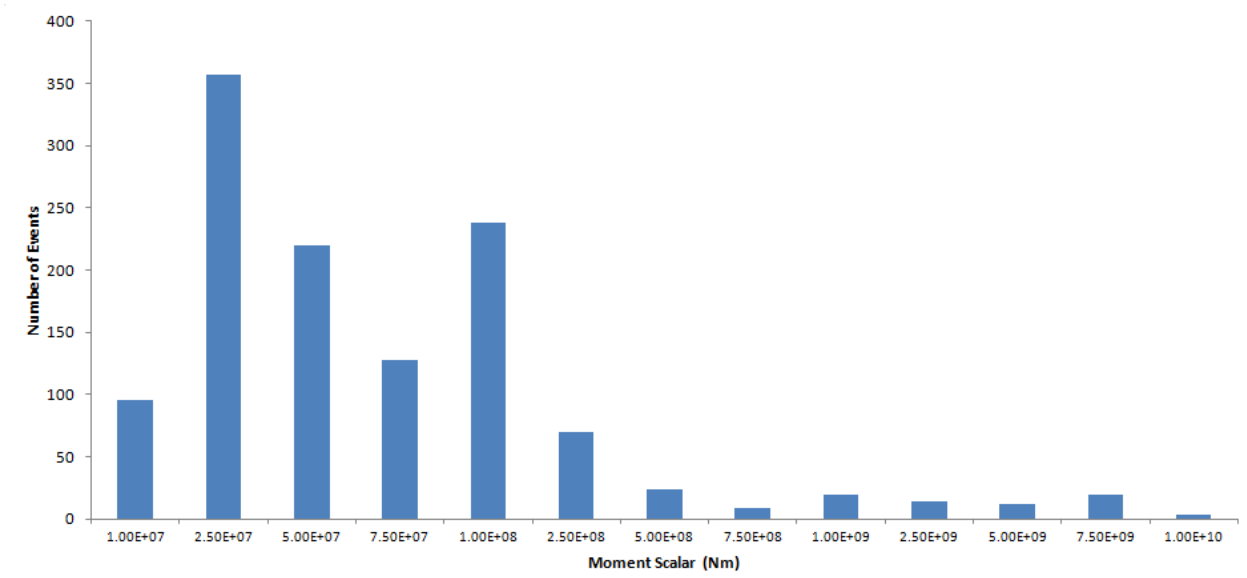

Figure 3.4: Moment scalar histogram

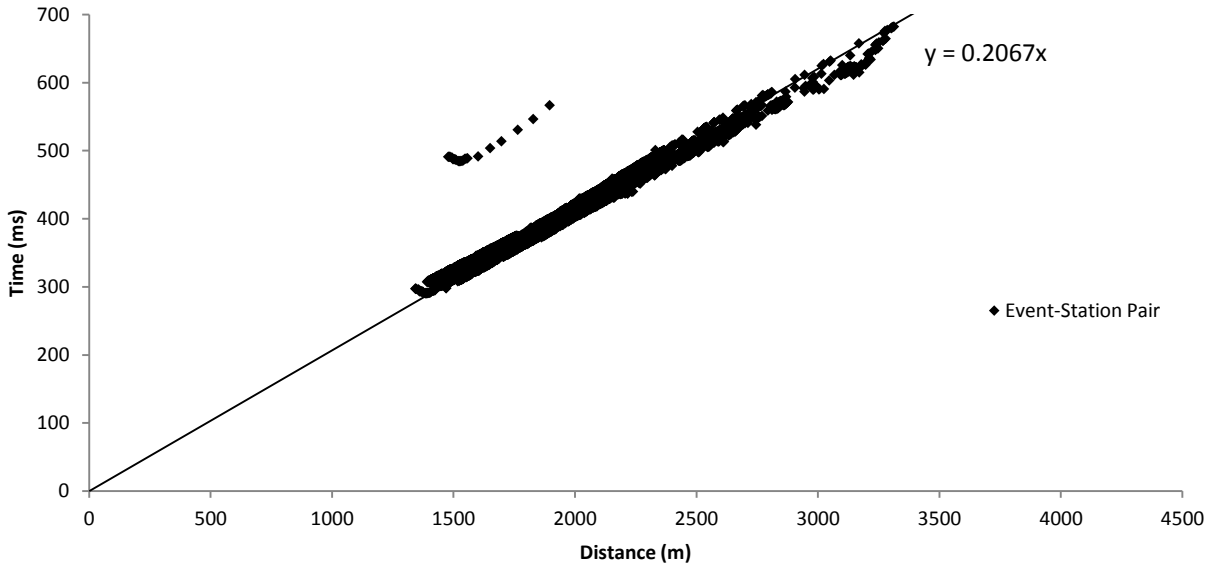

Figure 3.5: Distance vs. Time plot for P-wave travel times

The events form two clusters, shown in Figure 3.6: a northern cluster (approximately 4% of all events) and a southern cluster (approximately 96% of all events). The arrangement of the events suggest two NW-SE striking fault zones, one on the northern edge and one on the southern edge

of the Aneth Unit. Of these 1,211 events, 1,166 belong to the southern cluster, 44 belong to the northern cluster, and one event is located near the monitoring well.

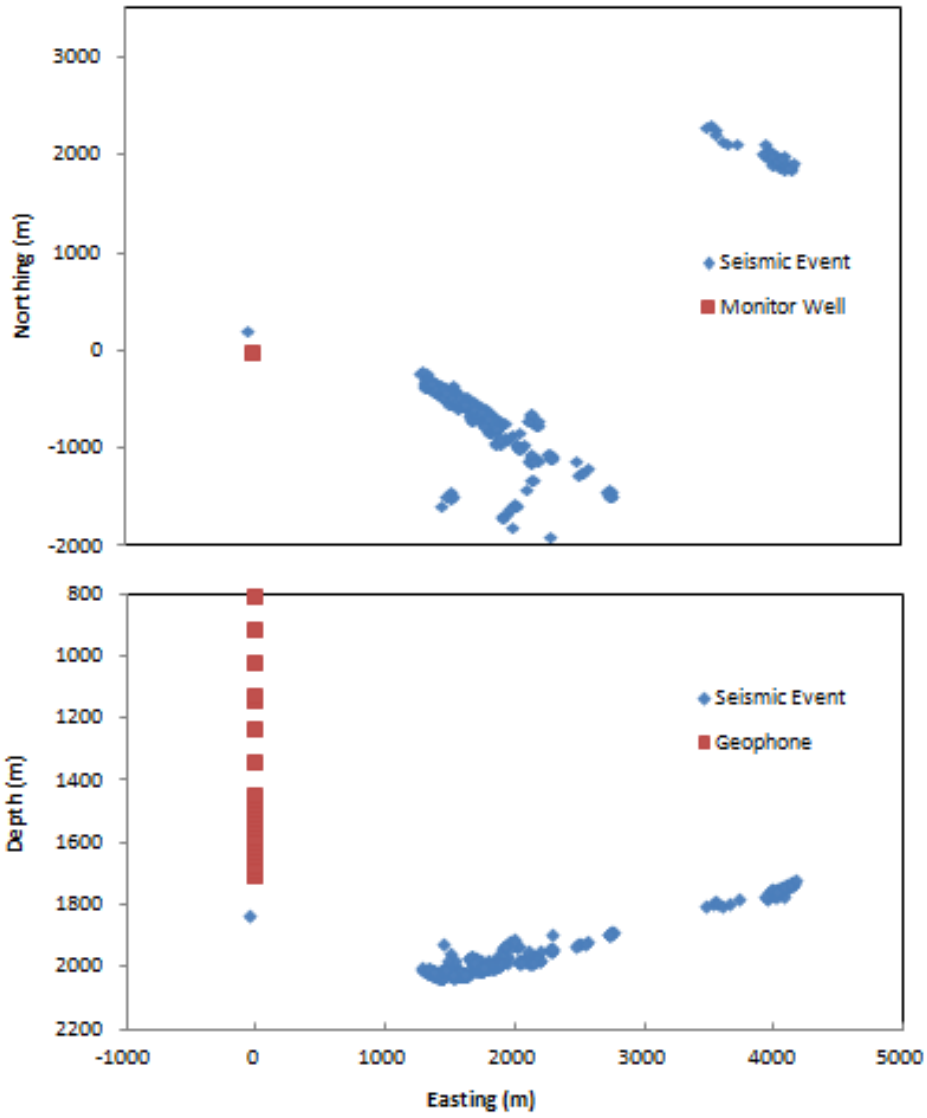

Figure 3.6: Event Locations

A layered velocity model was constructed based on prior knowledge of the reservoir geology, shown in Figure 3.7. This velocity model consists of five layers, with velocities ranging from 4.34 km/s to 5.27 km/s. The velocity model is constructed with a 40-node depth ranging from 800 meters to 2,150 meters. The velocity model also consists of a 40 by 40 northing-easting node distribution on the surface, encompassing an area of 13.6 km^2.

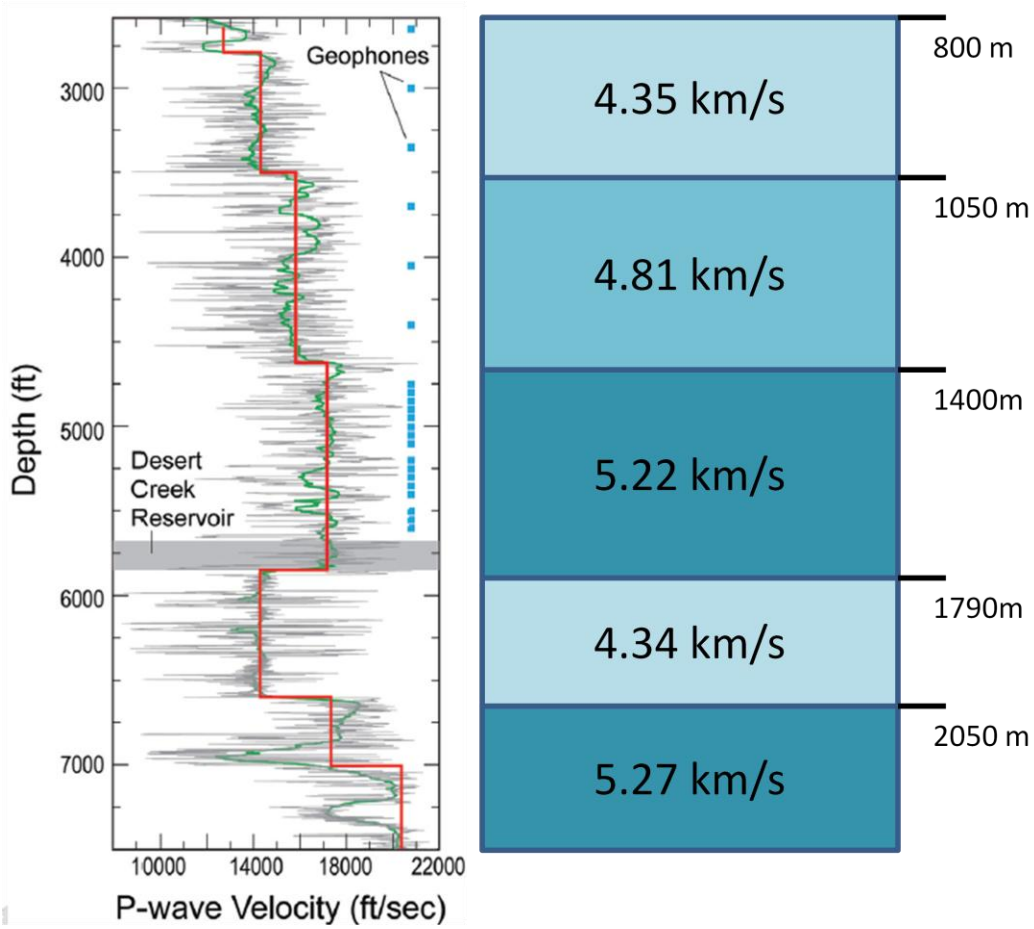

Figure 3.7: Aneth VSP [59] (left) and Derived Velocity Model (right).

3.3 Methods

3.3.1 Tomography Software Overview

Performing double-difference seismic tomography required the use of three primary programs. The first of these programs is tomoDD, a double-difference tomography program that jointly determines event locations and velocity structure by using both absolute and differential arrival time data [50]. The tomoDD code is based on the double-difference location algorithm hypoDD, written by Waldhauser [50].

TomoDD requires several input files, unique to each data set. These files include: events.dat, station.dat, phase.dat, dt.ct, tomoDD.inp and a MOD file. The events.dat and station.dat files establish the event and station locations, while the phase.dat file contains formatted travel time data. The dt.ct file contains the event pairs necessary to perform double-difference tomography. The tomoDD.inp file controls, among other parameters, the number of iterations performed, damping and smoothing values, and the maximum epicentral separation between events when creating pairs for relocation. The epicentral separation between events is set to decrease with increasing iterations, to allow for only the closest linked events being chosen to impact velocity model adjustments. The selection process for the number of iterations, damping values, and smoothing values will be discussed later in the Methods section. The MOD file represents the initial background velocity model. This file allows you to choose the number of nodes to be considered, the location of those nodes, and the initial velocity of the nodes. The dt.ct file is created by using the preprocessing program ph2dt.

Ph2dt searches through P and S wave phase data for event pairs with travel time information at common stations, and samples those data in order to optimize the quality of the phase pairs. A network of links is created between events, established by building links from each event to a specified maximum number of neighboring events within a specified search radius. If an event has more than a specified number of minimum linked phase pairs, it is considered to be a "strong" neighbor, whereas if it has fewer it is considered to be a "weak" neighbor. These specified values were, for this data set, chosen according to the hypoDD manual [58]. The manual suggests that for a small number of events that form a tight cluster, one could select all phase pairs by setting the minimum number of links to 1, the maximum number of links to the number of stations, and the maximum number of neighbors to the number of events [58]. The Aneth data, and synthetic data designed to closely match it, consist of several low-event time periods that form a tight cluster, so ph2dt input parameters were chosen according to the aforementioned guidelines. Sample input values for tomoDD and ph2dt are provided in Appendix A.

The second of the primary programs used is a travel time calculation code written in MATLAB. Synthetic tests require that appropriate travel times be determined between an event and receiver

when a velocity anomaly exists between them. The MATLAB travel time calculator, based on Dijkstra's Algorithm, creates a three-dimensional grid surrounding the events and receivers, consisting of a user-specified number of nodes. Each of these nodes creates a line segment to the neighboring nodes, which have velocities corresponding to the user-specified nodal velocities. The user-specified nodal velocities will reflect the velocity anomalies placed in the synthetic simulations. The travel-time calculator will search every possible travel path along this grid, and return the time of the path with the lowest absolute travel time. Due to processing constraints, the node geometry for every synthetic test was set to 20x20x20. Low resolution node geometries could create travel-time inaccuracies, as by decreasing the number of nodes, the approximation of actual event-receiver ray paths is worsened. The travel time calculation code is provided in Appendix B.

The third program used is Voxler 2, created by Golden Software. Voxler 2 allows for smooth two-dimensional or three-dimensional visual representations of numerical data. The resultant tomoDD velocity model file is formatted and displayed in Voxler 2. Tomograms displayed in this thesis are generated using a Gridder set to interpolate between data points using the inverse distance method and searching within a radius of twice the largest node spacing. Three-dimensional images can be difficult to represent in two dimensions, so all data presented in this thesis will be two-dimensional slices at a specified coordinate in the third dimension.

3.3.2 Damping and Smoothing

Damping and smoothing values were chosen to neither underfit nor overfit the data. The double-difference tomography program, tomoDD, was run at incrementally increasing damping and smoothing values, ranging from 10 to 1,000 for damping and 5 to 1,000 for smoothing. Figure 3.8 shows absolute variance and absolute mean for each point in these tests. For the purposes of damping and smoothing selection, only the 5.22 km/s zone, extending from 1,400 meters through 1,788 meters in depth, was considered. This is the layer that contains the Desert Creek reservoir, and is also most likely to contain any low velocity zone smearing which may occur.

Several outputs were compared for optimizing the damping and smoothing values. The maximum velocity, shown in Figure 3.9, and the minimum velocity, shown in Figure 3.10, should be kept within reasonable limits. One method for quantifying if the data have acceptable velocity change is reported in Figure 3.11, which reports the percentage of data within an expected 10% variation in velocity due to carbon sequestration. A 10% variation allows for velocities in the range of 4.70 km/s to 5.74 km/s. The minimum and maximum velocity change for each smoothing and damping value should be kept reasonably close to the background velocity, as neither the resolution of the velocity model nor known reservoir geology suggests that extreme deviations in velocity should be seen. A damping of 80 and smoothing of 100 was chosen to avoid underfitting or overfitting the data. The 1,000 and 500 damping values were found to be identical in absolute mean and variance, maximum recorded velocity, minimum recorded velocity, and percentage of velocities within expected limits, likely meaning the data are being overfitted. The 100 smoothing line shows the first separation from the 1,000 smoothing and 500 smoothing lines. The 100 smoothing line shows the first separation from this overfitting, and also represents the most linear relationship. A smoothing of 100 allows for separation from the 500 and 1,000 smoothing lines, likely overfitting the data, while also keeping the minimum values, maximum values, and overall velocity change within acceptable limits. A damping of 80 is chosen because it represents approximately the last point before the data begin to wander in Figure 3.8, representing underfitting of the data.

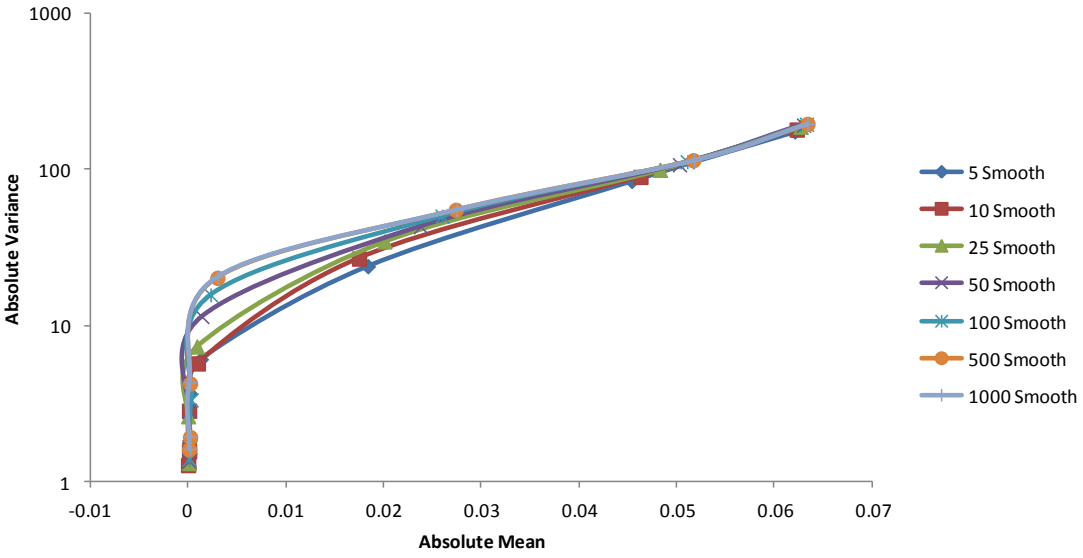

Figure 3.8: Absolute Variance vs. Absolute Mean

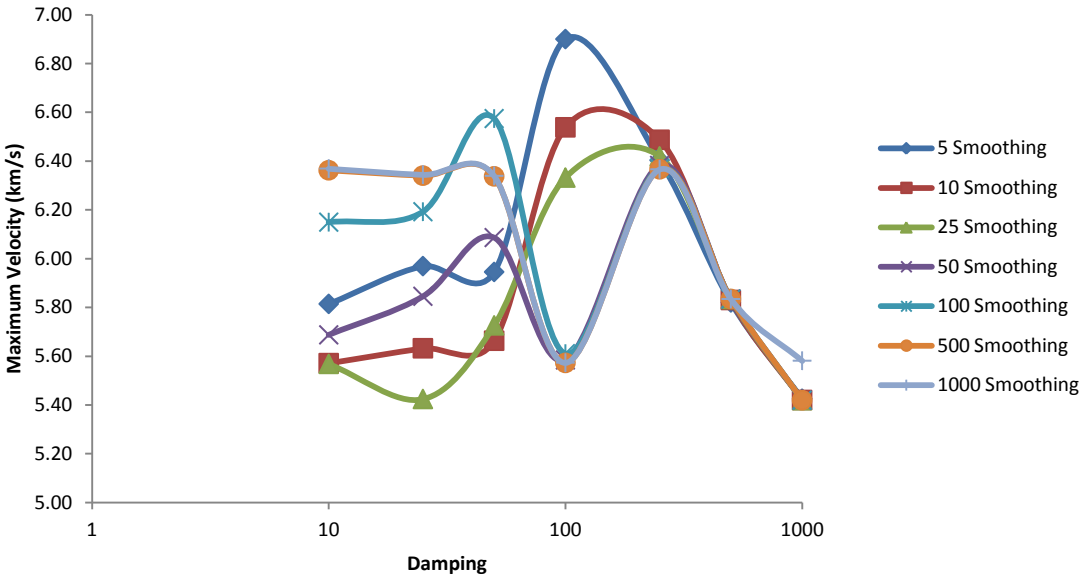

Figure 3.9: Maximum Recorded Velocity at Different Damping and Smoothing Values

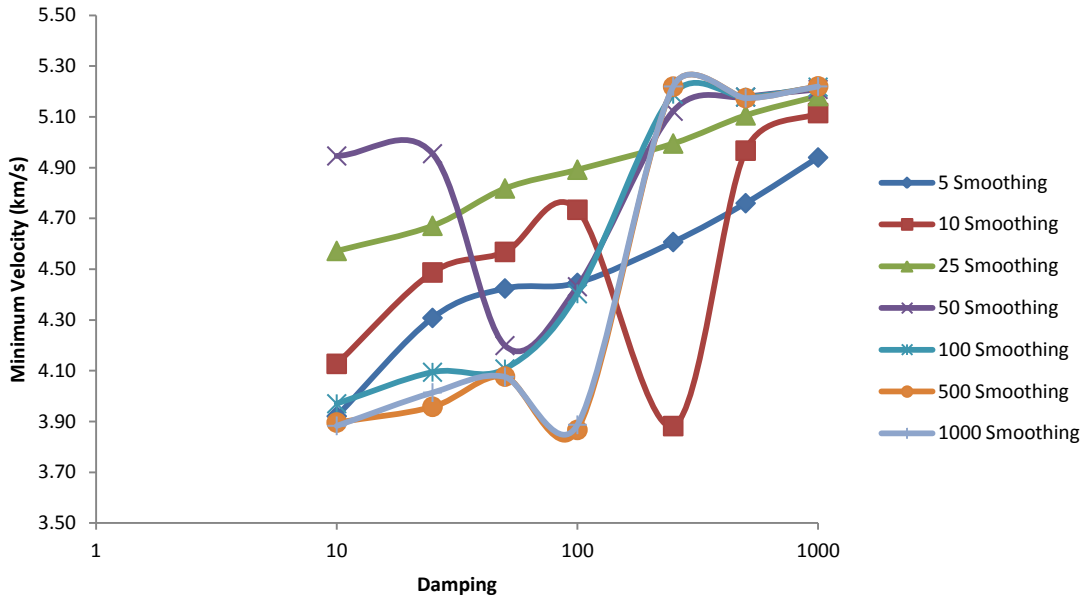

Figure 3.10: Minimum Recorded Velocity at Different Damping and Smoothing Values

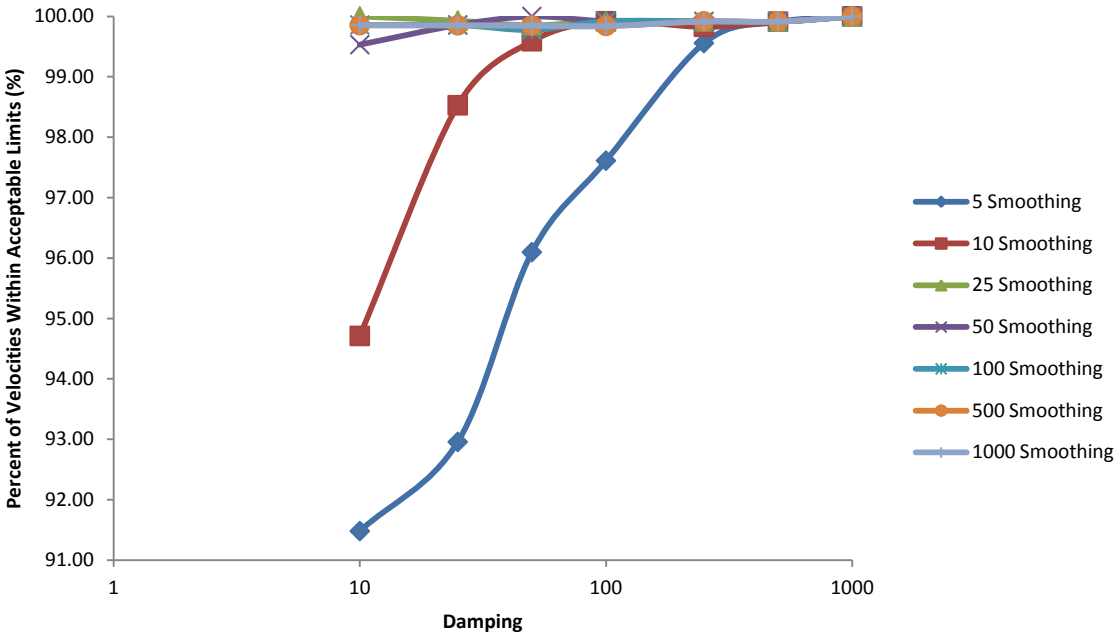

Figure 3.11: Percentage of Velocities Within Expected Variation Limits

In addition to changing smoothing and damping values, the number of iterative processes to cycle through was carefully selected. The RMSCT output through tomoDD indicates the RMS (Root Mean Squared) residual and its percent change from the previous iteration. This value

normally decreases with each iteration and can be used to locate the point at which further iterations are providing negligible change in the overall event relocation and velocity model adjustments are overfitting the data. The velocity model adjustments tend to converge faster than event relocations, so a stepping process of allowing for joint inversion and not allowing for joint inversion is performed. Tests were run for tomoDD inputs of 2, 3, and 5 iterations per joint inversion and non-joint inversion. The test with 3 iterations per joint and non-joint inversion is shown in Figure 3.12. This number of iterations was chosen as more than 3 iterations appeared to have a negligible impact on the RMSCT.

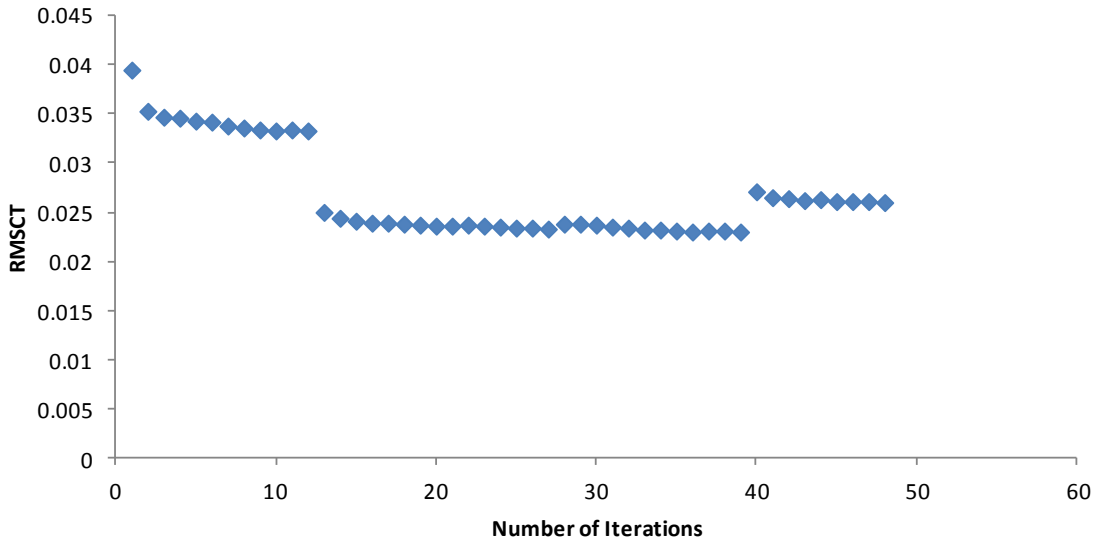

Figure 3.12: Iteration Analysis

3.3.3 Tomography Calibration

Calibration of both the MATLAB travel time calculator and tomoDD are performed. The ability to test the accuracy of tomoDD with this data set is limited, however one test is performed to ensure that tomoDD would not change the velocity model when no changes are necessary. The same event locations, receiver locations, and velocity model from the Aneth Unit are used. Using the squared distance between each event-receiver pair, and a desired average velocity of 5 km/s, each travel time is artificially set. The background velocity model for tomoDD was also set to a velocity of 5 km/s. Given that each travel time reflects a travel path of a 5 km/s average velocity and the velocity model contains a constant background velocity of 5 km/s, tomoDD should make no changes to the initial velocity model. TomoDD accurately made no changes to the initial velocity model, with a constant velocity of 5 km/s being reported for 100% of nodes.

For the synthetic travel time calculation calibration, two tests are performed to assess the potential for flaws in the calculation method that would prevent the accurate determination of travel times. The first test involves the creation of a 1000x1000x1000 meter cubic area containing 4,000 seismic events. Two receivers are placed within this region as well as a 200x200x200m low velocity zone, all shown in Figure 3.13. The background velocity for travel time calculation is 5 km/s and the low velocity zone is 3 km/s. Using a 20x20x20 node grid size, the travel-time calculator was able to output a travel-time input for tomoDD. Due to data constraints within tomoDD, the number of events was randomly reduced to 1,980, and then further reduced within the program to 1,091 events after relocation. The background velocity for tomoDD analysis is set to 4.56 km/s, to reflect the average velocity of the velocity model after travel times were calculated. A cross-sectional tomogram of this calibration is shown in Figure 3.14. The resulting low-velocity zone ranges from approximately 4.4 km/s to 4.9 km/s. The low velocity zone is not a cube, and also extends beyond the extents of the low-velocity cube. The symmetric nature of the velocity changes, and the existence of a low-velocity zone of the approximate dimensions centered in the correct location suggest that the travel time calculator may be able to provide an approximate representation of low-velocity zones.

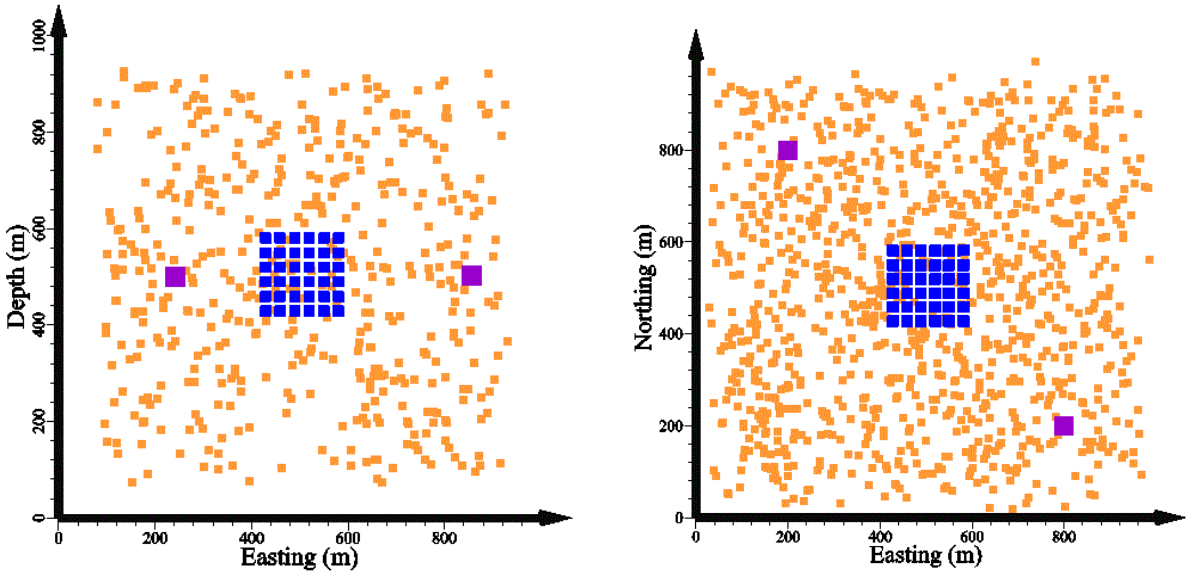

Figure 3.13: Cube Calibration Event and Receiver Arrangement. Events are shown in orange, receivers are shown in purple, and the low velocity zone is shown in blue.

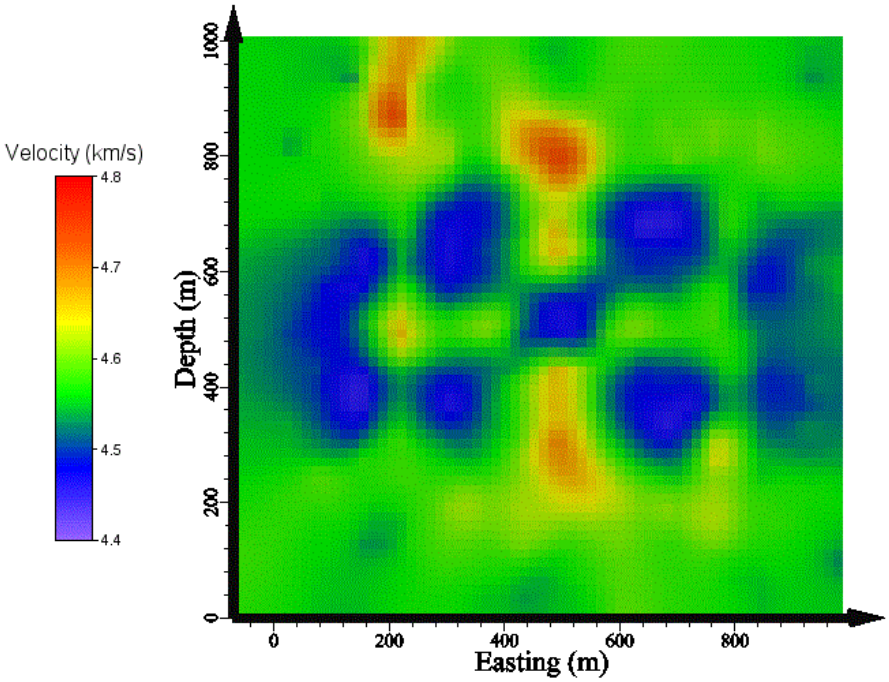

Figure 3.14: Cube Calibration Tomogram at 500 meters northing

The second calibration tests the ability of the travel time calculator to generate accurate travel times in a homogeneous velocity model, with no artificial low or high velocity zone to create

velocity anomalies. As with the tomoDD calibration, the event-receiver combination from Aneth is used, with the travel-time calculator velocity model having the same layered velocity model used with the actual Aneth data. This will be the control simulation to which synthetic tests, considering the Aneth event-receiver arrangement, can be compared. Some reduction in velocity is expected as a result of node-to-node travel paths rather than a continuous curve. Ideally, this velocity reduction would be very small and not reflected in the tomoDD output.

3.3.4 Synthetic Experimental Plumes

Synthetic plumes, designed to represent potential conditions, or assist in the understanding of velocity change in the Aneth Unit, are all created and processed in an identical manner. Event and station locations used in processing the original Aneth Unit data are used to assess the accuracy with which the current event-receiver arrangement can image the CO_2 accumulation in the oil field. The velocity model for the synthetic tests is the same layered velocity model provided for the Aneth Unit, with the exception of an artificially created low velocity zone at varying locations. These low velocity zones are assigned a 2 km/s velocity reduction from the background. A traditional plume shape is not assumed, nor is velocity dependent on position within the plume. The use of multiple injection wells and a changing caprock elevation are likely to create an unpredictable plume shape and CO_2 concentration distribution. A simple rectangular prism of low velocity is created instead to represent an area likely to be influenced by CO_2.

For all synthetic data post-processing, voxels with derivative weight sums (DWS) of zero will be excluded from the final results. The DWS is an indicator of the number of ray paths traversing a node, and can thus be considered a form of confidence in the value of that voxel. Voxels with a DWS of zero had no ray paths traverse them and remained unchanged, because no information can be inferred from the ray path behavior.

3.3.5 Differently Sized Synthetic Plumes

The first set of synthetic plumes is designed to test the appearance of a plume within the highest elevation portion of the Desert Creek reservoir. Figure 3.15 shows the DWS of the Aneth Unit data at 1,740 meters overlaying the Desert Creek reservoir elevation map shown in Figure 3.2. There is no ray path coverage for the majority of the high elevation portion of the Desert Creek reservoir. Through synthetic tests, it will be determined if plumes of varying radii are large enough to be detected with the given event-receiver arrangement if a CO_2 plume is residing in this region.

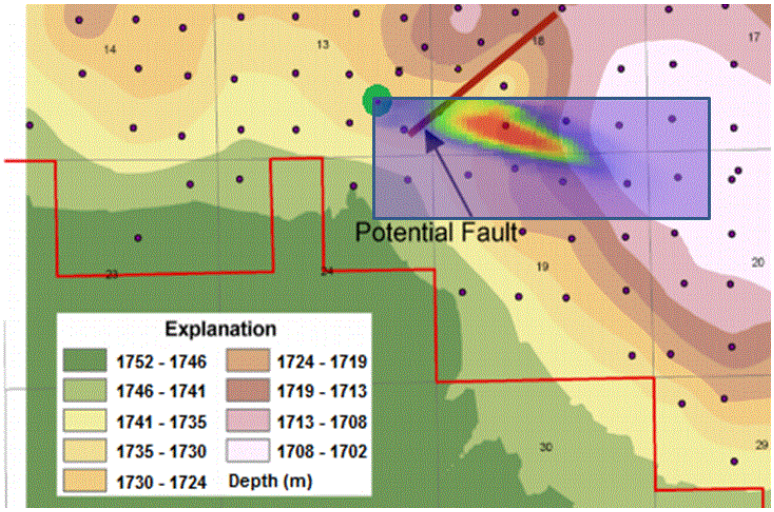

Figure 3.15: DWS Overlay of the Aneth Unit at 1,740 meter depth (Adapted from [48])

The low velocity zone varies in size for three separate scenarios: one with a 250 meter radius plume, another with a 500 meter radius plume, and a last test with a 1,000 meter radius plume. All of these different radii extend 100 meters vertically to surpass the average thickness of the Desert Creek reservoir. Each of these plume radii correspond to 500x500x100 meter, 1000x1000x100 meter, and 2000x2000x100 meter rectangular prism low velocity zones, and are all centered at 1,800 meters easting, -400 meters northing, and 1,770 meters in depth. All the plumes have a velocity reduction of 2 km/s from the background velocity. Plots of each different plume size in relation to the event and station locations are given in Figure 3.16.

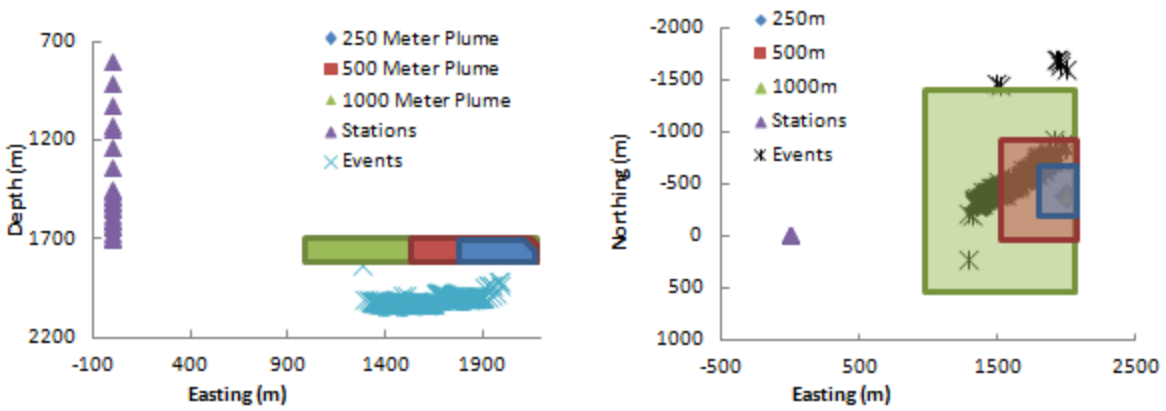

Figure 3.16: Locations and Extents of Differing Diameter Synthetic Plumes

To continue further investigating the ability of tomoDD to detect a low velocity zone with the given event-receiver arrangement, a plume with an infinite size in the northing and easting direction is created to simulate the complete saturation of the Desert Creek reservoir. A low velocity zone is created that reduces the background velocity by 2 km/s, extends infinitely in the northing and easting direction, and extends vertically 100 meters, from 1,720 meters to 1,820 meters in depth. These extents fully encompass the Desert Creek reservoir as well as up to 90 meters below the reservoir. The travel time calculator is used to generate travel times between the events and receivers, all of which involve travel paths traversing the low velocity layer.

3.3.6 Different Location Synthetic Plumes

The next three synthetic conditions vary the plume location rather than plume size. Using the Aneth Unit receiver and event locations, three different synthetic plume locations are analyzed. The locations chosen are not necessarily where CO_2 is expected to accumulate, but rather three locations at varying positions between the events and receivers where ray path coverage is high. Plumes in these locations are most likely to generate a velocity perturbation, however, the differences, or lack thereof, between the different plume location simulations should demonstrate the potential accuracy of tomography with the given event-receiver arrangement.

All the synthetic plumes are 500x500x100 meter rectangular prisms, and have a velocity reduction of 2 km/s from the background velocity. Plume location A is centered at 600 meters easting, -200 meters northing, and 1,600 meters in depth. Plume location B is centered at 800 meters easting, -300 meters northing, and 1,700 meters in depth. Plume location C is centered at 1,000 meters easting, -400 meters northing, and 1,800 meters in depth. The plume locations are shown in Figure 3.17.

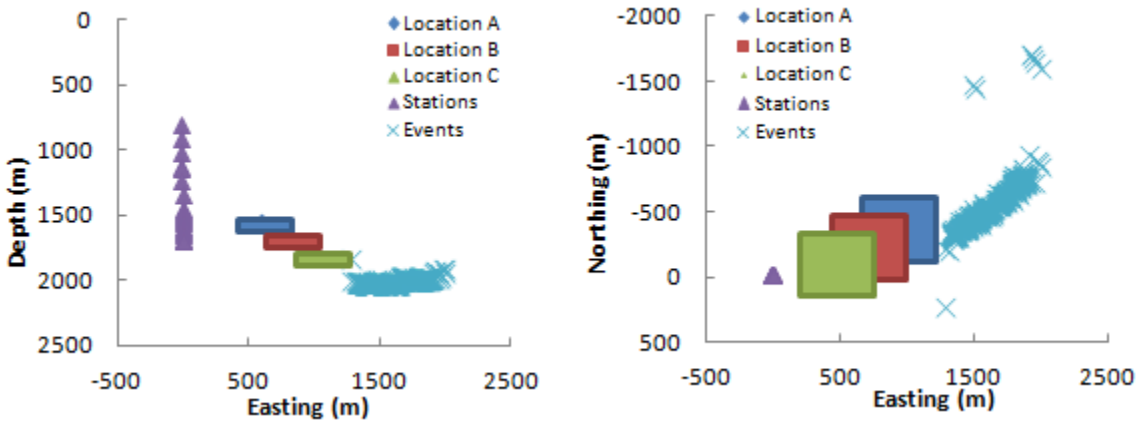

Figure 3.17: Plume Locations and Extents for Locations A, B, and C

3.3.7 Methods for Aneth Results

The processing of data for the Aneth Unit begins with refining the events provided. The northern cluster of events does not contain enough events to provide reliable ray path coverage of the desired area. The northern cluster and the event located near the monitor well are removed to allow for an increased resolution in the MOD file. The remaining 1,166 events were separated into 4 distinct time periods. The number of events in each time period and the dates encompassed are given in Table 3.1.

Table 3.1: Events Contained in Each Time Period

Time Period	Start Date	End Date	Number of Events
1	4/25/2008	8/31/2008	126
2	9/1/2008	10/31/2008	323
3	11/1/2008	12/31/2008	510
4	1/1/2009	3/16/2009	207

These time periods were selected to ensure that a sufficient number of events existed in each period for tomographic analysis, considering the removal of events during the relocation process.

The Aneth Unit data are treated in the same manner as the synthetic data for double-difference tomography. When choosing closely linked events, the maximum epicentral separation was given an initial value of 40 meters and later narrowed in tomoDD to 20 meters. The maximum number of neighbors was set to the number of events in that time period. The minimum number of links was set to 1, and the maximum number of links was chosen as the number of stations, 22. The background velocity model chosen was shown in Figure 3.7, and is the same velocity model used for the synthetic plume simulations.

A baseline velocity model for the Aneth Unit data will be assumed, performing a similar function as the control test for the synthetic plume simulations. There are no data provided for any period of time prior to CO_2 injection that could be used as a baseline, however, the first time period should most closely simulate the absence of a plume. Subtracting the initial time period from the remaining time periods should eliminate some program irregularities and highlight areas of increasing CO_2 concentration.

Nodes with DWS values of 0 are removed from the velocity model during post-processing. As part of a separate analysis, nodes with the lowest confidence values are also removed. Three confidence thresholds are set: the bottom 25%, 50%, and 75% DWS values. Tomograms will be shown that include only the most confident voxels: the top 25%, 50%, and 75% confidence levels. The limited data remaining after a confidence limit is established has the potential to result a low resolution tomogram, creating a net loss of accuracy in the resultant tomograms.

3.4 Results and Discussion

3.4.1 No Low Velocity Zone (Control)

To better understand the results from tomoDD, an analysis of the synthetic data, designed to simulate Aneth conditions, is presented first. The first synthetic test is one in which no low velocity zone was placed in the synthetic travel time calculation velocity model. Due to the layered nature of the velocity model, two tomograms of this simulation are shown. The first tomogram narrows the velocity range to isolate the 1,789 meter to 2,000 meter layer, which will be referred to as the 1,789 layer. Isolating this layer allows for visual representation of velocity changes that would otherwise be too small to see with the velocity scale encompassing the entire range of velocities present in the velocity model. The second tomogram narrows the velocity range to isolate the 1,400 meter to 1,789 meter layer, which will be referred to as the 1,400 layer. Tomograms for both of these layers are shown in
Figure 3.18. Isolations of the remaining layers are not performed, as artificial low velocity zones were not placed near these regions.

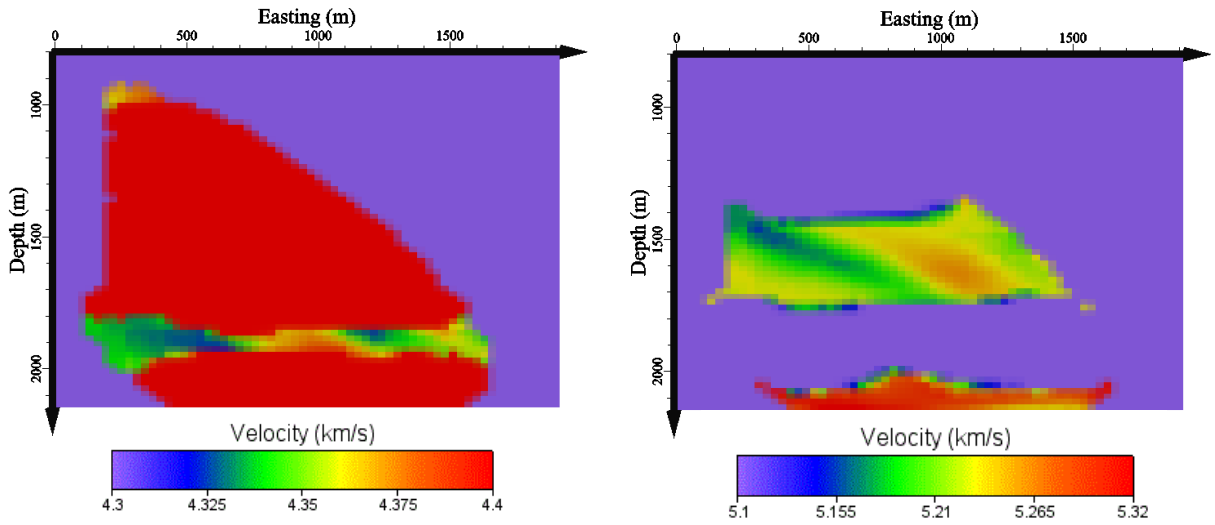

Figure 3.18: Synthetic control tomograms for 1,789 layer (left) and 1,400 layer (right)

Figure 3.19 shows the difference between this control test and the original background velocity model when interpolated in Voxler 2. There are several low and high velocity changes between

the two velocity models. The effect of these zones should be mitigated if the control is subtracted from the synthetic tests, however, additional scrutiny should be given to any velocity anomalies detected in these zones. The velocity scale chosen for this comparison and subsequent comparisons is intended to highlight areas of decreasing velocity, increasing velocity, and areas with negligible change. Regions colored in black represent a change towards a lower velocity, while regions colored in white represent a change towards a higher velocity. The magnitude of these changes is not indicated on the comparison tomograms.

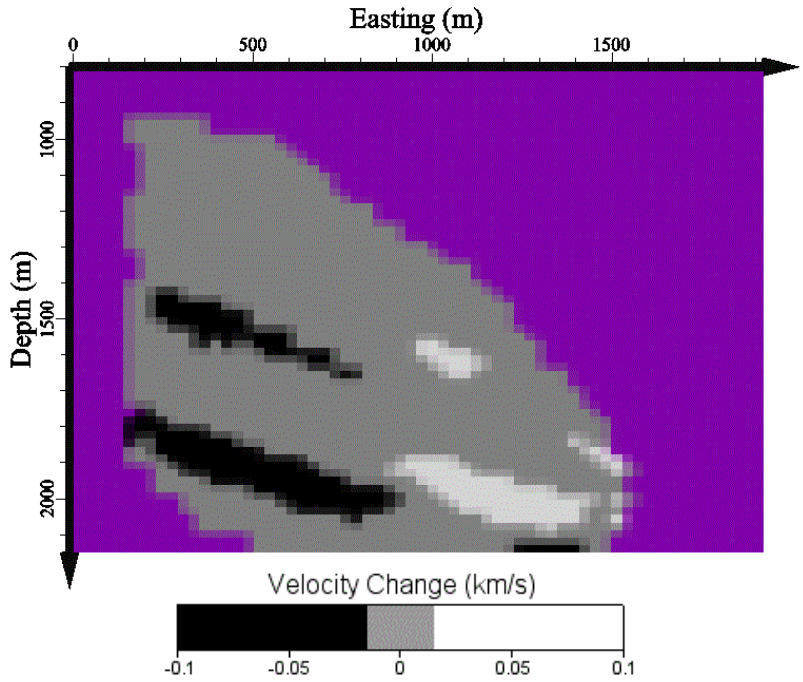

Figure 3.19: Velocity change between the control test and the background velocity model at -300 meters northing

The application of double-difference tomography to this data set has generated an image showing velocity discontinuities within homogeneous velocity layers. Some velocity anomalies are expected, due to the travel time calculation method and slight velocity model differences between applications. The node-based calculation method of the travel time calculator will produce travel-times with inaccuracies as a function of the number of nodes used, which could account for these anomalies. The background velocity model used in the travel-time calculator also differs slightly from the background velocity model used in tomoDD, in that layer boundaries may be misplaced by several meters due to the method with which the travel-time

calculator generates a velocity model. The purpose of running a simulation with no low velocity zone is to help reduce the impact of these velocity anomalies on future tests by providing a baseline velocity model which can be subtracted from the remaining synthetic tests. The difference between the "No Low Velocity Zone" test and test with a low velocity zone should highlight the impact that low velocity zone has on the velocity model, while minimizing the impact of experimental errors.

3.4.2 Differing Synthetic Plume Locations

The first set of synthetic simulations varies the location of the plume. The first of these locations is Location A. A 500x500x100 meter low velocity zone is placed in Location A, centered at 600 meters easting, -200 meters northing, and 1,600 meters in depth. Three tomograms are presented for this test. Figure 3.20 shows the isolated-layer velocity structure of the target area. Figure 3.21 shows the difference between Location A and the baseline tomogram without a low velocity zone.

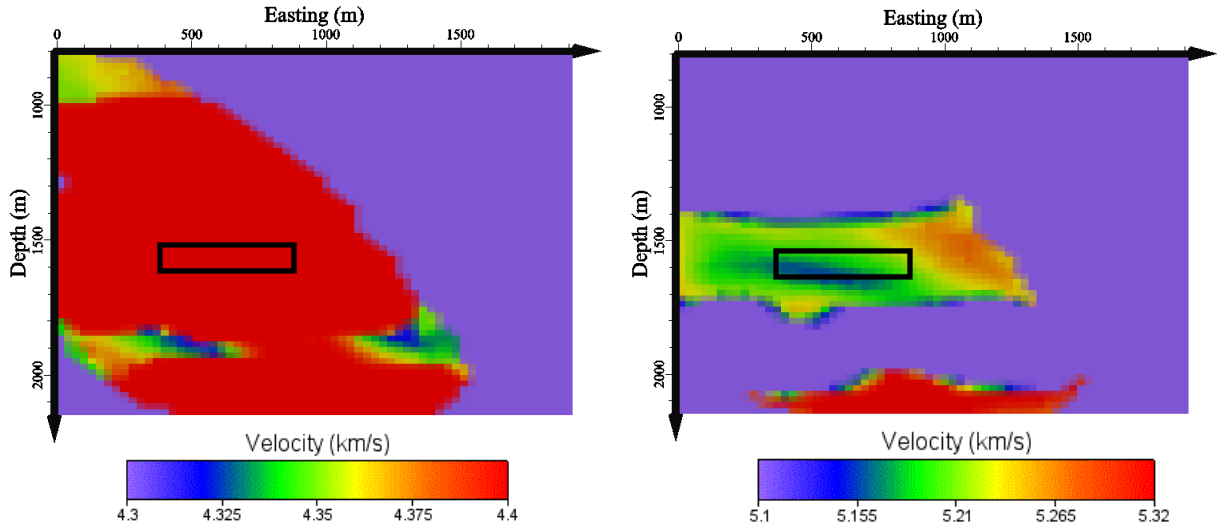

Figure 3.20: Tomograms of the 1,790 layer (left) and 1,400 layer (right) for Location A at -200 meters northing

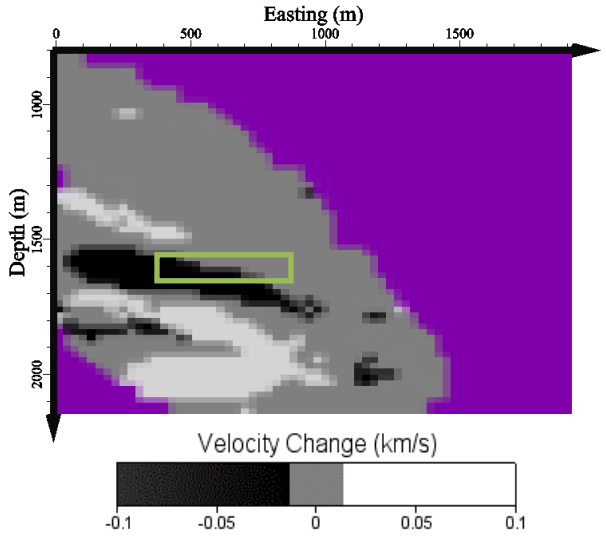

Figure 3.21: Difference between Location A and the control at -200 meters northing

Figure 3.21 shows a low velocity zone near the appropriate location with a slightly larger size. The location of the synthetic plume was purposefully designed to be easy to detect due to its placement directly between the events and geophones. With the given event-receiver arrangement, it was expected that a low velocity zone would be detected between the events and receivers, but that the low velocity zone would be stretched between those two locations. These results are encouraging, as the low velocity zone was located more accurately than anticipated, and would suggest that the given event-receiver arrangement can determine the plume location in the easting direction better than anticipated. The low velocity zone detected here exhibits a large amount of smearing, spanning the entire diagonal, northing extents between the events and receivers.

The second location is Location B. A 500x500x100 meter low velocity zone is placed in Location B, centered at 800 meters easting, -300 meters northing, and 1,700 meters in depth. Three tomograms are presented for this test. Figure 3.22 shows the isolated-layer velocity structure of the target area. Figure 3.23 shows the difference between Location A and the baseline tomogram without a low velocity zone.

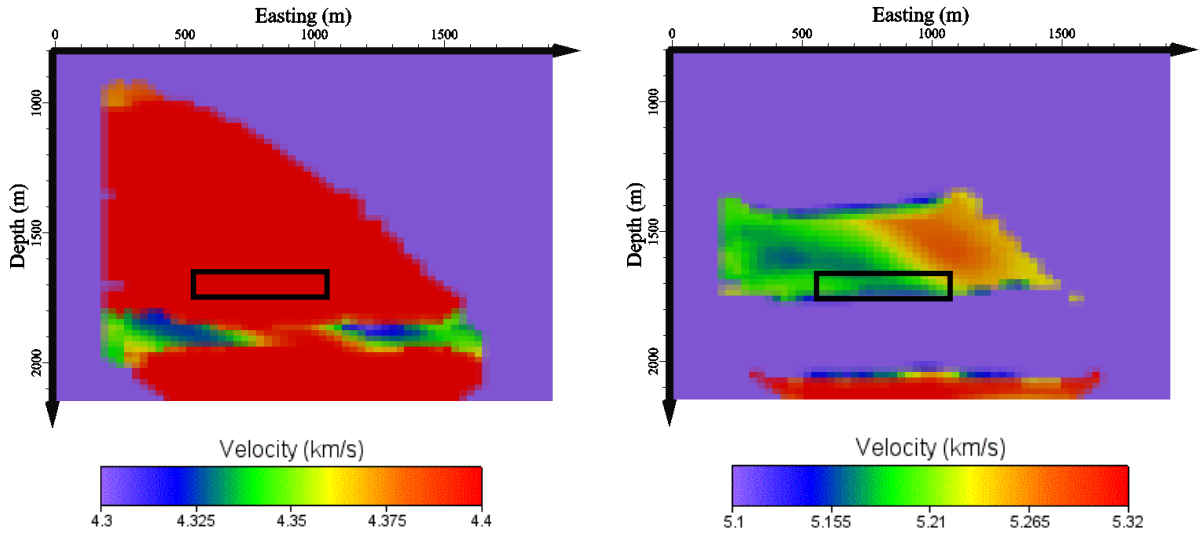

Figure 3.22: Tomograms of the 1,790 layer (left) and 1,400 layer (right) for Location B at -300 meters northing

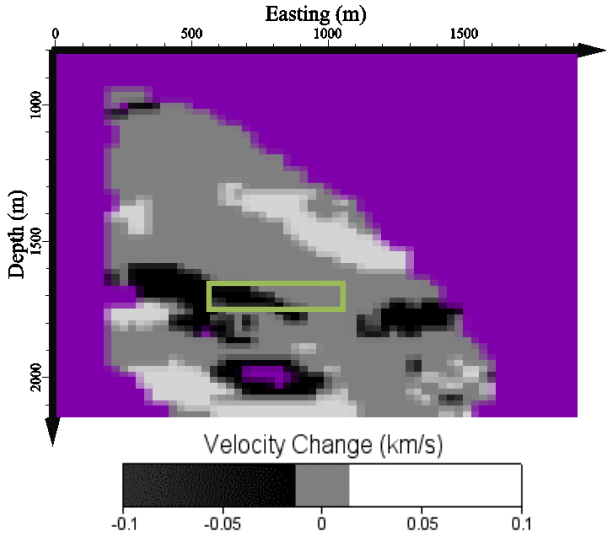

Figure 3.23: Difference between Location B and the control at -300 meters northing

The synthetic plume at Location B is partially represented, but shifted slightly west. This could be, in part, due to the proximity of the plume to the velocity layer boundary. Another explanation for anomalous behavior of a plume at this location is the presence of an anomalous low velocity zone at this location in the control test. Similar to the Location A tomograms, the Location B tomograms show significant smearing of a low velocity zone when viewing multiple northing slices.

The third location is Location C. A 500x500x100 meter low velocity zone is placed in Location C, centered at 1,000 meters easting, -400 meters northing, and 1,800 meters in depth. Three tomograms are presented for this test. Figure 3.24 shows the isolated-layer velocity structure of the target area. Figure 3.25 shows the difference between Location C and the baseline tomogram without a low velocity zone.

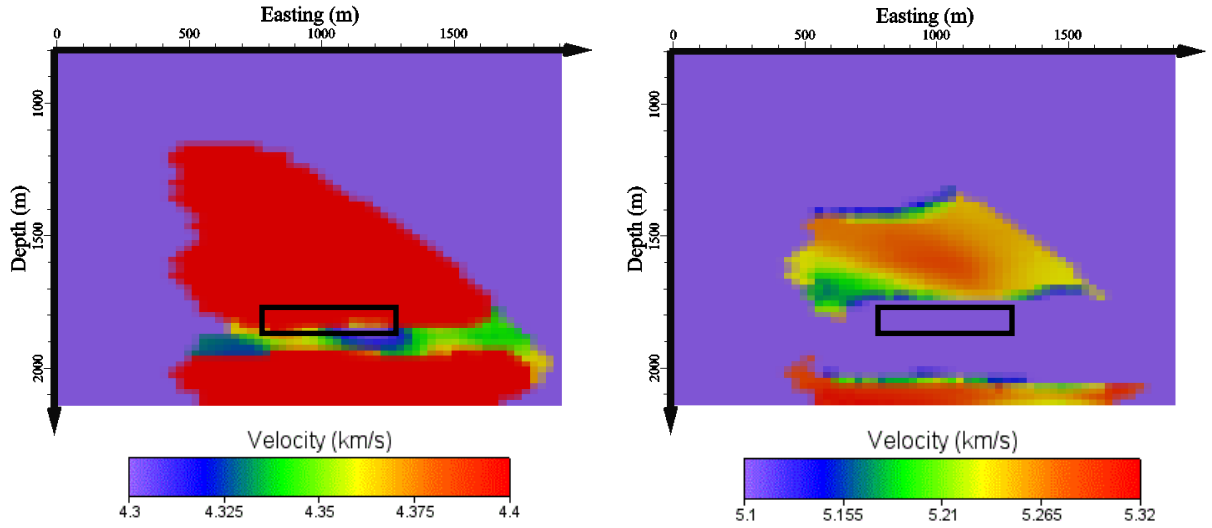

Figure 3.24: Tomograms of the 1,790 layer (left) and 1,400 layer (right) for Location C at -400 meters northing

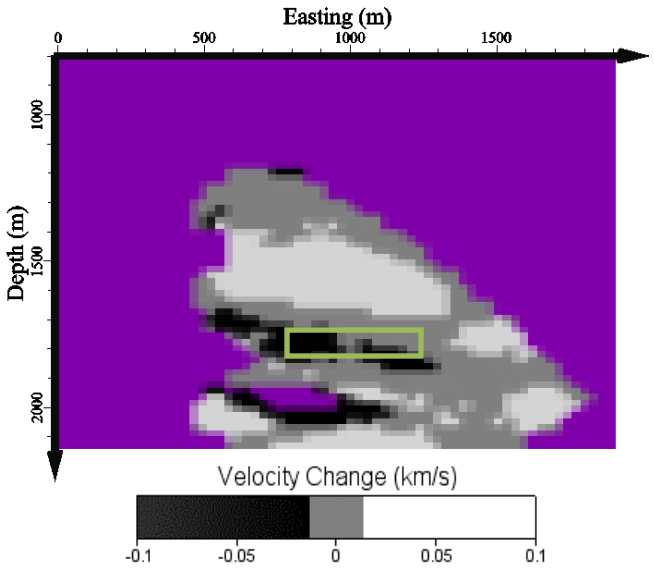

Figure 3.25: Difference between Location C and control at -400 meters northing

Location C is fairly well represented in Figure 3.24, as it is the only of the three different locations to have a significant low velocity presence in the 1,790 layer. The easting and depth position of this low velocity zone was slightly shifted, as could be expected, but the dimensions are approximately correct. The presence of a low velocity zone in these tomograms suggest that even in the presence of a changing velocity layer, the velocity reduction associated with a CO_2 plume may still be detectable. Similar to Location A and B, significant vertical smearing was detected between the events and receivers for Location C.

3.4.3 Different Sized Synthetic Plumes

The second set of synthetic tests involves performing double-difference tomography with various plumes of different sizes. The first low velocity zone, simulating a 250 meter radius plume placed at the likely CO2 accumulation point, was unable to be detected. The travel times associated with the 250 meter radius plume are identical to those of the control test, suggesting that a plume of this size cannot be detected in its current location. The second low velocity zone, simulating a plume with a 500 meter radius, and vertical extent of 100 meters is centered at 1,800 meters easting, -400 meters northing, and 1,770 meters in depth. Figure 3.26 shows the isolated-layer velocity structure of the target area. Figure 3.27 shows the velocity difference between the 500 meter radius plume and the baseline tomogram not containing a low velocity zone.

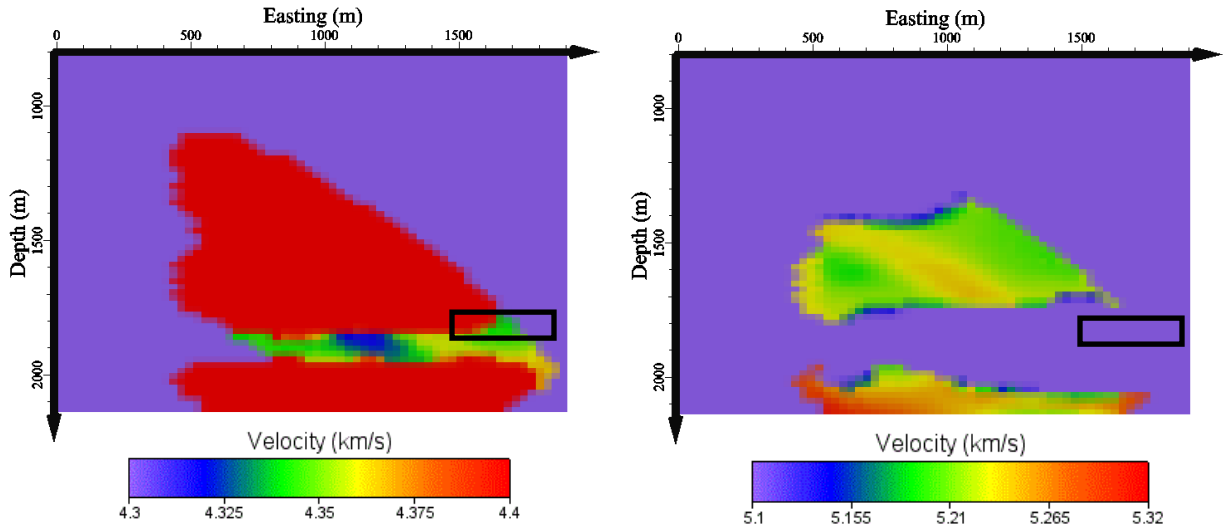

Figure 3.26: Tomograms of the 1,790 layer (left) and 1,400 layer (right) for a 500 meter radius plume at -400 meters northing

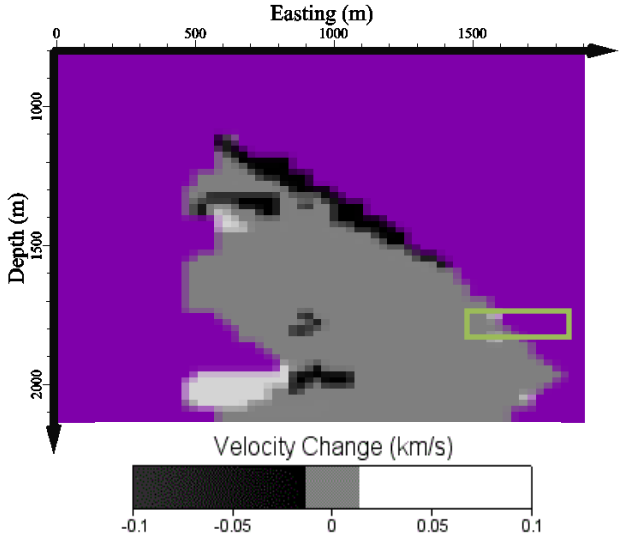

Figure 3.27: Difference between a 500 meter radius plume and the control at -400 meters northing

There is no apparent low velocity zone for the 500 meter radius plume simulation. There also appears to be very little overall change to the velocity model. The likely explanation for both of these observances is the size of the plume not being large enough to experience a significant amount of ray path coverage.

The third low velocity zone, simulating a plume with a 1,000 meter radius, and depth of 100 meters, is centered at 2000 meters easting, -400 meters northing, and 1,770 meters in depth. Figure 3.28 shows the isolated-layer velocity structure of the target area. Figure 3.29 shows the

difference between the 1,000 meter radius plume and the baseline tomogram without a low velocity zone.

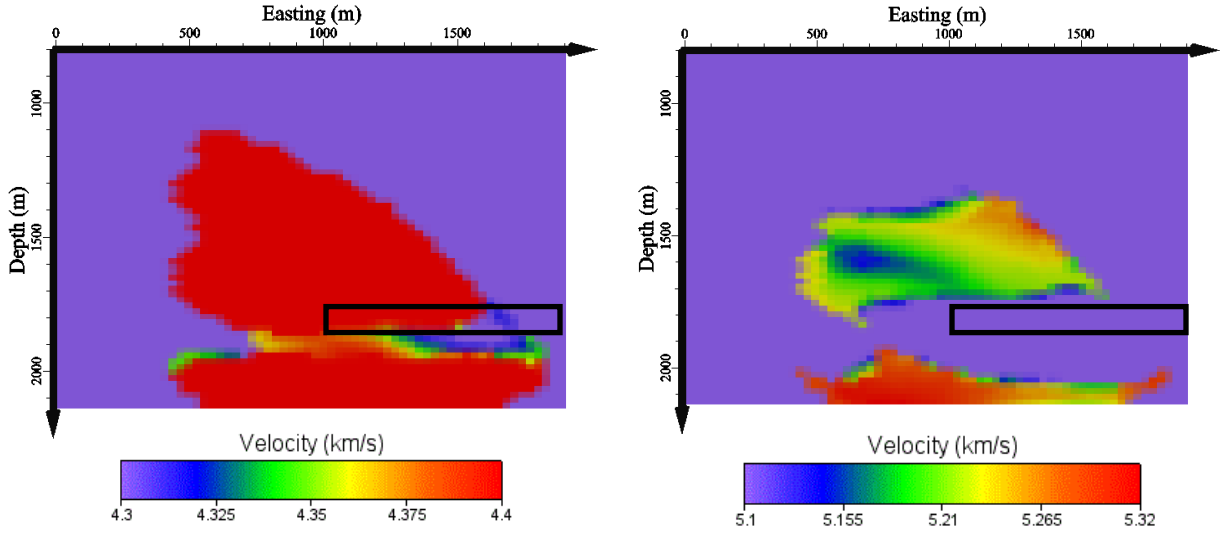

Figure 3.28: Tomograms of the 1,790 layer (left) and 1,400 layer (right) for a 1,000 meter radius plume at -400 meters northing

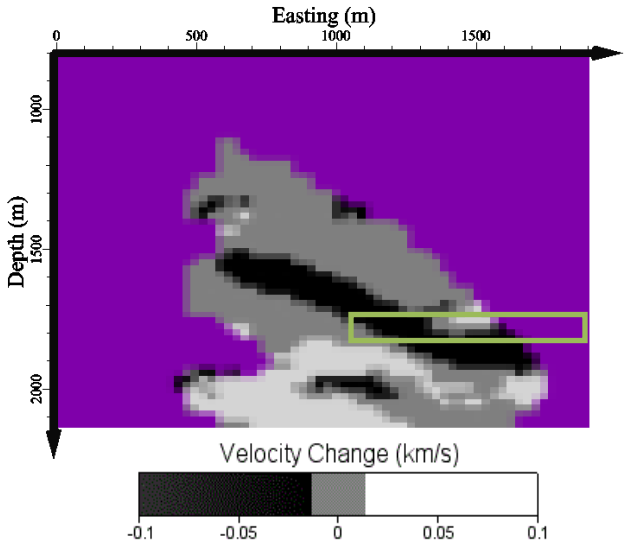

Figure 3.29: Difference between a 1,000 meter radius plume and the control at -400 meters northing

The 1,000 meter radius plume simulation shows a clear low velocity zone where the plume was placed. It extends vertically beyond its assigned depth, roughly 100 meters in both directions, demonstrating the stretching that was anticipated in any low velocity zone placed between

receivers and events with the given event-receiver arrangement. The existence of a low velocity zone in the resultant tomograms does reinforce the conclusion made for the Location C simulation that it is possible to detect a plume that exists on the border of two significantly different velocity layers.

The last low velocity zone simulates the saturation of the entire Desert Creek reservoir. It is 100 meters in depth, centered at 1,770 meters below the surface, and extends throughout the entirety of the lateral dimensions of the velocity model. Figure 3.30 shows the isolated-layer velocity structure of the target area. Figure 3.31 shows the difference between the Desert Creek saturation and the baseline tomogram without a low velocity zone.

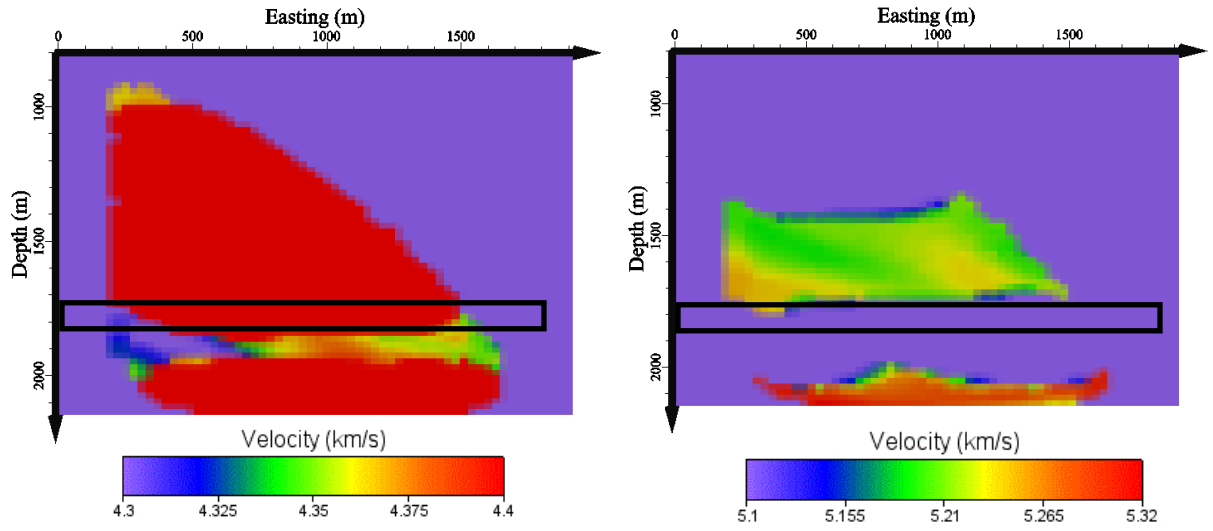

Figure 3.30: Tomograms of the 1,790 layer (left) and 1,400 layer (right) for the Desert Creek saturation test at -300 meters northing

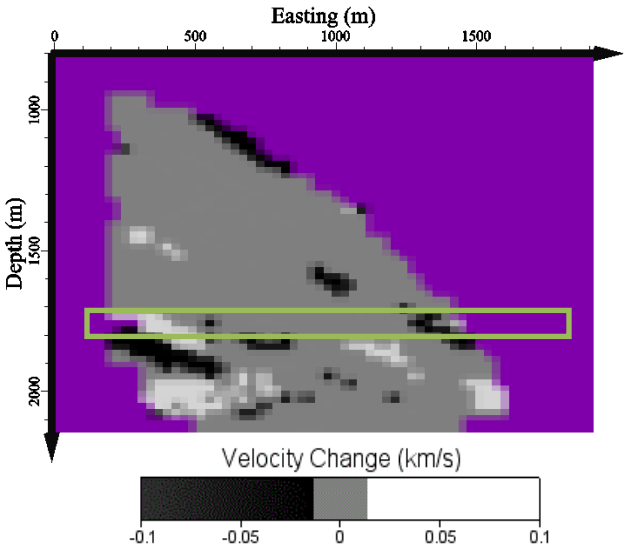

Figure 3.31: Difference between the Desert Creek saturation test and the control at -300 meters northing

A segmented low velocity zone can be seen. The similarities between the Desert Creek saturation simulation and the 1,000 meter plume radius simulation should be noted. The 1,000 meter plume radius simulation looks very similar to the Desert Creek saturation simulation through the extents of the 1,000 meter plume radius. Outside of the 1,000 meter radius, the tomogram from the Desert Creek saturation simulation shows another low velocity segment, while the 1,000 meter radius simulation does not. Both contain an area with seemingly little velocity change where a low velocity is expected. A lack of ray path coverage here due to ray bending could explain why the velocity remains relatively unchanged.

The synthetic tests help to highlight several key factors when analyzing the Aneth Unit data with the same event-receiver arrangement and background velocity model. The first of these factors is the importance of a control or baseline which can be subtracted from the other simulations to isolate velocity changes. There are low and high velocity zones in every synthetic test that are a direct result of improper velocity model adjustments, due to incorrect travel times or incorrect tomoDD adjustments. If not for a baseline model, these low and high velocity zones could be assumed to represent something geophysically significant. The second factor is the ability to detect a plume located on the boundary between low velocity and high velocity geologic formations. Location C, the 1,000 meter radius plume, and the Desert Creek saturation tests all showed low velocity zones of the proper sizes in the approximate areas of plume placement. It

should therefore not be assumed that the absence of a low velocity zone in the Aneth Unit data are a result of a low velocity zone "getting lost" among changing geologic strata. The third factor to be considered is potential stretching or shifting of low velocity zones. Location A, Location B, Location C, the 1,000 meter radius plume, and the Desert Creek saturation simulations all had some form of stretching or shifting in both the vertical and lateral dimensions. Very little confidence can be placed in the location or quantity of sequestered CO_2 based on the location and extent of a low velocity zone in this region. The fourth factor to consider is the size of the plume. Neither the 250 meter radius plume nor 500 meter radius plume were able to be detected with the given event-receiver arrangement. This is important to consider because the highest elevation of the Desert Creek reservoir lies where these two plumes were centered, and buoyantly driven flow could lead to CO_2 to accumulate in this region. A plume residing in this location would likely need to be of a diameter greater than 500 meters to be accurately detected.

3.4.4 Aneth Unit DWS Analysis

The Aneth data are presented in the same way as the synthetic data. In order to perform a time-lapse analysis, the data were divided into four time periods, which are presented sequentially. Increased ray path coverage should lead to a higher accuracy characterization of the reservoir, so only tomograms with high DWS values at the Desert Creek reservoir depth will be presented. Figure 3.32 shows the DWS values at northings of -500 meters, -300 meters, and -50 meters.

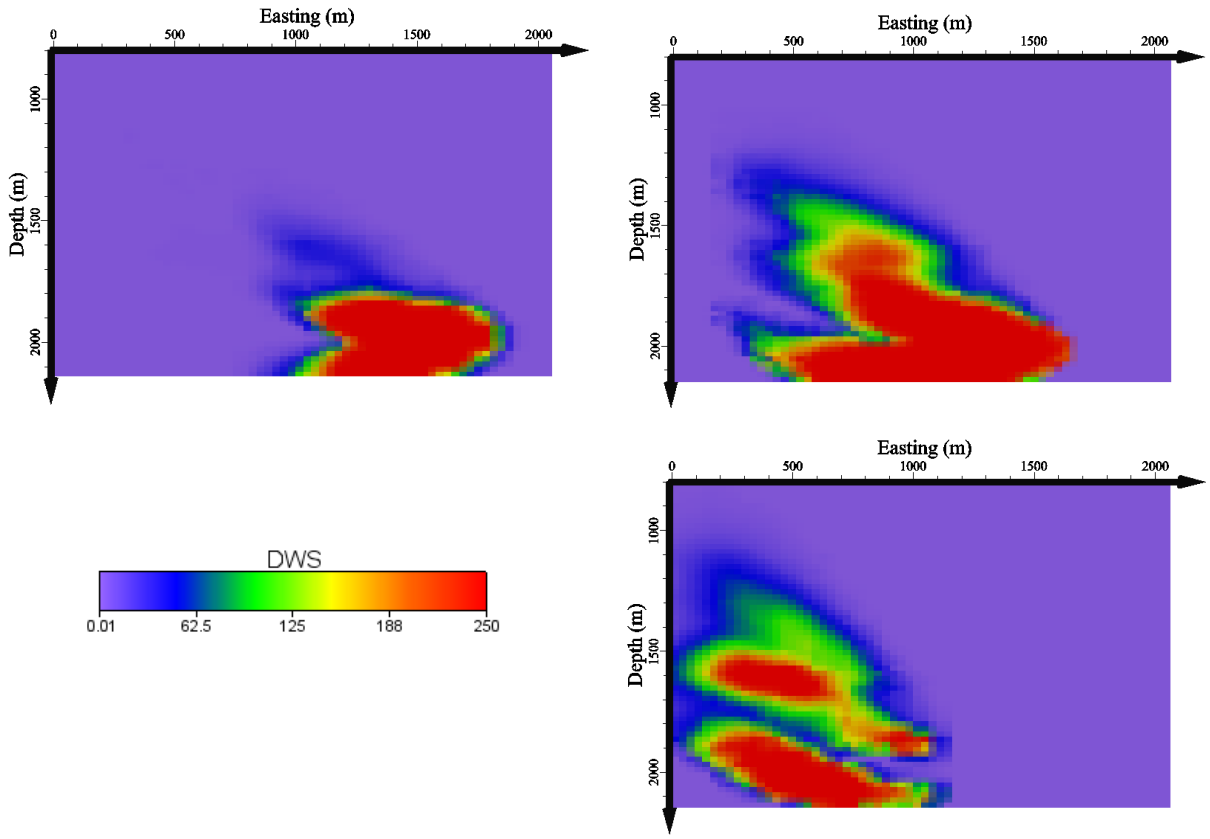

Figure 3.32: DWS levels at -500 meters northing (top left), -300 meters northing (top right), and -50 meters northing (bottom right)

These tomograms are important for several reasons. First, they represent the northing extents of good Desert Creek reservoir ray path coverage. No information should be inferred from velocity tomograms representing layers outside of these extents. Second, they provide an easting range in which the ray path coverage is acceptable. The easting range varies with the northing slice. Easting values, from which a confidence in results can roughly be assumed, range from 200 meters to 1,500 meters. All reported tomograms will be taken at the -300 meter northing slice due to its high DWS values and large range of confidence.

3.4.5 Aneth Unit Analysis by Layer

Beginning with the first time period, tomograms are presented of the lower velocity layer that underlies the Desert Creek reservoir, Figure 3.33, and the upper velocity layer that contains the Desert Creek reservoir, Figure 3.34, referred to as the 1,790 layer and 1,400 layer respectively.

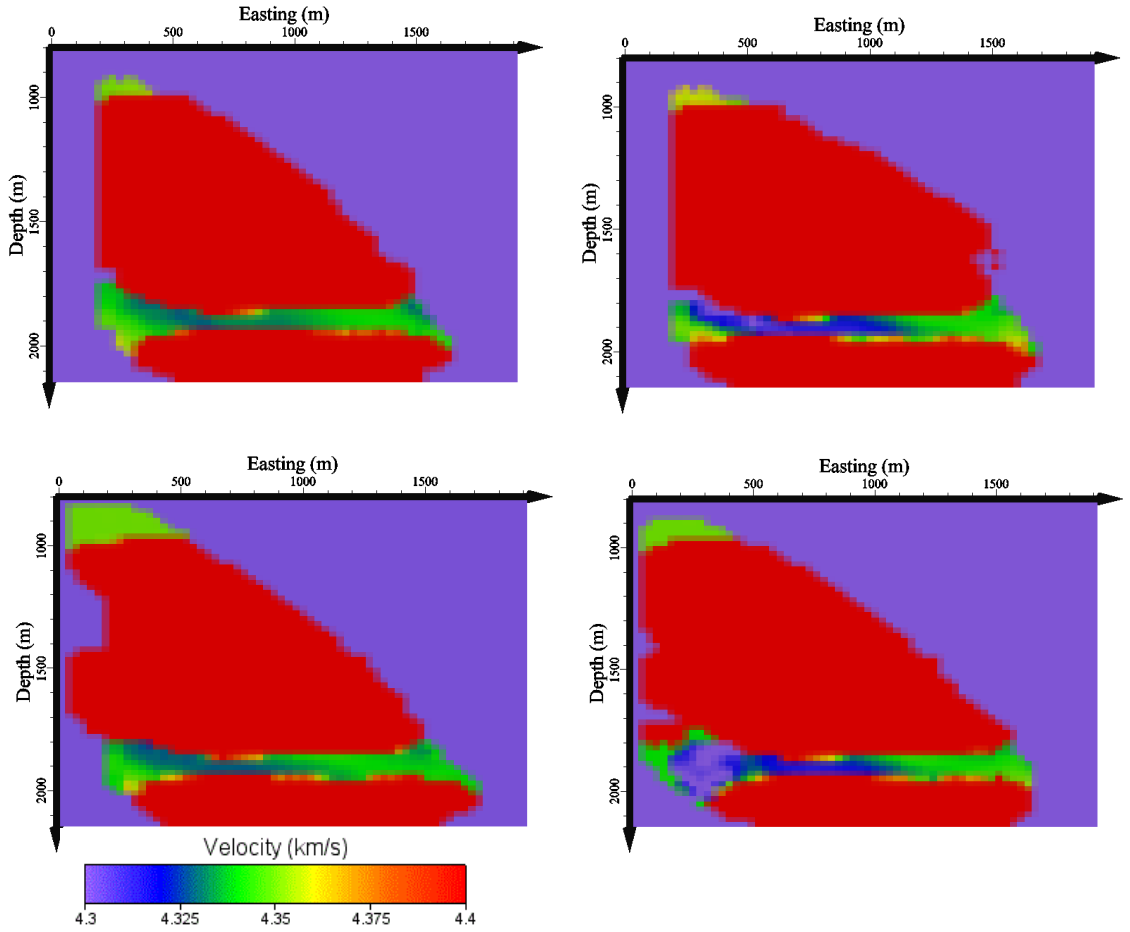

Figure 3.33: Tomograms of the 1,790 layer for Time 1 (top left), Time 2 (top right), Time 3 (bottom left), and Time 4 (bottom right) at -300 meters northing

A low velocity zone can be seen, in these tomograms, that correlates well to the DWS for this region. The easting range with confidence at this northing coordinate is roughly 400 meters to 1,200 meters, which is the general region exhibiting a low velocity for all time periods. This low velocity zone, while not located in the Desert Creek reservoir, could be the result of stretching of the plume. If this low velocity zone is a result of CO2 concentrations in the region, then there also appears to be a reduction in the levels of CO2 from Time 2 to Time 3. The other time periods follow an expected trend of decreasing velocity as the quantity of injected CO2 increases, with Time 1 showing the highest velocity, and Time 4 showing the lowest velocity.

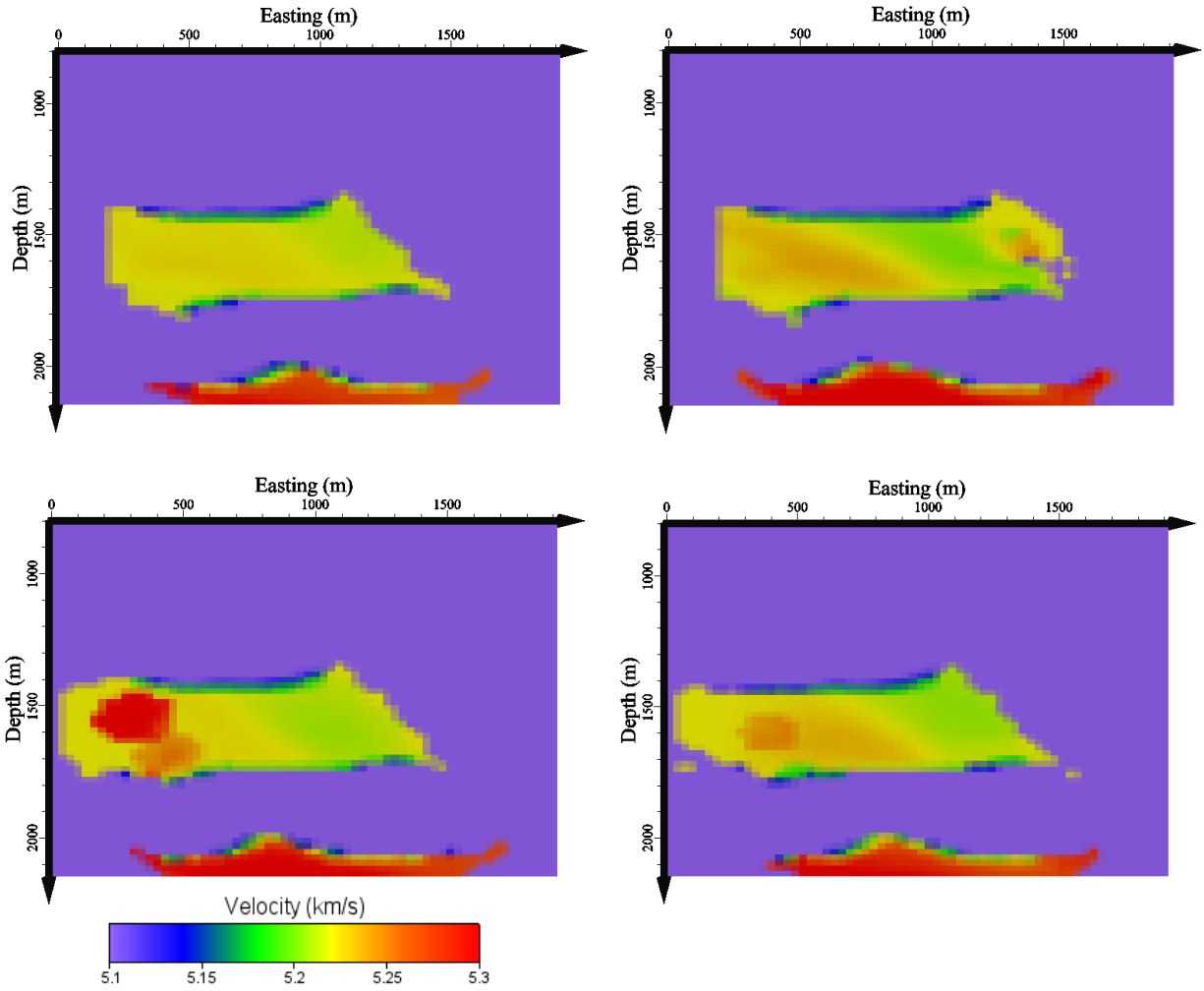

Figure 3.34: Tomograms of the 1,400 layer for Time 1 (top left), Time 2 (top right), Time 3 (bottom left), and Time 4 (bottom right) at -300 meters northing

This layer encompasses the Desert Creek reservoir, but it is improbable that any results could be inferred from the reservoir extents themselves. The reservoir borders the low velocity 1,790 layer, which resides within the interpolation distance of twice the maximum node separation. A low velocity zone can be seen, along the easternmost section of the layer, which could reflect the smearing of a low velocity zone in the Desert Creek reservoir from the events towards the stations. There is also an anomalous high velocity zone that appears in Time 3 and exists to a smaller degree in Time 4. No explanation can be given for why this high velocity zone exists, but it could be responsible for the velocity inconsistencies found in all Time 3 tests.

3.4.6 Aneth Unit Control Comparisons

To attempt to mitigate the effect of the close proximity of the Desert Creek reservoir to the 1,790 layer below it, Time 1 will be treated as a baseline, or initial velocity model. Time 1 is most likely to contain the smallest concentrations of CO2 within the regional limits, making it the ideal candidate to simulate an initial velocity model. Figure 3.35 shows the difference between Time 2 and Time 1. Figure 3.36 shows the difference between Time 3 and Time 1, and Figure 3.37 shows the difference between Time 4 and the Time 1.

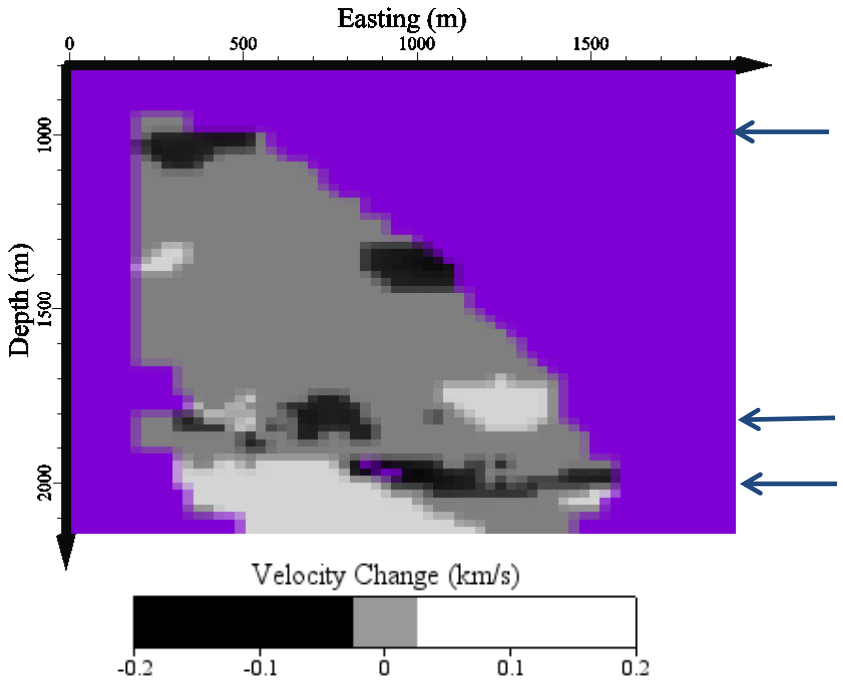

Figure 3.35: Difference between Time 2 and Time 1 at -300 meters northing

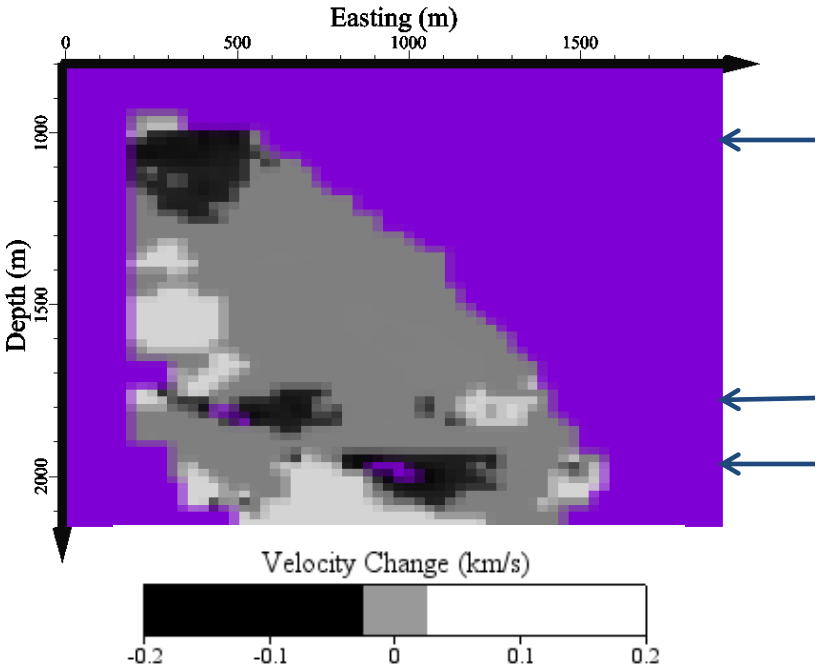

Figure 3.36: Difference between Time 3 and Time 1 at -300 meters northing

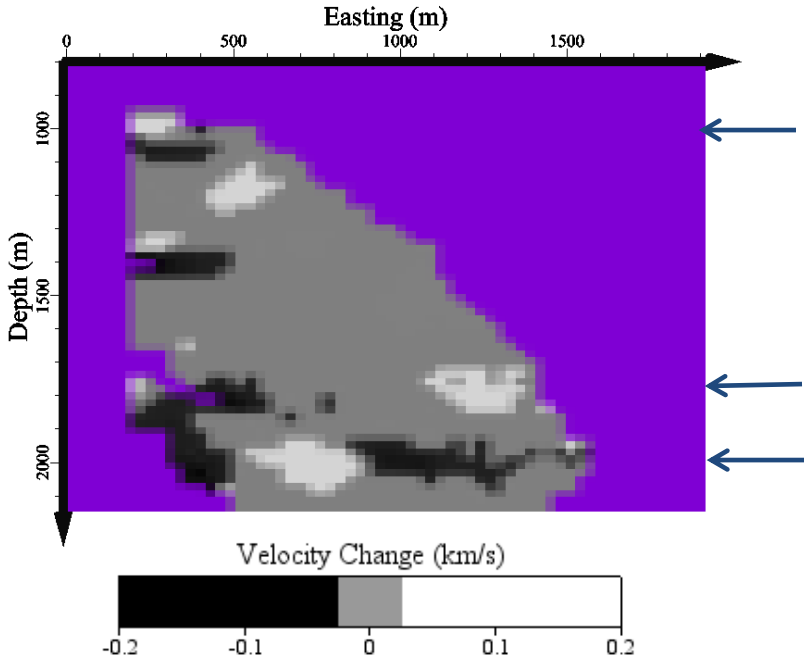

Figure 3.37: Difference between Time 4 and Time 1 at -300 meters northing

Subtracting the first time period successfully removes most of the layering of the velocity model and isolates velocity changes between the time periods. Three distinct low velocity zones appear

in all three time period analyses, indicated by the arrows. The first of these, the top low velocity zone, is not only far from any expected CO_2 accumulation but the DWS for this region is also incredibly small. This region is, therefore, dismissed as not being related to CO_2 injection. The second low velocity zone is located approximately 1,750 meters to 1,850 meters deep, and in an area of high DWS concentration. This depth not only covers a portion of the Desert Creek reservoir, but is also placed directly on the velocity layer change. It can therefore not be said for certain which regional abnormality may be responsible for the low velocity: the layer change or CO_2 accumulation. It can be observed in the synthetic tests that anomalous low or high velocity zones, likely unassociated with artificial plumes, could be created on the boundaries of velocity layers. The low velocity zone does exhibit migratory behavior that could be expected of a CO_2 plume. The center of the low velocity zone in Time 1 is approximately 700 meters easting. It moves to 600 meters easting in Time 2 and 500 meters easting in Time 3. The other low and high velocity zones do not exhibit the same migratory behavior throughout the different time periods.

The third low velocity zone is centered approximately 2,000 meters deep, near another velocity layer change. In addition to the layer change, this is also where the majority of the events are located. It is unclear what affect events will have on the velocity in the region immediately surrounding them, with only one event cluster being available for analysis. The synthetic tests show no consistent low velocity zone near the events with the exception of the Desert Creek saturation test. This low velocity zone does not have a noticeable trend between the time periods from which a quantity or migration of CO_2 could be inferred if this low velocity zone were CO_2 created. Additional tomograms for the control comparison, 1,400 layer, and 1,790 layer at different northing values can be found in Appendix C.

An alternative to using the first time period as a baseline velocity model is using the control velocity model used in the synthetic data tests as a baseline. Figure 3.38 shows the difference between the four time periods and the synthetic control test.

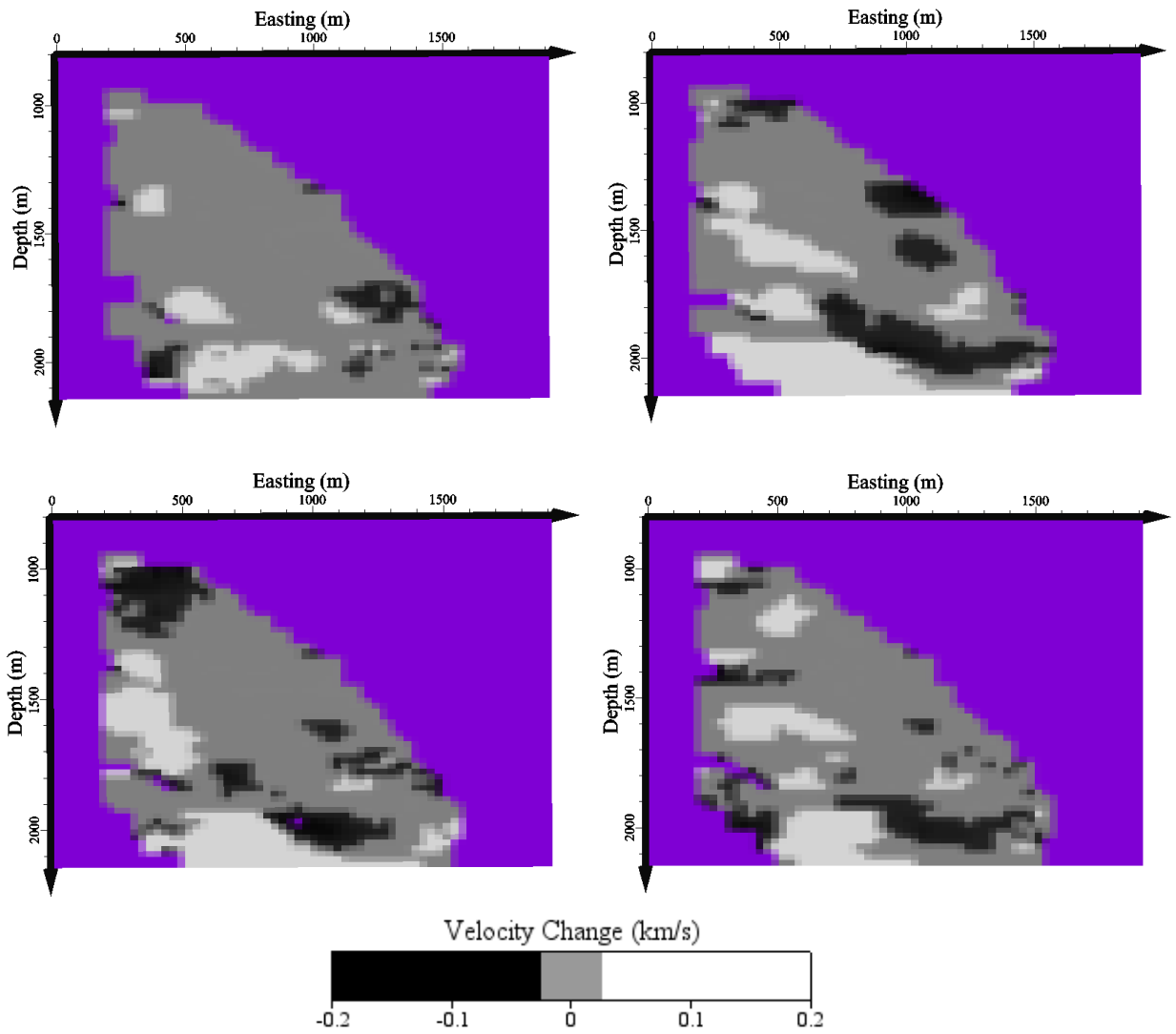

Figure 3.38: Difference between Aneth data and the synthetic control for Time 1 (top left), Time 2 (top right), Time 3 (bottom left), and Time 4 (bottom right) at -300 meters northing

Comparing the differences between the Aneth Unit data and the synthetic control yields similar results to comparing the last three time periods of the Aneth Unit data to the first. Velocity zones are placed in similar locations, but stretched further. The first time period shows the smallest variation from the synthetic control. This could be a result of either CO_2 concentrations not being high enough to greatly affect the velocity model, or smaller amount of changes due to the reduced number of ray paths. The fourth time period has the most similar number of ray paths to Time 1, but exhibits nearly as many changes as the other two time periods, so this is not likely the cause for the similarities.

No absolute conclusion can be made about which, if any, low velocity zone represents a CO_2 plume and to what extent. However, the effect that different plumes have on the velocity model can be seen through the use of synthetic data tests. The synthetic simulation that most closely resembles the Aneth Unit results is the saturation of the Desert Creek reservoir. This simulation makes the assumption that from a depth of 1,720 meters to 1,820 meters, the velocity model is 2 km/s lower than the background for every northing and easting. The result of subtracting the synthetic control from the Desert Creek saturation test at a northing of -300 meters is shown in Figure 3.39. Subtracting the Aneth Time 3 results from Time 1 results at a northing of -300 meters is shown in Figure 3.40, and subtracting the Aneth Time 3 results from the synthetic control is shown in Figure 3.41.

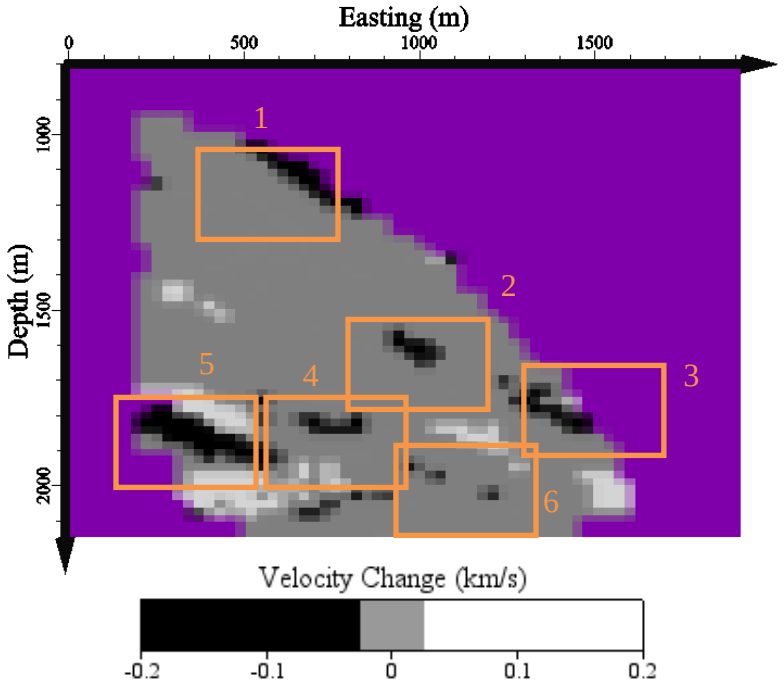

Figure 3.39: Difference between Desert Creek saturation test and the synthetic control at -300 meters northing with low velocity zones highlighted

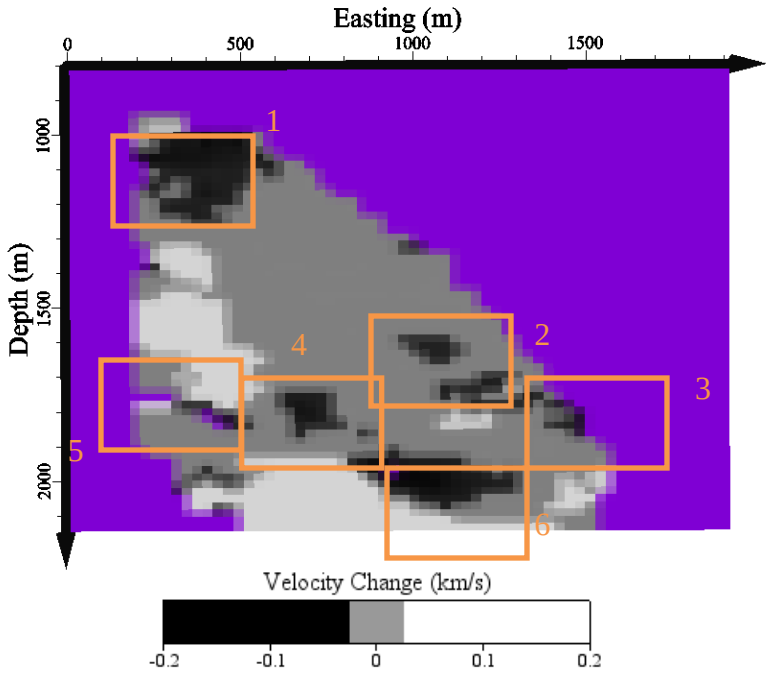

Figure 3.40: Difference between Aneth Time 3 and Aneth Time 1 at -300 meters northing with low velocity zones highlighted

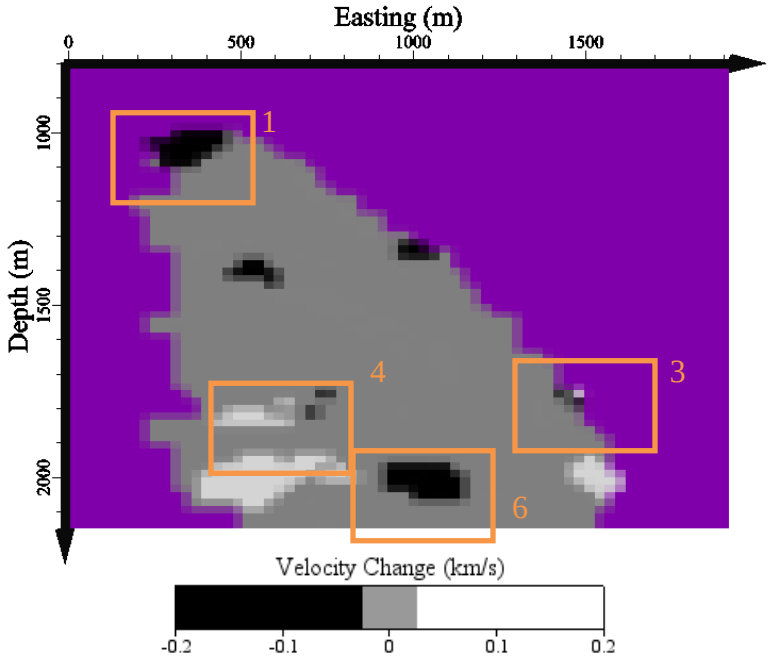

Figure 3.41: Difference between Aneth Time 3 and the synthetic control at -300 meters northing with low velocity zones highlighted

There are six boxes highlighting the low velocity areas of the Desert Creek saturation synthetic simulation. All six of these low velocity zones are represented in Figure 3.40 and four of them are present in Figure 3.41. These low velocity zones are not the same size, but appear in the same location. Other synthetic tests show low velocity zones in similar locations, but only the Desert Creek saturation test can account for all the low velocity zones. The likely explanation for this is not the concentration of CO_2 or necessarily its placement, but rather that all ray paths are traversing the plume. As a result, it would be difficult to determine the amount of CO_2 sequestered, or preciesely where it is located, because the plume itself is not being analyzed but rather the behavior of tomoDD under certain synthetic conditions. If the tomogram is very similar to the Desert Creek saturation synthetic test, it may then be concluded that the Desert Creek reservoir is experiencing some form of uniform CO_2 inundation throughout the 300 meters to 1,500 meters easting range and -600 meters northing to -50 meters northing range.

It may also be concluded that no significant leakage is occurring within the observable region. The synthetic simulation results for Location A, Location B, and Location C, all show clear, unique, low velocity zones above the Desert Creek reservoir where an artificial plume was placed, yet no clear low velocity zone is shown in any of the Aneth Unit time periods that would indicate there is an accumulation of CO_2 where there should not be.

3.4.7 Aneth Unit DWS Threshold

Lastly, a DWS threshold analysis is performed. The acceptable DWS threshold is set to the top 75% for the first test, top 50% for the second test, and top 25% for the third test. In each test, the first time period is used as a baseline and is subtracted from the remaining time periods. The results for time period 2 are given in Figure 3.42, time period 3 in Figure 3.43, and time period 4 in Figure 3.44. Time period 2 is reported at the -550 meter northing slice, while time periods 3 and 4 are reported at the -300 meter slice.

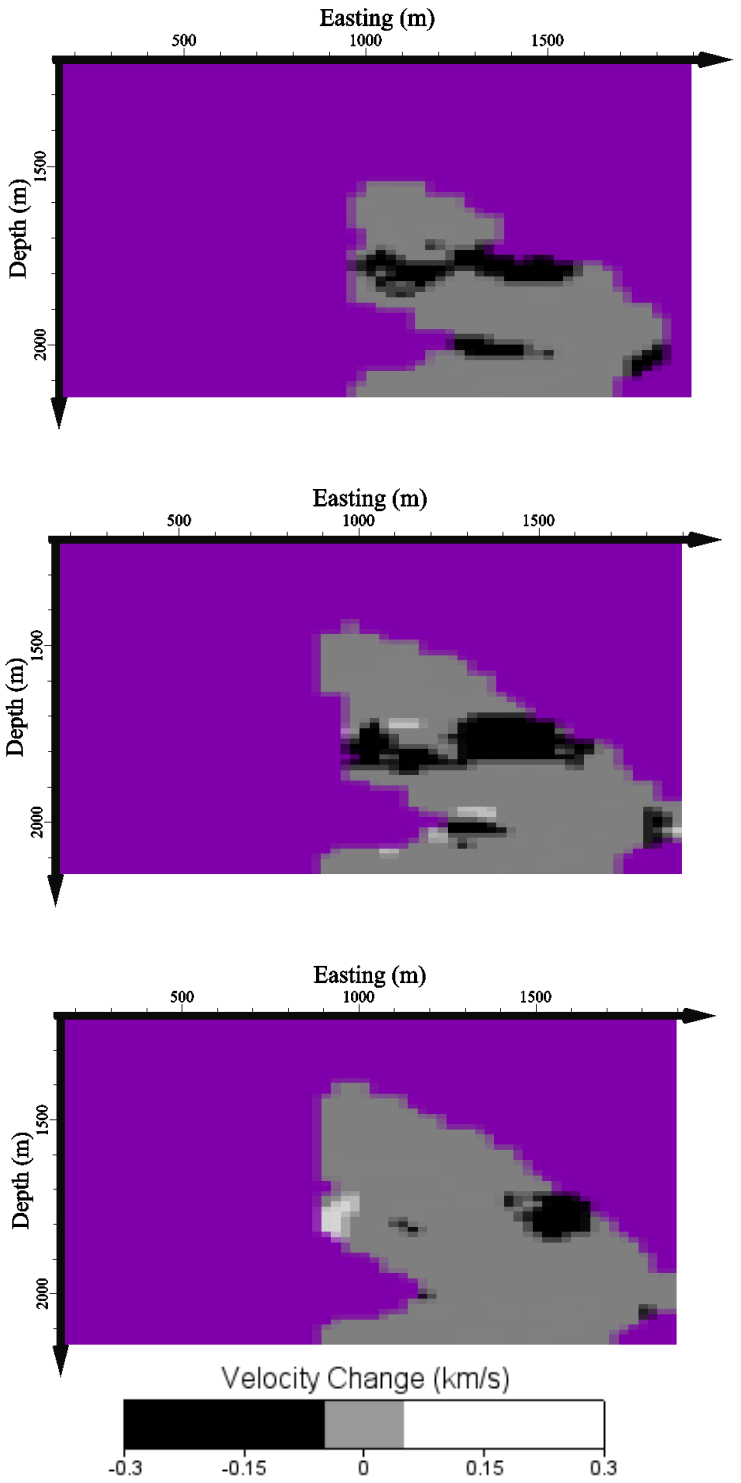

Figure 3.42: DWS thresholds of top 25% (top), top 50% (middle), and top 75% (bottom) for Aneth Time 2 at -550 meters northing

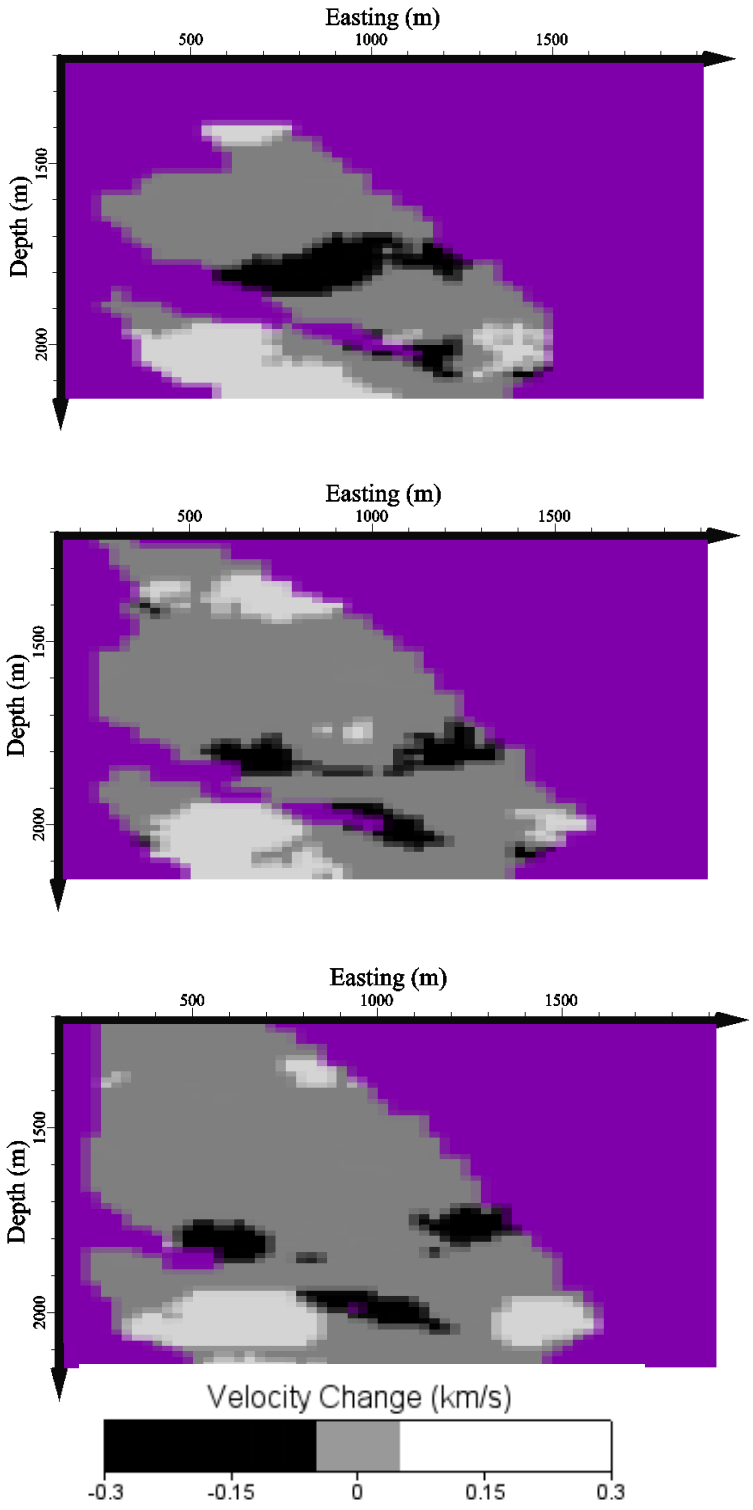

Figure 3.43: DWS thresholds of top 25% (top), top 50% (middle), and top 75% (bottom) for Aneth Time 3 at -300 meters northing

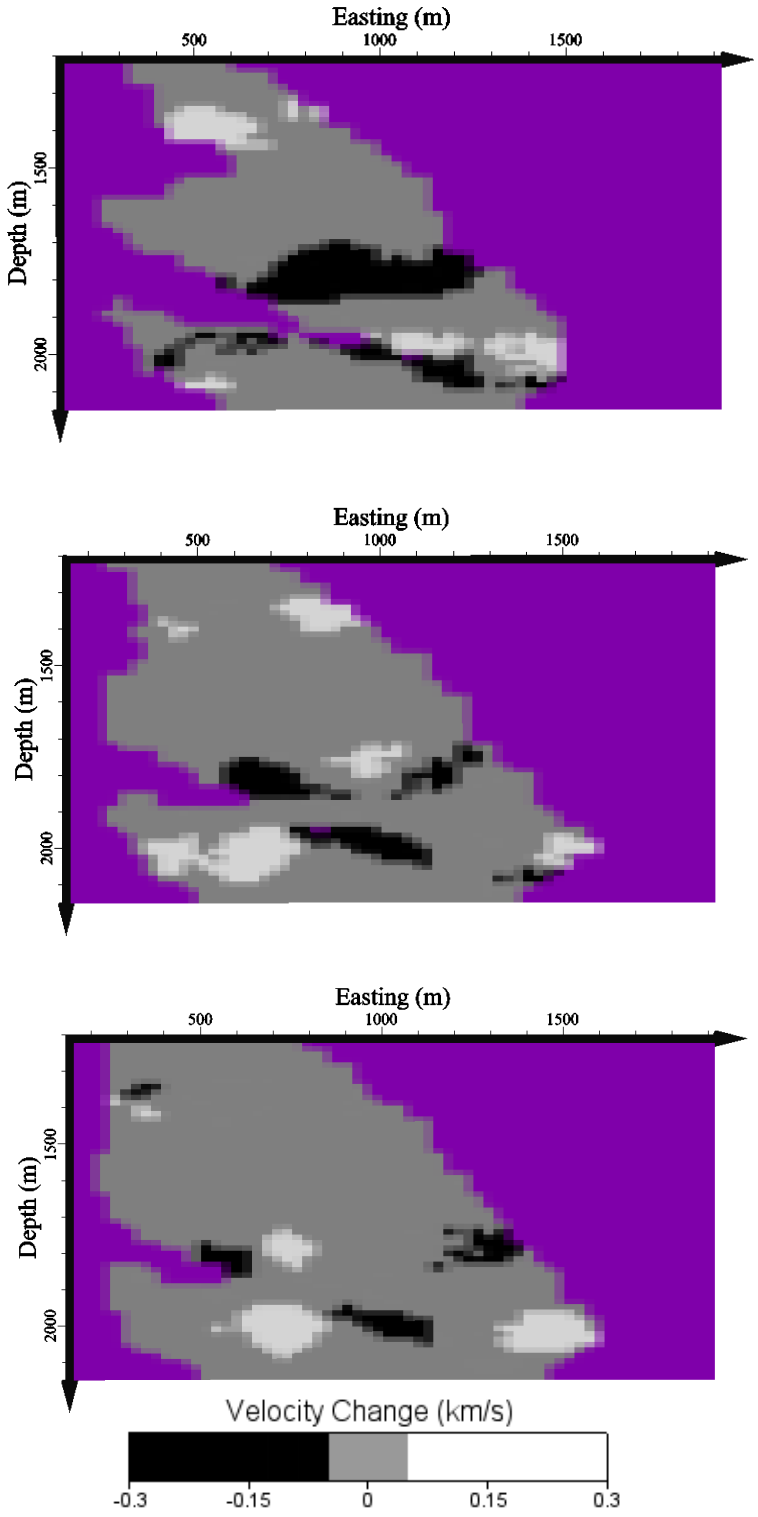

Figure 3.44: DWS thresholds of top 25% (top), top 50% (middle), and top 75% (bottom) for Aneth Time 4 at -300 meters northing

All three time periods show a very distinct trend of the target low velocity zone growing smaller as the DWS threshold is decreased. The DWS threshold test containing the data with the highest confidence shows a low velocity zone stretching from approximately 1,700 meters to 1,850 meters in depth, encompassing the entirety of the Desert Creek reservoir. It should also be noted that this low velocity zone extends across the entire easting extent, and continues for every northing value at the same depth. Average velocities for each time period and DWS threshold are reported from the 1,720 meter to 1,790 meter depth in Table 3.2. This is the assumed depth of the Desert Creek reservoir.

Table 3.2: Average velocities at different DWS thresholds and time periods

Time Period	Top 25% DWS Average Velocity (km/s)	Top 50% DWS Average Velocity (km/s)	Top 75% DWS Average Velocity (km/s)
1	5.222	5.220	5.219
2	5.222	5.219	5.218
3	5.217	5.216	5.216
4	5.226	5.223	5.221

No trend exists for average velocity per time period. Any trend in velocity change could be used to indicate plume behavior, such as migration or an increasing concentration. It is therefore concluded that any migration of CO_2 or small increases in CO_2 concentration cannot be detected with the current resolution of the CO_2 plume.

3.4.8 Discussion of Results

There are two explanations for the cause of a low velocity zone in the reported tomograms, neglecting uncertainties associated with this tomography application. The first is the presence of a CO_2 plume within the Desert Creek reservoir. The second is boundary changes throughout the velocity model, most notably the 0.88 km/s change from the 1,400 layer to the 1,789 layer in the vicinity of the Desert Creek reservoir.

Low velocity zones are only expected to be caused by CO2 concentrations and geologic anomalies not included in the initial one-dimensional velocity model. Repeated small low velocity zones are found throughout nearly every Aneth Unit test near the approximate 1,720 meter to 1,780 meter depth of the Desert Creek reservoir. Figures 3.35 through 3.37 show a migration of one of these low velocity zones, which is potential behavior of a CO2 plume. The direction of this plume's migration, however, is towards a lower elevation, which is unlikely given the buoyancy of CO2. The arrangement of small low velocity zones in the Aneth Unit data resemble the arrangement of small low velocity zones in the synthetic Desert Creek saturation simulation, shown in Figures 3.39 through 3.41. Only the Desert Creek saturation simulation contains low velocity zones in the same locations as the Aneth Unit data while remaining the same approximate size. Given the exaggerated drop in velocity assigned to the Desert Creek saturation simulation, these similar results are likely due to ray paths being forced to travel through the plume rather than an indication of the amount of CO_2 contained in this region. More evidence to suggest the existence of a CO_2 plume is the appearance of a large, distinct low velocity zone surrounding the Desert Creek reservoir when confidence limits are applied to the data. Figures 3.42 through 3.44 show an increasingly clear low velocity zone 1,700 meter to 1,850 meter depth. Removing voxels with a low DWS values creates an interpolation region showing a consistent low velocity that continues through the northing extents of the observable region. This low velocity zone does not show the smearing along the ray path direction exhibited in the synthetic tests varying plume location, but neither does the Desert Creek saturation simulation or the 1,000 meter radius plume simulation, suggesting that the smearing was related to plume positioning precisely between the events and receivers.

The positioning of both the Desert Creek reservoir and the event cluster near a velocity layer boundary in the velocity model increases the difficulty with which anomalous stretching of velocity layers and actual low velocity zones can be differentiated. Velocity layer boundaries exist at depths of 1,050 meters, 1,400 meters, 1,790 meters, and 2,050 meters. Low or high velocity anomalies are present at each of these depths in every test of both Aneth Unit data and synthetic data. However, low velocity anomalies at the 1,790 meter depth velocity boundary are small in all tests that do not include a plume in the immediate vicinity. While small velocity perturbations may be expected as a result of velocity layer boundaries, the low velocity region

detected in the high DWS Aneth Unit data tests are too large to be the result of velocity layer boundaries alone.

Determining the degree to which MVA can be performed on this reservoir using double-difference seismic tomography is a major objective of this project. The three components of MVA are defined as follows:

- Monitoring - monitor both the location and impact of sequestered CO_2.
- Verifying - verify movement of CO_2 and ensure that sequestered CO_2 is not permeating the sealing mechanism, or migrating to an unsealed area.
- Accounting - account for the amount of injected CO_2, by comparing it to the amount of CO_2 estimated to be in place, through the chosen monitoring method.

The results obtained show potential for monitoring applications. The location of a plume can be determined in two ways. The first is through establishing confidence thresholds for voxels that will exclude data points with low ray path coverage. The second is by comparing supposed plume locations with actual data to find results that match in velocity zone placement.

Verification of CO_2 in the Aneth Unit is a substantial challenge given the event-receiver arrangement. None of the tomograms show a low velocity zone confined to the Desert Creek reservoir. Nearly all of the tomograms show significant stretching of low velocity zones up to hundreds of meters in either the positive or negative depth direction. The exaggerated size of these low velocity zones makes assessing leakage and migration very difficult without significant changes to the plume location.

Accounting for the amount of injected CO_2 requires both accurate imaging of the extents of a CO_2 plume and the concentrations therein. The plume located in the Desert Creek reservoir suffers from two flaws that prevent accounting for the amount of CO_2 it contains. The first flaw is the same exaggerated size of the plume that prevented accurate verification. The effect of a smeared plume size can be mitigated to an extent because the same concentration of CO_2 is likely spread over a larger area. A reduced concentration over a larger area may yield the same amount of CO_2 as a normal concentration over a smaller area. The second flaw is the lateral

extents of the detected low velocity zone. The DWS coverage for the Aneth Unit is very limited, and the detected low velocity zone extends beyond the limits of the observable region. With no bounds to confine the plume, no estimation of the quantity of CO_2 in place can be made. A receiver arrangement that provides not only more comprehensive ray path coverage of the Desert Creek reservoir but also encompasses a larger portion of the Aneth Unit is needed to prevent stretching of the CO_2 plume or incomplete characterization of the lateral plume boundaries. For proper accounting of CO_2, it is also necessary to know if any CO_2 has been produced to properly account for the volume of injected CO_2.

Chapter 3 References

[19] T.-w. Lo and P. Inderwiesen, *Fundamentals of Seismic Tomography* vol. 6, 1994.

[23] K. Luxbacher, *et al.*, "Time-Lapse Tomography of a Longwall Panel: A Comparison of Location Schemes," presented at the 26th International Conference on Ground Control in Mining, Morgantown, West Virginia, 2007.

[26] K. Luxbacher, *et al.*, "Three-dimensional time-lapse velocity tomography of an underground longwall panel," *International Journal of Rock Mechanics and MIning Sciences,* vol. 45, pp. 478-485, 2008.

[30] S. Persoglia, *et al.*, "4-D Seismics, Gas-Hydrate Detection and Overpressure Prediction as a Combined Methodology for Application to CO2 Sequestration," 2006.

[48] T. C. Chidsey, *et al.*, "Why Modelers Need to Look at the Rocks! Examples from Greater Aneth Field, Paradox Basin, Utah," 2007.

[49] H. Zhang and C. H. Thurber, "Double-Difference Tomography: The Method and Its Application to the Hayward Fault, California," *Bulletin of the Seismological Society of America,* vol. 93, pp. 1875-1889, 2003.

[50] H. Zhang and C. Thurber, "User's manual for tomoDD1.1 (double-difference tomography) for determining event locations and velocity structure from local earthquakes and explosions," Department of Geology and Geophysics, University of Wisconsin-Madison 2003.

[51] *Southwest Partnership CO_2 Sequestration*. Available: http://southwestcarbonpartnership.org/AboutSWP.html

[52] S. Carney, "Carbon Dioxide Sequestration Demonstration Project Underway in Utah!," Utah Geological Survey 2009.

[53] T. C. Chidsey, *et al.*, "Aneth Oil Field, Southeastern Utah: Demonstration Site for Geologic Sequestration of Carbon Dioxide," S. R. P. o. C. Sequestration, Ed., ed, 2006.

[54] "Factsheet for Partnership Field Validation Test," in *Regional Carbon Sequestration Partnerships Annual Review Meeting*, Pittsburgh, PA, 2009.

[55] "Statement of Basis - Aneth Unit Phase III: Class IIR Area Permit," U. S. E. P. Agency, Ed., ed. San Juan County, Utah, 2008.

[56] P. E. Babcock, "Aneth (Aneth Unit)," The Superior Oil Company 1978.

[57] A. Cheng, *et al.*, "Time-lapse VSP data processing for monitoring CO_2 injection," *The leading Edge,* 2010.

[58] F. Waldhauser, "A Program to Compute Double-Difference Hypocenter Locations," U.S. Geological Survey 2001.

[59] J. Rutledge, "Geologic Demonstration at the Aneth Oil Field, Paradox Basin, Utah," New Mexico Institute of Mining and Technology 2010.

Chapter 4: Summary of Results and Conclusion

Double-difference tomography was performed on a carbon sequestration project in the Aneth Unit of the Aneth Oil Field in southeast Utah. Location data for 1,211 passively induced seismic events was provided as well as travel times between the seismic events and a vertical borehole arrangement of 22 geophones. The provided data were split into four sequential time periods for a time-lapse tomographic analysis of subsurface conditions. Simulations using synthetic data were also conducted to understand the behavior and sensitivity of tomoDD as well as to compare expected results with actual results.

Locating a CO_2 plume in the Aneth Unit is made difficult due to a narrow ray path distribution, generated by a borehole array of geophones and single cluster of seismic events. A low velocity zone was detected, however, in the Desert Creek reservoir among tomograms excluding low DWS values. This low velocity zone could be the result of an increasing CO_2 concentration within the Desert Creek reservoir. It is distributed across the extents of the observable region, which would be expected in a region experiencing injection from multiple wells. This low velocity zone begins to deteriorate with decreased DWS, highlighting the importance of ray path coverage.

Also reinforcing the existence of a plume within the Desert Creek reservoir is the comparison of a synthetic test simulating the complete saturation of the Desert Creek reservoir with the results obtained from Aneth Unit data. The synthetic simulation shows low velocity zones in the same place and of the approximate size as in the Aneth Unit data. These low velocity zones themselves may not represent CO_2 plumes, but the behavior associated with a Desert Creek saturation synthetic test being very similar to the Aneth Unit results reinforces the conclusion that there may have been a uniformly distributed CO_2 inundation across the reservoir detected by double-difference tomography.

With the event and receiver arrangements, double-difference seismic tomography is a poor choice as a method of MVA for the Aneth Unit. The resolution of CO_2 detected is too low to

make informed verification or accounting decisions. Monitoring is possible to a limited extent, but precise and accurate locations for a CO_2 plume cannot be determined. A more comprehensive event-receiver arrangement is required for accurate tomographic imaging of the Desert Creek reservoir.

4.1 Possible Sources of Error

The possible sources of error within the Aneth Unit data include the event-receiver arrangement, the methods by which the event locations and travel times were determined, and a one-dimensional initial velocity model. The event-receiver arrangement in the Aneth Unit results in an undesirable ray path distribution in the Desert Creek reservoir. It is unknown the extent to which the event-receiver arrangement affects the results, but the accuracy of tomography increases with ray paths traversing the body-of-interest from as many angles as possible. The events recorded at the Aneth Unit formed two relatively narrow clusters, forcing all ray paths along two narrow paths. With the northern cluster having been removed in data pre-processing due to an insufficient number of events, this reduces the ray path coverage crossing the Desert Creek reservoir even further, as shown in Figure 4.1 and Figure 4.2.

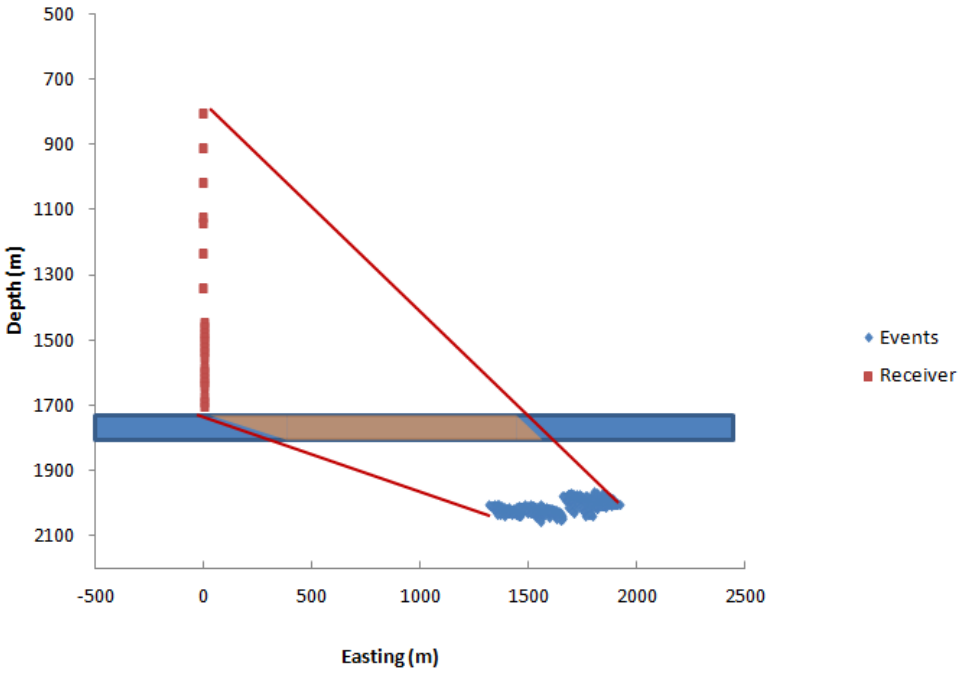

Figure 4.1: Desert Creek reservoir vertical ray path coverage

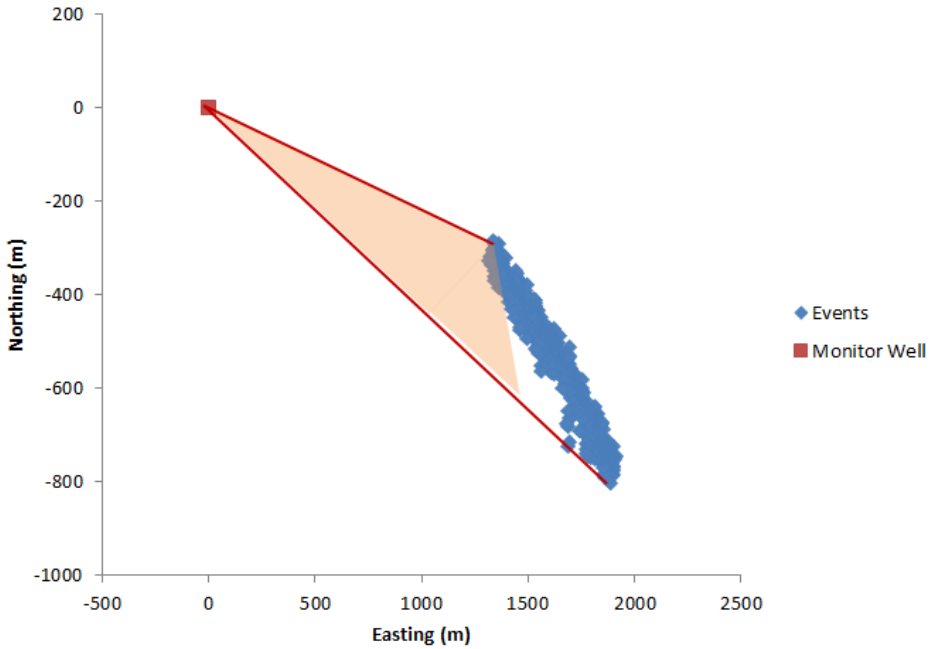

Figure 4.2: Desert Creek reservoir lateral ray path coverage

It is difficult to obtain accurate, passive, seismic event locations. Double-difference tomography should assist in precise relocation of events, but if arrival times were determined by inaccurately located events, then the relocation may not improve event locations to within an acceptable level. The accuracy of event location is a function of the receiver arrangement. The single column of events located 200 meters to 1,100 meters above the events may provide a better estimation of depth than a varied surface array, but likely results in a poor characterization of the events' lateral positions.

The accuracy of the initial velocity model affects the accuracy of the final velocity model. It is better to use the one-dimensional velocity model provided, than to assume a constant background velocity, but this velocity model could be further improved by the use of an accurate two or three-dimensional velocity model. In the current velocity model there is assumed to be no lateral variation in geology. It is unknown the extent to which lateral heterogeneities in the geologic structure would affect the results of tomography.

A possible source of error in the synthetic data is the means by which travel times were calculated. The travel time calculator is node-based, meaning each event and receiver will have to draw a travel path to the nearest node before calculating an event-receiver travel path. This additional travel distance is greatest for events furthest from a node. Creating an event-node or station-node travel path artificially increases the total travel time. For example, two events equidistant from a receiver in a constant velocity model should have identical travel times; however, if one event is closer to a node than another, the closer event will have a shorter travel time. This has the potential to be especially problematic when applying double-difference tomography, as the assumption will be made that the difference in travel times of two closely spaced events is due to a velocity anomaly in the immediate event region rather than an extended node-event travel path. The effect this has on travel paths is a function of the number of nodes used, which must be kept small due to processing restrictions.

4.2 Future Work

Several additional steps can be taken to improve the accuracy of tomographic imaging of carbon sequestration in the Aneth Unit. The first step is the improvement of the event-receiver arrangement. While drilling more boreholes for increased ray path coverage would be expensive, the addition of a surface geophone array, when used in conjunction with the current borehole array could provide significantly better ray path coverage.

Another step to improving the results that can be taken is to improve the synthetic travel-time calculation method. The current method of calculating travel times is either inaccurate or resource intensive. A progressive travel-time calculator that does not need to individually check every segment combination in a node-based grid could provide better results faster.

A third step is imposing a constraint on the velocity model that would prevent changes from being made to certain regions. Within the Aneth Unit, the only major change occurring during the experiment is within the Desert Creek reservoir. If the velocity model were not allowed to change from one time period to the next except within the immediate vicinity of the Desert Creek reservoir, all changes reflected in travel times would be appropriately applied to this region. While verification of CO_2 leakage could be affected by this approach, if CO_2 concentrations are detected in a region immediately above the Desert Creek reservoir, the velocity model could be later extended to account for the extent of CO_2 leakage.

Appendix A – TomoDD and ph2dt inputs

TomoDD and ph2dt require various files for proper functionality. Among these are the tomoDD.inp file, which defines necessary parameters for tomoDD operation, the station locations, the event locations, and travel time data. The tomoDD.inp file for Time 2, receiver locations, and sample data containing both event locations and travel time data for Time 2 are provided in this Appendix.

TomoDD.inp

```
*catalog P diff times:
dt.ct
*
* event file:
events.dat
*
* station file:
station.dat
*
*--- output file selection
* original locations:
Rway_mar10n.loc
* relocations:
Rway_mar10n.reloc
* station information:
Rway_mar10n_syn.sta
* residual information:
Rway_mar10n_syn.res
* source paramater information:
*hypo3VDD.src

*Output velocity
Rway_mar10n.vel
*absolute data
tt.dat
*--- data type selection:
* IDAT:  0 = synthetics; 1= cross corr; 2= catalog; 3= cross & cat
* IPHA: 1= P; 2= S; 3= P&S
* DIST:max dist [km] between cluster centroid and station
* IDAT   IPHA   DIST
   2     1      7000
*
*--- event clustering:
* OBSCC:    min # of obs/pair for crosstime data (0= no clustering)
```

```
* OBSCT:    min # of obs/pair for network data (0= no clustering)
* OBSCC  OBSCT  CC_format
  0     0      2
*
*--- solution control:
* ISTART:  1 = from single source; 2 = from network sources
* ISOLV:   1 = SVD, 2=lsqr
* NSET:      number of sets of iteration with specifications following
*  ISTART  ISOLV  NSET weight1 weight weight3 air_depth
   2       2    16    100       100      100       0
* i3D delt1 ndip iskip scale1 scale2 iusep iuses iuseq
  2   1   9    1    1.0   2.0    1    1    0
* invdel ifixl xfac   tlim     nitpb(1) nitpb(2) stepl
   1     0    1.3   0.002    10      10       1.0
* lat_Orig lon_Orig Z_Orig iorig rota
 0.00001  0.00001  0  1  0
*
*--- data weighting and re-weighting:
* NITER:                    last iteration to used the following weights
* WTCCP, WTCCS:                     weight cross P, S
* WTCTP, WTCTS:                     weight catalog P, S
* WRCC, WRCT:                       residual threshold in sec for cross, catalog data
* WDCC, WDCT:                       max dist [km] between cross, catalog linked pairs
* DAMP:                     damping (for lsqr only)
*       ---  CROSS DATA ----- ----CATALOG DATA ----
* NITER WTCCP WTCCS WRCC WDCC WTCTP WTCTS WRCT WDCT WTCD DAMP JOINT THRES
 3     0.01  0.01 -9    -9   1.0   0    -9   -9   -9   80   1     2
 3     0.01  0.01 -9    -9   1.0   0    -9   -9   -9   80   0     2
 3     0.01  0.01 -9    -9   1.0   0    -9   10   10   80   1     2
 3     0.01  0.01 -9    -9   1.0   0    -9   10   10   80   0     2
 3     0.01  0.01 -9    -9   1.0   0     6   10   10   80   1     2
 3     0.01  0.01 -9    -9   1.0   0     6   10   10   80   0     2
 3     0.01  0.01 -9    -9   1.0   0     6   10   10   80   1     2
 3     0.01  0.01 -9    -9   1.0   0     6   10   10   80   0     2
 3      1    0.5  -9    -9   1.0   0     6   10   10   80   1     2
 3      1    0.5  -9    -9   1.0   0     6    5   10   80   0     2
 3      1    0.5  -9    -9   1.0   0     6    5    5   80   1     2
 3      1    0.5  -9    -9   1.0   0     6    5    5   80   0     2
 3      1    0.5   8    -9   1.0   0     6    5    5   80   1     2
 3      1    0.5   8    -9   1.0   0     6    2    2   80   0     2
 3      1    0.5   8    -9   1.0   0     6    2    2   80   1     2
 3      1    0.5   8    -9   1.0   0     6    2    2   80   0     2
*
*--- event selection:
* CID:          cluster to be relocated (0 = all)
* ID:           cuspids of event to be relocated (8 per line)
* CID
   0
* ID
```

Table A.1: Receiver locations

Station ID #	Northing (m)	Easting (m)	Depth (m)
1	-9.11	-1.17	1704.42
2	-9.23	-1.34	1689.19
3	-9.34	-1.51	1673.95
5	-9.57	-1.85	1643.48
6	-9.69	-2.02	1628.24
7	-9.80	-2.19	1613.00
8	-9.92	-2.36	1597.77
9	-10.03	-2.52	1582.53
11	-10.27	-2.77	1552.05
12	-10.38	-2.91	1536.81
13	-10.50	-3.05	1521.57
14	-10.61	-3.19	1506.34
15	-10.73	-3.33	1491.10
16	-10.82	-3.48	1475.86
17	-10.92	-3.63	1460.62
18	-11.03	-3.79	1445.38
25	-11.89	-5.06	1338.71
32	-13.20	-6.31	1232.05
38	-14.41	-7.32	1140.62
39	-14.57	-7.46	1125.38
46	-15.30	-8.17	1018.71
53	-15.34	-8.92	912.03
60	-15.07	-9.59	805.35

Table A.2: Sample travel time data for Aneth Unit Time 2

ID #	Station ID	Station X (m)	Station Y (m)	Station Z (m depth)	Event X (m)	Event Y (m)	Event Z (m depth)	Travel Time (ms)	Distance (m)
170	2	-1.34	-9.23	1689.19	1608.03	-525.33	2025.72	368.29	1723.28
170	3	-1.51	-9.34	1673.95	1608.03	-525.33	2025.72	368.35	1726.44
170	5	-1.85	-9.57	1643.48	1608.03	-525.33	2025.72	367.82	1733.15
170	6	-2.02	-9.69	1628.24	1608.03	-525.33	2025.72	366.33	1736.70
170	7	-2.19	-9.80	1613.00	1608.03	-525.33	2025.72	364.97	1740.37
170	8	-2.36	-9.92	1597.77	1608.03	-525.33	2025.72	365.03	1744.17
170	9	-2.52	-10.03	1582.53	1608.03	-525.33	2025.72	364.97	1748.08
170	11	-2.77	-10.27	1552.05	1608.03	-525.33	2025.72	362.84	1756.23
170	12	-2.91	-10.38	1536.81	1608.03	-525.33	2025.72	362.84	1760.49
170	13	-3.05	-10.50	1521.57	1608.03	-525.33	2025.72	362.52	1764.87
170	14	-3.19	-10.61	1506.34	1608.03	-525.33	2025.72	362.48	1769.38
170	15	-3.33	-10.73	1491.10	1608.03	-525.33	2025.72	363.48	1774.01
170	16	-3.48	-10.82	1475.86	1608.03	-525.33	2025.72	365.56	1778.77
170	17	-3.63	-10.92	1460.62	1608.03	-525.33	2025.72	366.22	1783.64
170	18	-3.79	-11.03	1445.38	1608.03	-525.33	2025.72	366.16	1788.65
170	25	-5.06	-11.89	1338.71	1608.03	-525.33	2025.72	368.85	1826.92
170	32	-6.31	-13.20	1232.05	1608.03	-525.33	2025.72	380.93	1870.36
170	38	-7.32	-14.41	1140.62	1608.03	-525.33	2025.72	389.63	1911.49
170	46	-8.17	-15.30	1018.71	1608.03	-525.33	2025.72	405.49	1971.37
170	53	-8.92	-15.34	912.03	1608.03	-525.33	2025.72	421.55	2028.53
170	60	-9.59	-15.07	805.35	1608.03	-525.33	2025.72	441.2	2089.58
171	1	-1.17	-9.11	1704.42	1374.18	-326.58	2017.90	317.73	1445.91
171	2	-1.34	-9.23	1689.19	1374.18	-326.58	2017.90	317.38	1449.42
171	3	-1.51	-9.34	1673.95	1374.18	-326.58	2017.90	317.26	1453.09
171	5	-1.85	-9.57	1643.48	1374.18	-326.58	2017.90	316.84	1460.87
171	6	-2.02	-9.69	1628.24	1374.18	-326.58	2017.90	314.06	1464.98
171	7	-2.19	-9.80	1613.00	1374.18	-326.58	2017.90	314.06	1469.24
171	8	-2.36	-9.92	1597.77	1374.18	-326.58	2017.90	313.88	1473.65
171	9	-2.52	-10.03	1582.53	1374.18	-326.58	2017.90	312.87	1478.19
171	11	-2.77	-10.27	1552.05	1374.18	-326.58	2017.90	311.18	1487.64
171	12	-2.91	-10.38	1536.81	1374.18	-326.58	2017.90	311.27	1492.58
171	13	-3.05	-10.50	1521.57	1374.18	-326.58	2017.90	311.37	1497.67
171	14	-3.19	-10.61	1506.34	1374.18	-326.58	2017.90	311.92	1502.89
171	15	-3.33	-10.73	1491.10	1374.18	-326.58	2017.90	312.59	1508.25
171	16	-3.48	-10.82	1475.86	1374.18	-326.58	2017.90	314.59	1513.75
171	17	-3.63	-10.92	1460.62	1374.18	-326.58	2017.90	314.88	1519.39
171	18	-3.79	-11.03	1445.38	1374.18	-326.58	2017.90	315.24	1525.18
171	25	-5.06	-11.89	1338.71	1374.18	-326.58	2017.90	318.55	1569.28
171	32	-6.31	-13.20	1232.05	1374.18	-326.58	2017.90	330.87	1619.11
171	38	-7.32	-14.41	1140.62	1374.18	-326.58	2017.90	340.57	1666.02

171	46	-8.17	-15.30	1018.71	1374.18	-326.58	2017.90	356.94	1733.83
171	53	-8.92	-15.34	912.03	1374.18	-326.58	2017.90	373.31	1798.00
171	60	-9.59	-15.07	805.35	1374.18	-326.58	2017.90	394.32	1866.05
172	1	-1.17	-9.11	1704.42	1529.08	-433.48	2028.21	348.92	1620.68
172	2	-1.34	-9.23	1689.19	1529.08	-433.48	2028.21	349.4	1623.92
172	3	-1.51	-9.34	1673.95	1529.08	-433.48	2028.21	349.4	1627.30
172	5	-1.85	-9.57	1643.48	1529.08	-433.48	2028.21	348.8	1634.46
172	6	-2.02	-9.69	1628.24	1529.08	-433.48	2028.21	346.97	1638.24
172	7	-2.19	-9.80	1613.00	1529.08	-433.48	2028.21	346.37	1642.16
172	8	-2.36	-9.92	1597.77	1529.08	-433.48	2028.21	346.3	1646.20
172	9	-2.52	-10.03	1582.53	1529.08	-433.48	2028.21	346.46	1650.37
172	11	-2.77	-10.27	1552.05	1529.08	-433.48	2028.21	343.8	1659.04
172	12	-2.91	-10.38	1536.81	1529.08	-433.48	2028.21	343.65	1663.57
172	13	-3.05	-10.50	1521.57	1529.08	-433.48	2028.21	343.73	1668.24
172	14	-3.19	-10.61	1506.34	1529.08	-433.48	2028.21	344.18	1673.03
172	15	-3.33	-10.73	1491.10	1529.08	-433.48	2028.21	344.82	1677.95
172	16	-3.48	-10.82	1475.86	1529.08	-433.48	2028.21	346.85	1682.99
172	17	-3.63	-10.92	1460.62	1529.08	-433.48	2028.21	347.32	1688.17
172	18	-3.79	-11.03	1445.38	1529.08	-433.48	2028.21	347.56	1693.47
172	25	-5.06	-11.89	1338.71	1529.08	-433.48	2028.21	350.69	1733.99
172	32	-6.31	-13.20	1232.05	1529.08	-433.48	2028.21	362.73	1779.87
172	38	-7.32	-14.41	1140.62	1529.08	-433.48	2028.21	372.16	1823.17
172	46	-8.17	-15.30	1018.71	1529.08	-433.48	2028.21	388.13	1886.03
172	53	-8.92	-15.34	912.03	1529.08	-433.48	2028.21	404.11	1945.80
172	60	-9.59	-15.07	805.35	1529.08	-433.48	2028.21	424.54	2009.47

Appendix B – Travel Time Calculation Code

Appendix A includes the travel time calculation code, Westmansyn_4b.m, written for MATLAB. This code uses the Dijkstra Algorithm to calculate synthetic travel times within a given velocity model.

Westmansyn_4b

```
%prompt for file names and number of points to calculate at a time
velfile='velmod.txt';
srfile='UnalteredEventsStations.txt';
%points=input('How many points do you want to process at a time? ');
nxnod=input('Enter the number of nodes in the x direction: ');
nynod=input('Enter the number of nodes in the y direction: ');
nznod=input('Enter the number of nodes in the z direction: ');
TTfile=input('Enter the name of the output file: ','s');

%put data into matrix form
fid = fopen(velfile, 'r');
Velocity=fscanf(fid,'%f %f %f %f',[4 inf]);
array=Velocity';
fclose(fid);

fid = fopen(srfile, 'r');
srlocs=fscanf(fid,'%f %f %f %f %f %f',[6 inf]);
fclose(fid);
srlocs=srlocs';
srlocs(:,7)=0;

%Determine number of rays
rays=size(srlocs,1);

% establish velocity matrix

xmin=min(array(:,1));
xmax=max(array(:,1));
ymin=min(array(:,2));
ymax=max(array(:,2));
zmin=min(array(:,3));
zmax=max(array(:,3));

xgrid=xmin:((xmax-xmin)/(nxnod-1)):xmax;
ygrid=ymin:((ymax-ymin)/(nynod-1)):ymax;
zgrid=zmin:((zmax-zmin)/(nznod-1)):zmax;
[xi,yi,zi]=meshgrid(xgrid,ygrid,zgrid);
velmatrix = griddata3(array(:,1),array(:,2),array(:,3),array(:,4),xi,yi,zi);

% Nodes and initial velocity matrix
icounter = 1;
nodes=zeros(2*nxnod*nynod*nznod,5);
for l = 1:nxnod
    for m = 1:nynod
        for n = 1:nznod
            x=xmin+((xmax-xmin)*(l-1)/(nxnod-1));
            y=ymin+((ymax-ymin)*(m-1)/(nynod-1));
            z=zmin+((zmax-zmin)*(n-1)/(nznod-1));
            nodes(icounter, 1:4)=[icounter; x; y; z];
            icounter = icounter+1;
        end
    end
end

%Segments
segs=zeros(20*nxnod*nynod*nznod,3);
ic=1;
```

```
for i=1 : nxnod-1
    for j=1 : nynod-1
        for k=1:nznod-1
            nodenum=((i*nynod*nznod)+(j*nznod)+(k))-(nznod*nynod)-nznod;
            node1=nodes(nodenum,1);
            segs(ic,1:3)=[ic,node1,node1+1];    %a
            ic=ic+1;
            segs(ic,1:3)=[ic,node1,node1+nznod+1];    %b
            ic=ic+1;
            segs(ic,1:3)=[ic,node1,node1+nznod];    %c
            ic=ic+1;
            segs(ic,1:3)=[ic,node1,node1+(nynod*nznod)+nznod];    %d
            ic=ic+1;
            segs(ic,1:3)=[ic,node1,node1+(nynod*nznod)];    %e
            ic=ic+1;
            segs(ic,1:3)=[ic,node1,node1+(nynod*nznod)+1];    %f
            ic=ic+1;
            segs(ic,1:3)=[ic,node1,node1+(nynod*nznod)+nznod+1];    %g
            ic=ic+1;
            segs(ic,1:3)=[ic,node1+1,node1+nznod];    %h
            ic=ic+1;
            segs(ic,1:3)=[ic,node1+1,node1+(nynod*nznod)];    %i
            ic=ic+1;
            segs(ic,1:3)=[ic,node1+1,node1+(nynod*nznod)+nznod];    %j
            ic=ic+1;
            segs(ic,1:3)=[ic,node1+nznod+1,node1+(nynod*nznod)];    %k
            ic=ic+1;
            segs(ic,1:3)=[ic,node1+nznod,node1+(nynod*nznod)];    %l
            ic=ic+1;
            segs(ic,1:3)=[ic,node1+nznod,node1+(nynod*nznod)+1];    %m
            ic=ic+1;
        end
    end
end

for j=1:nynod-1
    for k=1:nznod-1
            nodenum=((nxnod*nynod*nznod)+(j*nznod)+(k))-(nznod*nynod)-nznod;
            node1=nodes(nodenum,1);
            segs(ic,1:3)=[ic,node1,node1+1];    %a
            ic=ic+1;
            segs(ic,1:3)=[ic,node1,node1+nznod+1];    %b
            ic=ic+1;
            segs(ic,1:3)=[ic,node1,node1+nznod];    %c
            ic=ic+1;
            segs(ic,1:3)=[ic,node1+1,node1+nznod];    %h
            ic=ic+1;
    end
end

for i=1:nxnod-1
    for k=1:nznod-1
            nodenum=((i*nynod*nznod)+(nynod*nznod)+(k))-(nznod*nynod)-nznod;
            node1=nodes(nodenum,1);
            segs(ic,1:3)=[ic,node1,node1+1];    %a
            ic=ic+1;
            segs(ic,1:3)=[ic,node1,node1+(nynod*nznod)];    %e
            ic=ic+1;
            segs(ic,1:3)=[ic,node1,node1+(nynod*nznod)+1];    %f
            ic=ic+1;
            segs(ic,1:3)=[ic,node1+1,node1+(nynod*nznod)];    %i
            ic=ic+1;
    end
end

for i=1:nxnod-1
    for j=1:nynod-1
            nodenum=((i*nynod*nznod)+(j*nznod)+(nznod))-(nznod*nynod)-nznod;
            node1=nodes(nodenum,1);
            segs(ic,1:3)=[ic,node1,node1+nznod];    %c
            ic=ic+1;
            segs(ic,1:3)=[ic,node1,node1+(nynod*nznod)+nznod];    %d
            ic=ic+1;
            segs(ic,1:3)=[ic,node1,node1+(nynod*nznod)];    %e
            ic=ic+1;
            segs(ic,1:3)=[ic,node1+nznod,node1+(nynod*nznod)];    %l
            ic=ic+1;
    end
end

for i=1:nxnod-1
```

```
            nodenum=((i*nynod*nznod)+(nynod*nznod)+(nznod))-(nznod*nynod)-nznod;
            node1=nodes(nodenum,1);
            segs(ic,1:3)=[ic,node1,node1+(nynod*nznod)];    %e
            ic=ic+1;
end

for j=1:nynod-1
            nodenum=((nxnod*nynod*nznod)+(j*nznod)+(nznod))-(nznod*nynod)-nznod;
            node1=nodes(nodenum,1);
            segs(ic,1:3)=[ic,node1,node1+nznod];    %c
            ic=ic+1;
end

for k=1:nznod-1
            nodenum=((nxnod*nynod*nznod)+(nynod*nznod)+(k))-(nznod*nynod)-nznod;
            node1=nodes(nodenum,1);
            segs(ic,1:3)=[ic,node1,node1+1];    %a
            ic=ic+1;
end

% add nodes at Sources and Receivers and add segments to nearest nodes
disp ('line 190')
temp=ic;

numnodes=icounter-1;
%numsegs=ic-1;

% Interpolate velocity to each node

for i=1:numnodes;
    x=nodes(i,2);
    y=nodes(i,3);
    z=nodes(i,4);
    nodes(i,5) = interp3(xi,yi,zi,velmatrix,x,y,z);
end

%_____________________________

disp ('nodes and segments done')

%---------------   end of nodes and segments    ---------------------


calctime=0;
allpaths=[];allcalctime=[];pathsize=[];pathlength=[];seglength=[];
pathnodes=[];

%Loop through Source/Receiver Array and find shortest time path for each
for mm = 1:rays
        % sources
    sx=srlocs(mm,1);
    sy=srlocs(mm,2);
    sz=srlocs(mm,3);
    nodes(icounter, 1:4)=[icounter; sx; sy; sz];
    nodes(icounter,5)=interp3(xi,yi,zi,velmatrix,sx,sy,sz);
    % find adjacent node toward minimun x,y,z then add segments to it
    % and other 7 adjacent nodes
    x=xmin+(floor((sx-xmin)/((xmax-xmin)/(nxnod-1)))*((xmax-xmin)/(nxnod-1)));
    y=ymin+(floor((sy-ymin)/((ymax-ymin)/(nynod-1)))*((ymax-ymin)/(nynod-1)));
    z=zmin+(floor((sz-zmin)/((zmax-zmin)/(nznod-1)))*((zmax-zmin)/(nznod-1)));
    j=find(floor(nodes(:,2))==floor(x));
    k=find(floor(nodes(:,3))==floor(y));
    l=find(floor(nodes(:,4))==floor(z));
    a=intersect(j,k);
    b=intersect(j,l);
    nodelist=intersect(a,b);
    node2=nodelist(1);
    segs(ic,1:3)=[ic,icounter,node2];
    ic=ic+1;
    segs(ic,1:3)=[ic,icounter,node2+nznod];   %c
    ic=ic+1;
    segs(ic,1:3)=[ic,icounter,node2+(nynod*nznod)+nznod];   %d
    ic=ic+1;
    segs(ic,1:3)=[ic,icounter,node2+(nynod*nznod)];   %e
    ic=ic+1;
    segs(ic,1:3)=[ic,icounter,node2+1];    %a
    ic=ic+1;
    segs(ic,1:3)=[ic,icounter,node2+nznod+1];   %b
    ic=ic+1;
    segs(ic,1:3)=[ic,icounter,node2+(nynod*nznod)+1];   %f
    ic=ic+1;
```

```
    segs(ic,1:3)=[ic,icounter,node2+(nynod*nznod)+nznod+1];   %g
    ic=ic+1;
    icounter = icounter+1;

    % receivers
    rx=srlocs(mm,4);
    ry=srlocs(mm,5);
    rz=srlocs(mm,6);
    nodes(icounter, 1:4)=[icounter; rx; ry; rz];
    nodes(icounter,5)=interp3(xi,yi,zi,velmatrix,rx,ry,rz);
    rnx=xmin+(floor((rx-xmin)/((xmax-xmin)/(nxnod-1)))*((xmax-xmin)/(nxnod-1)));
    rny=ymin+(floor((ry-ymin)/((ymax-ymin)/(nynod-1)))*((ymax-ymin)/(nynod-1)));
    rnz=zmin+(floor((rz-zmin)/((zmax-zmin)/(nznod-1)))*((zmax-zmin)/(nznod-1)));
    rj=find(floor(nodes(:,2))==floor(rnx));
    rk=find(floor(nodes(:,3))==floor(rny));
    rl=find(floor(nodes(:,4))==floor(rnz));
    ra=intersect(rj,rk);
    rb=intersect(rj,rl);
    nodelist=intersect(ra,rb);
    node2=nodelist(1);
    segs(ic,1:3)=[ic,icounter,node2];
    ic=ic+1;
    segs(ic,1:3)=[ic,icounter,node2+nznod];   %c
    ic=ic+1;
    segs(ic,1:3)=[ic,icounter,node2+(nynod*nznod)+nznod];   %d
    ic=ic+1;
    segs(ic,1:3)=[ic,icounter,node2+(nynod*nznod)];   %e
    ic=ic+1;
    segs(ic,1:3)=[ic,icounter,node2+1];    %a
    ic=ic+1;
    segs(ic,1:3)=[ic,icounter,node2+nznod+1];   %b
    ic=ic+1;
    segs(ic,1:3)=[ic,icounter,node2+(nynod*nznod)+1];   %f
    ic=ic+1;
    segs(ic,1:3)=[ic,icounter,node2+(nynod*nznod)+nznod+1];   %g
    icounter = icounter-1;
    ic=temp;
    % find source node #
    sourcenode=find((nodes(:,2)==srlocs(mm,1))&...
        (nodes(:,3)==srlocs(mm,2))&(nodes(:,4)==srlocs(mm,3)),1);
    % find receiver node #
    recnode=find((nodes(:,2)==srlocs(mm,4))&...
        (nodes(:,3)==srlocs(mm,5))&(nodes(:,4)==srlocs(mm,6)),1);

    %use Dijkstra's method for shortest time
    node_ids=nodes(:,1);
    [num_map_pts,cols]=size(nodes);
    table=sparse(num_map_pts,2);
    shortest_time=Inf(num_map_pts,1);
    settled=zeros(num_map_pts,1);
    path=num2cell(NaN(num_map_pts,1));
    pidx=find(sourcenode==node_ids);
    shortest_time(pidx)=0;
    table(pidx,2)=0;
    settled(pidx)=1;
    path(pidx)={sourcenode};

    while_cmd='settled(zz)==0';
    zz=find(recnode==node_ids);

    while eval(while_cmd)
        % update the table
        table(:,1)=table(:,2);
        table(pidx,2)=0;
        % find neighboring nodes in the segments list
        jj=find(node_ids(pidx)==segs(:,2));
        kk=find(node_ids(pidx)==segs(:,3));
        neighbor_ids=[segs(jj,3); segs(kk,2)];
        % calculate the times to the neighboring nodes (by dividing distance by velocity) and keep track of the
paths
        for k=1:length(neighbor_ids)
            cidx=find(neighbor_ids(k)==node_ids);
            if ~settled(cidx)
                calctime=(sqrt(sum((nodes(pidx,2:4)-nodes(cidx,2:4)).^2)))/((nodes(pidx,5)+nodes(cidx,5))*0.5);
%%% changed from
                if (table(cidx,1)==0) || (table(cidx,1)>(table(pidx,1)+calctime))
                    table(cidx,2)=table(pidx,1)+calctime;
                    tmp_path=path(pidx);
                    path(cidx)={[tmp_path{1} neighbor_ids(k)]};
                else
                    table(cidx,2)=table(cidx,1);
```

```
                end
            end
        end
        % find the minimum non-zero value in the table and save it
        nidx=find(table(:,2)>0);
        ndx=find(table(nidx,2)==min(table(nidx,2)));
        if isempty(ndx)
            break
        else
            pidx=nidx(ndx(1));
            shortest_time(pidx)=table(pidx,2);
            settled(pidx)=1;
        end
    end

    srlocs(mm,7)=shortest_time(zz);

disp ('percent of rays complete')
disp (100*mm/rays)

%Write each iteration to end of output file
dlmwrite(TTfile,srlocs(mm,1:7),'-append');

end
```

Appendix C – Supplemental Tomograms

Tomograms of Time 1, Time 2, Time 3, and Time 4 are provided for northing values not reported in text. Tomograms showing northings of -100 meters and -500 meters are reported for the 1,790 layer and the 1,400 layer. Differences between Time 2 and Time 1, Time 3 and Time 1, and Time 4 and Time 1 are also reported at -100 meters northing.

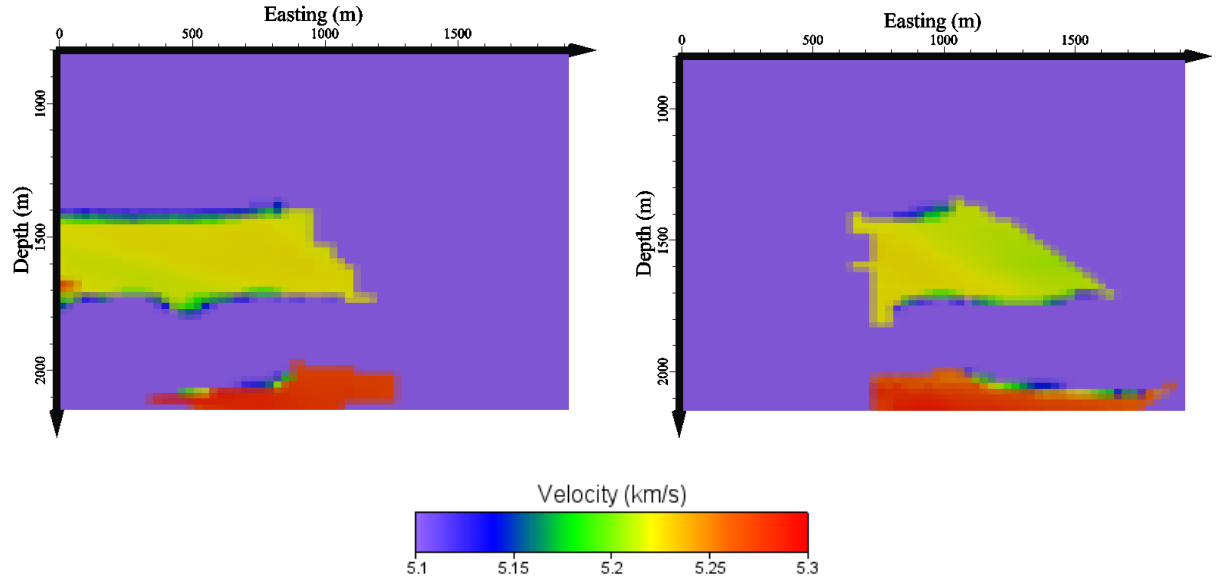

Figure C.1: 1,400 layer tomograms for Time 1 at -100 meters northing (left) and -500 meters northing (right)

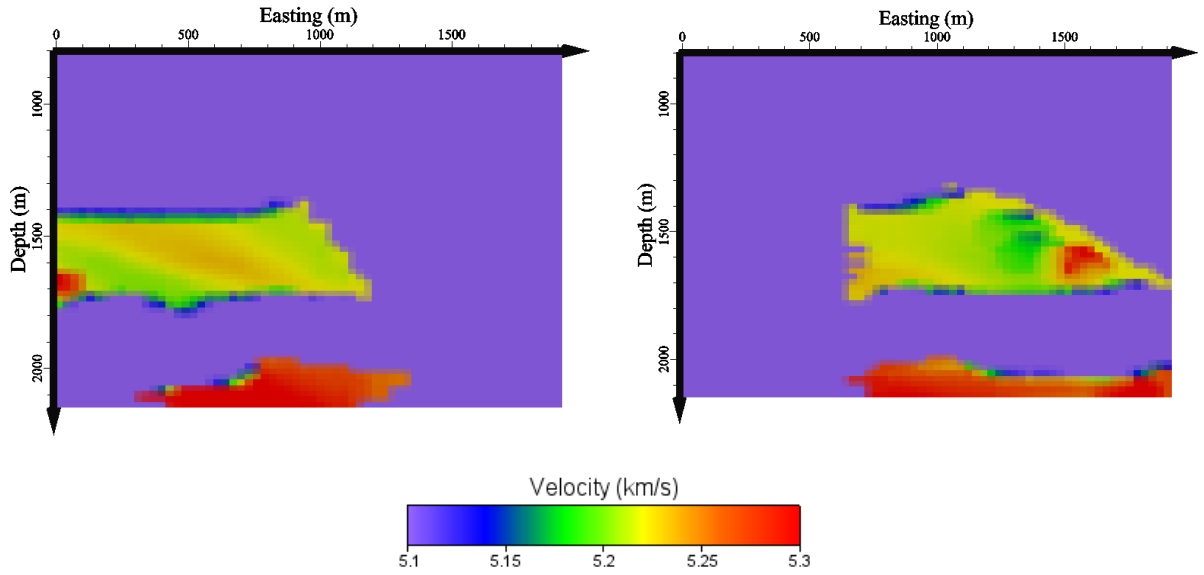

Figure C.2: 1,400 layer tomograms for Time 2 at -100 meters northing (left) and -500 meters northing (right)

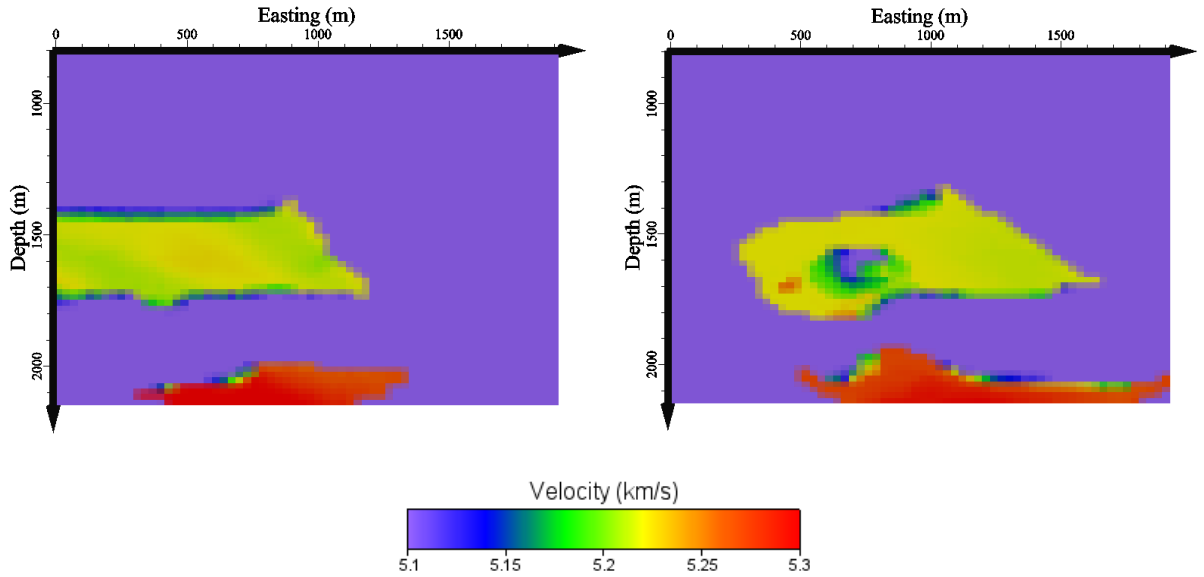

Figure C.3: 1,400 layer tomograms for Time 3 at -100 meters northing (left) and -500 meters northing (right)

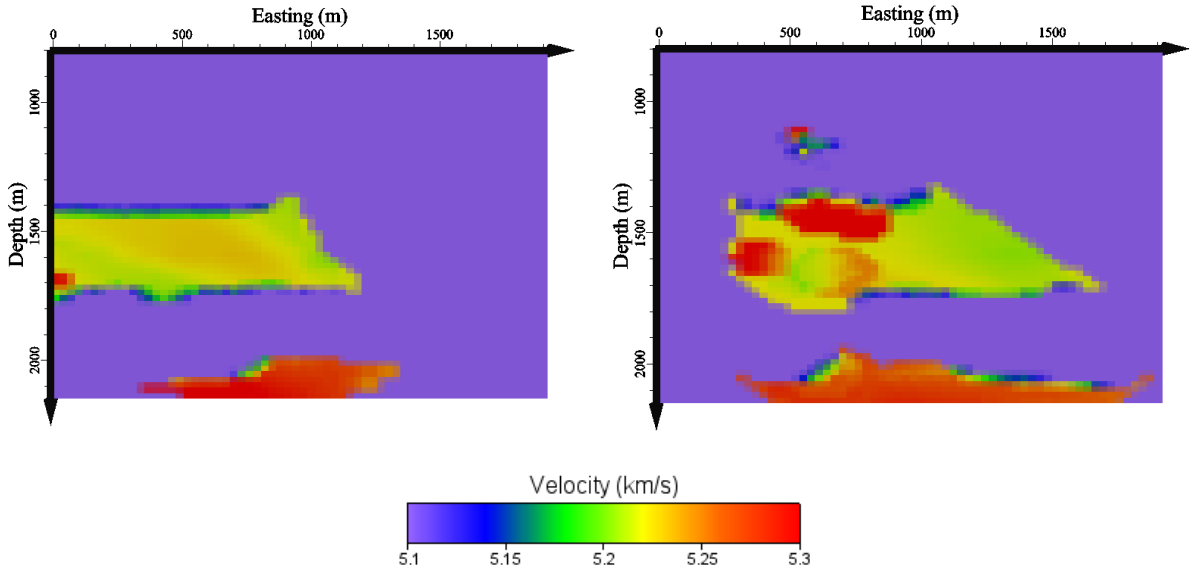

Figure C.4: 1,400 layer tomograms for Time 4 at -100 meters northing (left) and -500 meters northing (right)

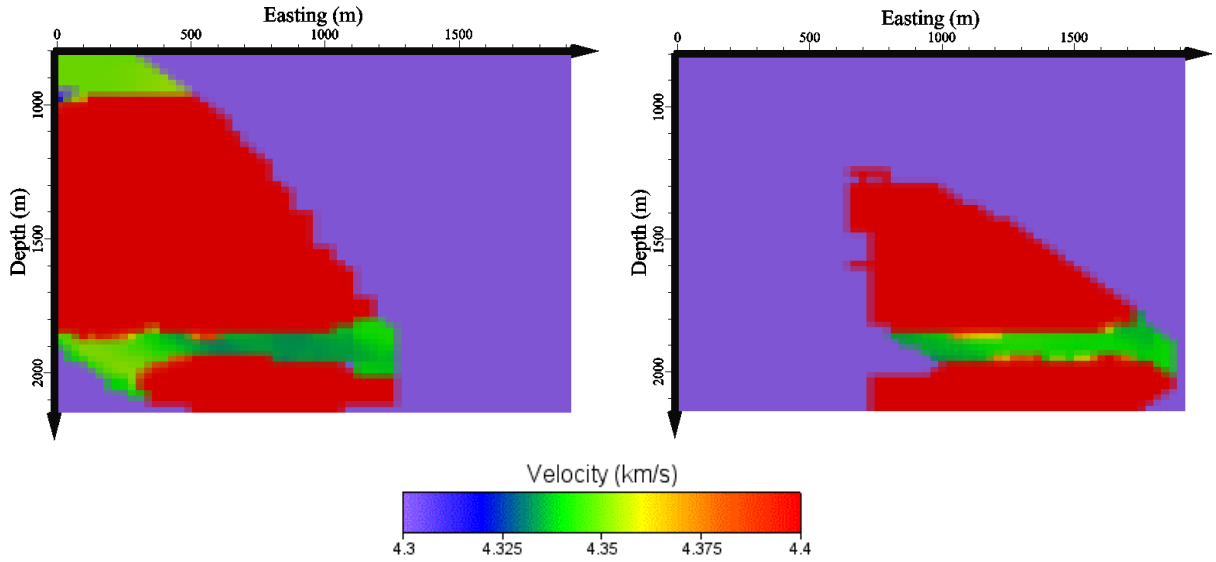

Figure C.5: 1,790 layer tomograms for Time 1 at -100 meters northing (left) and -500 meters northing (right)

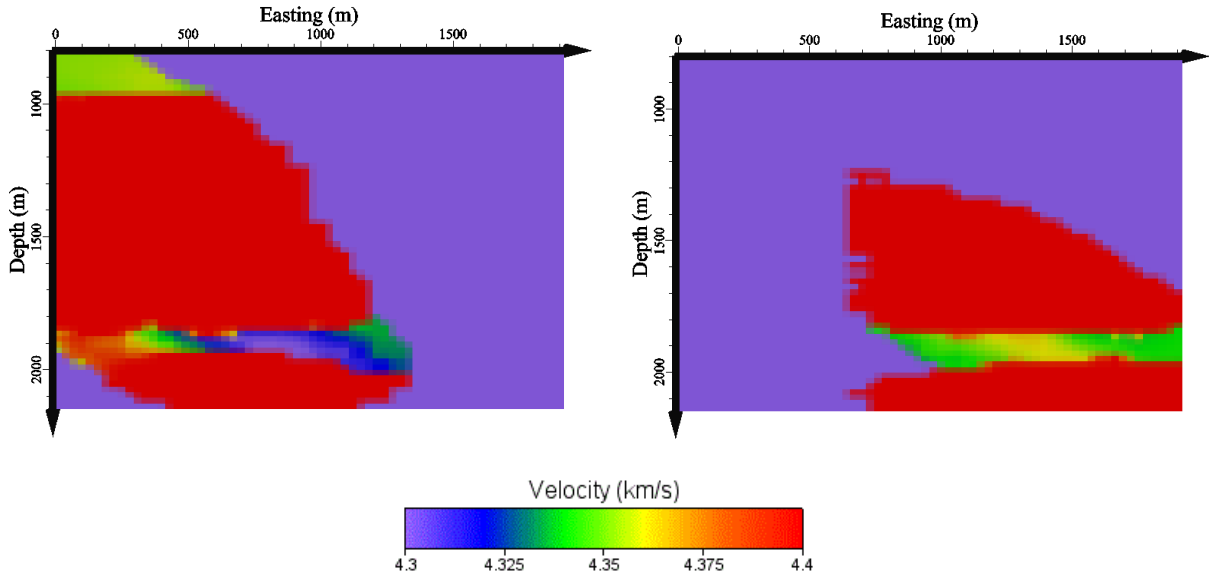

Figure C.6: 1,790 layer tomograms for Time 2 at -100 meters northing (left) and -500 meters northing (right)

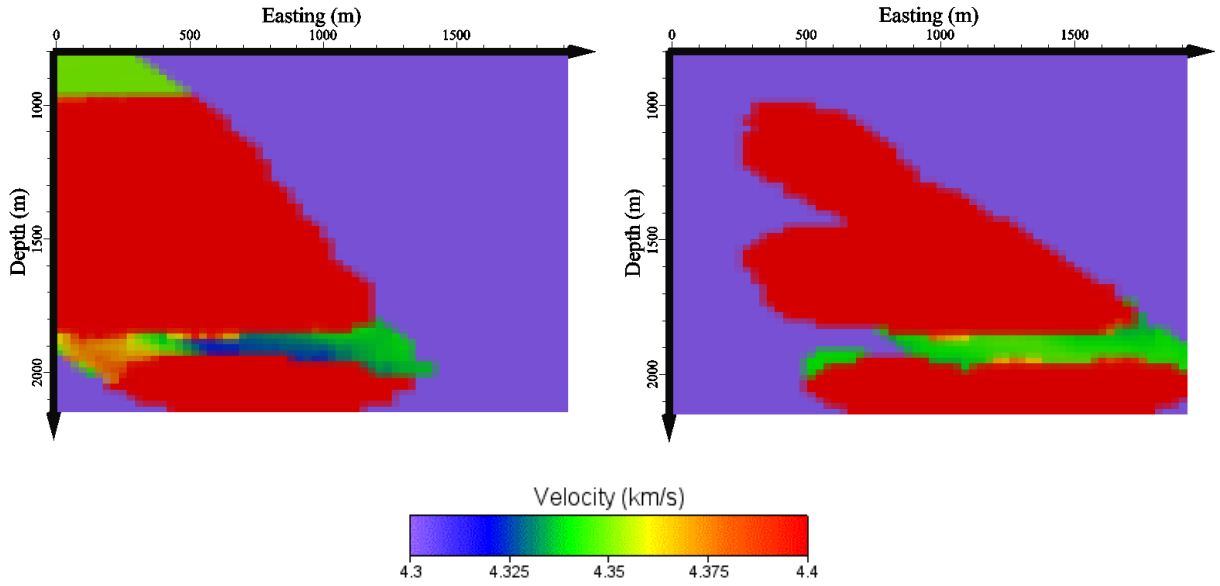

Figure C.7: 1,790 layer tomograms for Time 3 at -100 meters northing (left) and -500 meters northing (right)

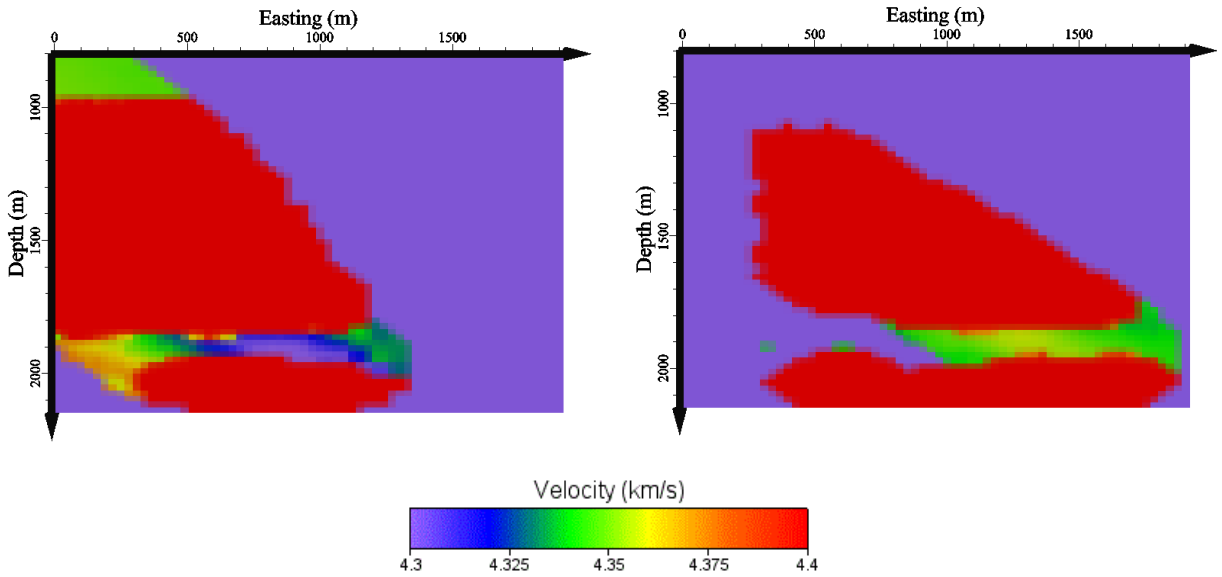

Figure C.8: 1,790 layer tomograms for Time 4 at -100 meters northing (left) and -500 meters northing (right)

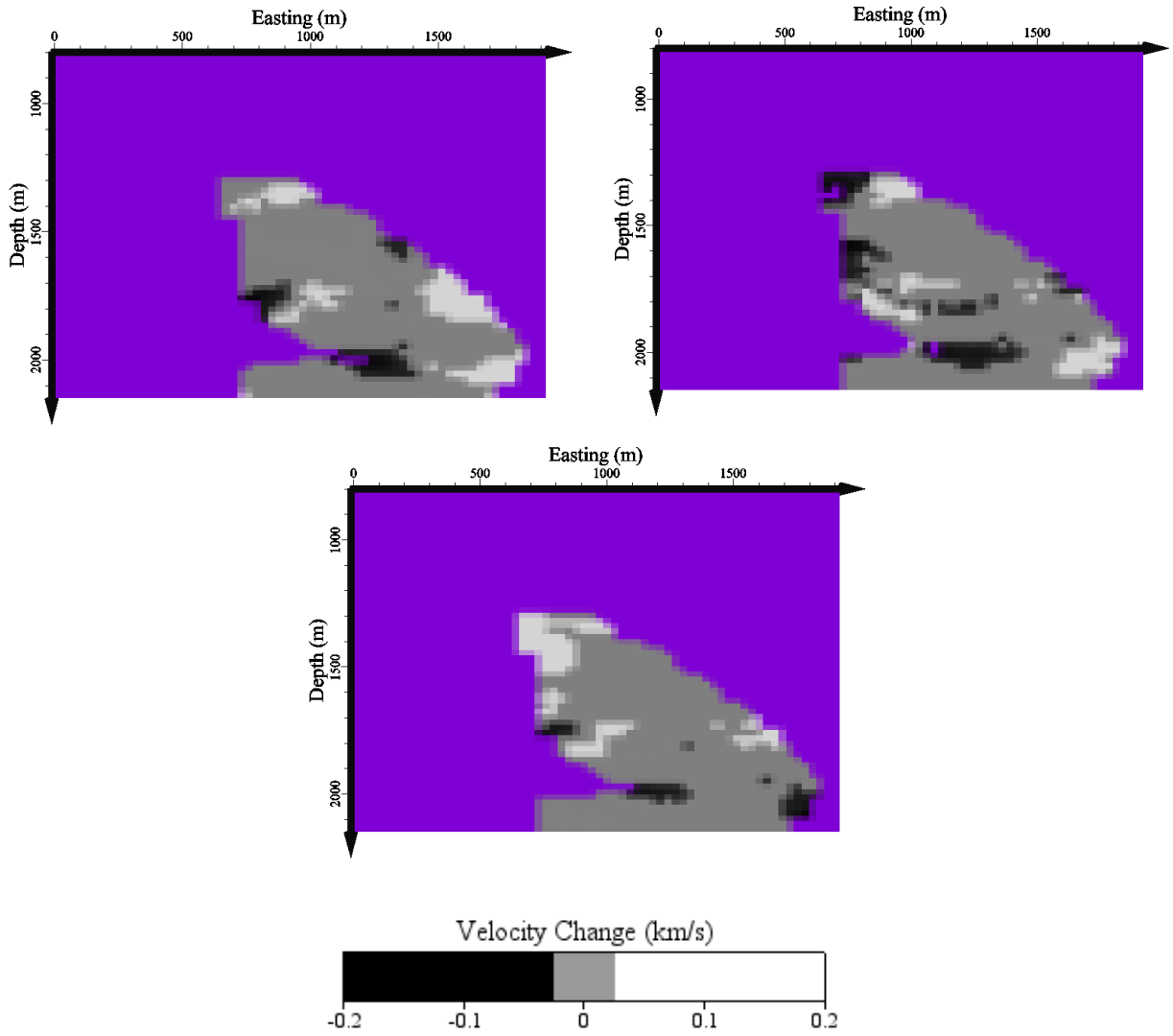

Figure C.9: Difference between Time 2 and Time 1 (top left) Time 3 and Time 1 (top right) Time 4 and Time 1 (bottom) at -100 meters northing